Title

Investigating the variability of subtropical marine boundary layer clouds in observations and climate models

Author

Myers, Timothy Albert

Publication Date

2015

UNIVERSITY OF CALIFORNIA, SAN DIEGO

Investigating the variability of subtropical marine boundary layer clouds in observations and climate models

A dissertation submitted in partial satisfaction of the
requirements for the degree
Doctor of Philosophy

in

Earth Sciences

by

Timothy Albert Myers

Committee in charge:

Professor Joel Norris, Chair
Professor Ian Eisenman
Professor Myrl Hendershott
Professor Jan Kleissl
Professor Shang-Ping Xie

2015

The dissertation of Timothy Albert Myers is approved, and it is acceptable in quality and form for publication on microfilm and electronically:

Chair

University of California, San Diego

2015

TABLE OF CONTENTS

LIST OF FIGURES

LIST OF TABLES

ACKNOWLEDGEMENTS

Without the support of my family and especially my parents, I would not have been able to complete this thesis. I learned from them not only how to think critically and to work diligently but also to appreciate the simple pleasures of life such as enjoying a walk in nature or having a home-cooked meal with loved ones. The outstanding academic achievements of my brother Roberto, grandfather Vernon, and grandmother Betty motivated me to seek my own – among them the completion of this dissertation.

Thank you to my advisor Joel Norris for helping me to become a thoughtful, curious, and meticulous scientist. I learned more about science from our spontaneous discussions than in any course – most importantly how to ask the right questions.

Lastly I thank the friends, colleagues, and surfers I met at Scripps who made graduate school so enjoyable.

Chapters 2 and 3, respectively, are published in their entirety in:

- Myers, T.A., and Norris, J.R., "Observational evidence that enhanced subsidence reduces subtropical marine boundary layer cloudiness", *J. Climate*, 26(19), 2013.
- Myers, T.A., and Norris, J.R., "On the relationships between subtropical clouds and meteorology in observations and CMIP3 and CMIP5 models", *J. Climate*, 28(8), 2015.

Material from Chapter 4 is currently being prepared for submission for publication as

- Myers, T.A., and Norris, J.R., "Observational and model estimates of subtropical marine boundary layer cloud feedbacks", in prep.

The dissertation author was the preliminary investigator and author of these three papers.

VITA

2009	B.S. in Atmospheric Science, Cornell University
2011	M.S. in Oceanography, University of California, San Diego
2015	Ph.D. in Earth Sciences, University of California, San Diego

PUBLICATIONS

Seethala, C., Norris, J.R., and Myers, T.A., “How has subtropical stratocumulus and associated meteorology changed since the 1980s?”, *J. Climate*, in revision.

Myers, T.A., and Norris, J.R., “On the relationships between subtropical clouds and meteorology in observations and CMIP3 and CMIP5 models”, *J. Climate*, 28(8), 2015.

Myers, T.A., and Norris, J.R., “Observational evidence that enhanced subsidence reduces subtropical marine boundary layer cloudiness”, *J. Climate*, 26(19), 2013.

ABSTRACT OF THE DISSERTATION

Investigating the variability of subtropical marine boundary layer clouds in observations and climate models

by

Timothy Albert Myers

Doctor of Philosophy in Earth Sciences

University of California, San Diego, 2015

Professor Joel Norris, Chair

Low-level clouds found over the eastern subtropical oceans have a substantial cooling effect on Earth's climate since they strongly reflect solar radiation back to space, and their simulation in climate models contributes to large uncertainty in global warming projections. This thesis aims to increase understanding of these marine boundary layer clouds through observational analysis, theoretical considerations, and an evaluation of their simulation in climate models. Examination of statistical relationships between cloud properties and large-scale meteorological variables is a key method employed throughout the thesis. The meteorological environment of marine boundary layer clouds shapes their properties by affecting the boundary layer's depth and structure.

It is found that enhanced subsidence, typically thought to promote boundary layer cloudiness, actually reduces cloudiness when the confounding effect of the strength of the temperature inversion capping the boundary layer is taken into account. A conceptual model is able to explain this result. Next, fundamental deficiencies in the simulation of subtropical clouds in two generations of climate models are identified. Remarkably, the newer generation of climate models is in some ways inferior to the older generation in terms of capturing key low-level cloud processes. Subtropical mid- and high-level clouds are also found to contribute more to variability in the radiation budget at the top of the atmosphere than previously thought. In the last portion of the thesis, large inter-model spread in subtropical cloud feedbacks is shown to arise primarily from differences in the simulation of the interannual relationship between shortwave cloud radiative effect and sea surface temperature. An observational constraint on this feedback suggests that subtropical marine boundary layer clouds will act as a positive feedback to global warming.

Chapter 1

Introduction

Clouds are a key aspect of climate through their role in the Earth's energy budget. Owing to their high brightness relative to most land and ocean surfaces, clouds have a cooling effect on the climate by reflecting more shortwave radiation to space than would be the case for an atmosphere free of clouds. This cooling effect is estimated to be ∼50 W m^{-2} (*Dolinar et al.*, 2014) on a global annual mean basis. In addition, owing to their low temperature relative to most underlying surfaces, clouds have a warming effect on the climate by emitting less longwave radiation to space than would be the case for an atmosphere free of clouds. This warming effect is estimated to be ∼28 W m^{-2} (*Dolinar et al.*, 2014). Thus, clouds on average cool the climate system by ∼22 W m^{-2}. This is greater than five times the radiative forcing expected to occur due to a doubling of the atmospheric concentration of CO_2 (*Hartmann*, 1994). Assuming a climate feedback parameter of 0.5 K / W m^{-2} (*Hartmann*, 1994), the effect of clouds on the energy balance of the climate system in steady state translates to a cooling of 11 K!

Clearly, even small changes in global cloudiness can have a large effect on climate, a notion first formally recognized by *Charney et al.* (1979). In that study, the equilibrium global mean surface temperature response due to a doubling of CO_2 was estimated using the first global climate models. Unknown changes in cloud properties under this scenario were inferred through loose theoretical reasoning to yield an uncertainty of future temperature change of 1.5 K. Combining this with additional inter-model uncertainty, *Charney et al.* (1979) concluded that a doubling of CO_2 would result in a global surface warming between 1.5 K and 4.5 K. Even though climate models since the Charney Report have become much more complex and realistic, this estimated range of climate sensitivity has remained virtually unchanged (*Randall et al.*, 2007; *Stocker et al.*, 2014).

Why is this so? The main contributor for this large range of climate sensitivity has been identified as uncertainty of projections of reflected shortwave radiation by clouds (*Webb et al.*, 2006; *Andrews et al.*, 2012b; *Vial et al.*, 2013). Models that project less reflection by clouds in the future climate tend to simulate more global warming compared to models that project more reflection by clouds. Several studies have suggested that subtropical marine boundary layer (MBL) cloud feedbacks are at the core of these divergent model projections (*Bony and Dufresne*, 2005; *Soden and Vecchi*, 2011; *Vial et al.*, 2013). It follows that to reduce the uncertainty of climate sensitivity estimates, a more complete understanding of MBL clouds is needed. This thesis aims to further our knowledge of subtropical clouds through observational analysis of, theoretical considerations, and evaluation of their simulation in climate models.

Subtropical MBL clouds include sheet-like stratus, convective yet horizontally homogenous stratocumulus, and convective scattered shallow cumulus. By definition, these clouds occur within the marine boundary layer – the first few hundred to several thousand meters of the atmosphere where turbulent fluxes of heat and moisture shape its thermodynamic profile. The MBL extends to a statically stable layer where temperature sharply increases with height. This temperature inversion acts as a lid by preventing free-tropospheric air from mixing with the moister air of the boundary layer. Climatologically, stratus and stratocumulus clouds are prevalent along the western coasts of the continents over the subtropical oceans, while shallow cumulus clouds are prevalent in similar latitudes but farther west. Distinguishing these regimes are particular large-scale meteorological characteristics that help to shape the MBL structure and in turn different cloud types and properties.

The inter-connectedness between subtropical MBL clouds and the properties of the meteorological environment in which they occur is a main focus of this thesis. Relationships between subtropical clouds and large-scale meteorological factors such as the temperature inversion strength can elucidate understanding of the cloud dynamics, help establish statistical models for predicting changes in cloud properties, and serve as performance metrics for the simulation of subtropical cloud processes in climate models. Numerous studies have investigated these relationships (e.g. *Klein and Hartmann*, 1993; *Norris and Leovy*, 1994; *Klein et al.*, 1995; *Bony and Dufresne*, 2005; *Clement et al.*, 2009). What distinguishes this thesis from previous studies is: 1) the identification of a physical mechanism affecting subtropical MBL cloudiness in observations using novel statistical methods; 2) the discovery of a heretofore unrecognized deficiency in climate model simulation of subtropical clouds; 3) the finding that variability of mid- and high-level clouds in regions of climatological subsidence can have a larger effect on the top-of-atmosphere radiation budget than previously thought; 4) the discovery of the key mechanisms driving subtropical cloud feedbacks in climate models.

To understand how large-scale meteorological conditions can help shape cloud properties, it is useful to consider one of the simplest theoretical models of the cloudy MBL, first formulated by *Lilly* (1968) and briefly discussed here. This model assumes that the MBL is well mixed with respect to heat and moisture. In such a framework, the governing equations describe the conservation of mass, equivalent potential temperature θ, and total water mixing ratio q within the boundary layer. These equations are written as

$$\frac{dz_i}{dt} = w_{\mathrm{ent}} - w_{\mathrm{sub}} \tag{1.1}$$

$$\frac{d\theta}{dt} = (V\Delta\theta_0 + w_e\Delta\theta_+ - \Delta F)/z_i \tag{1.2}$$

$$\frac{dq}{dt} = (V\Delta q_0 + w_{\mathrm{ent}}\Delta q_+)/zi. \tag{1.3}$$

Here, z_i is the depth of the boundary layer or, equivalently, cloud-top height; w_{ent} is the rate of entrainment of tropospheric air into the boundary layer; w_{sub} is the cloud-top subsidence rate; V is the surface horizontal windspeed multiplied by a non-dimensional transfer coefficient; ΔF is the radiative flux difference between the surface and cloud top; and $\Delta\theta_0 = \theta_0 - \theta$, $\Delta\theta_+ = \theta_+ - \theta$, where θ_0 and θ_+ are the potential temperatures at the sea surface and just above cloud top, respectively. Identical notation is used for Δq_0 and Δq_+.

In these equations, V, w_{sub}, θ_0, q_0, θ_+, q_+, and ΔF are all specified. If steady state is assumed, there are then three equations and four unknowns z_i, w_{ent}, θ, and q. For closure, w_{ent} must be parameterized in some way. One simple and physically intuitive formulation is to assume that $w_{\text{ent}} = \alpha \Delta F / \Delta \theta_+$, where α is a non-dimensional constant representing the entrainment efficiency (*Stevens*, 2006). Strong radiative cooling ΔF at cloud top induces negative buoyancy of air parcels, increasing the entrainment rate, and vice versa. Strong static stability $\Delta\theta_+$ inhibits the mixing of air between the MBL and the free troposphere, reducing the entrainment rate, and vice versa. Of course, the value of α must be determined in some way (empirically or through physical arguments). The formulation of w_{ent} is thus a challenging problem, and given the solutions' to Eqs. 1.1–1.3 dependence on w_{ent}, so is the modeling of the cloudy MBL even in this simplified framework (*Stevens*, 2006). Climate models cannot explicitly resolve entrainment, suggesting why they struggle so much to simulate MBL clouds (*Wood*, 2012).

In steady state, cloud top height is located where the rate of entrainment w_{ent} of free-tropospheric air into the boundary layer is balanced by the subsidence rate w_{sub} at cloud top. Surface heating $V\Delta\theta_0$ and entrainment warming $w_{\text{ent}}\Delta\theta_+$ are balanced by cloud-top radiative cooling ΔF. Surface moisture flux $V\Delta q_0$ is balanced by the flux of dry air from the free troposphere $w_{\text{ent}}\Delta q_+$. It is clear that large-scale environmental conditions affect the depth of the boundary layer and its moisture and heat content. These properties of the MBL in turn determine cloud thickness, water content, horizontal coverage, and albedo.

A palpable way in which theory of a cloudy MBL can be used to increase understanding and indeed explain observed relationships among subsidence, inversion strength, and subtropical MBL cloudiness is presented in the subsequent chapter. In Chapter 3, we evaluate the performance of a suite of coupled climate models in simulating relationships between meteorological variables and subtropical cloud radiative effect. Finally, in Chapter 4, we use a diagnostic technique employing these relationships to explain the subtropical cloud feedbacks produced in global warming simulations in an ensemble of climate models and exploit observations to suggest how subtropical cloud radiative effect will change in a warming climate.

The reader should note that, while there is an underlying theme of this thesis, each chapter is written as a stand-alone study with key results that do not depend critically on the results of other chapters.

Chapter 2

Observational Evidence That Enhanced Subsidence Reduces Subtropical Marine Boundary Layer Cloudiness

Low-level clouds have the largest net cloud radiative effect of all cloud types, acting to cool the planet via high albedo and a weak greenhouse effect (*Hartmann et al.*, 1992). The large and persistent decks of stratus and stratocumulus over eastern subtropical oceans are the primary contributors to this cooling effect. These clouds occur predominantly within a shallow, well-mixed marine boundary layer (MBL) over cool sea surface temperatures (SSTs) and under a strong temperature inversion associated with the descending branches of the Hadley circulation (*Albrecht et al.*, 1995; *Norris*, 1998a; *Wood and Hartmann*, 2006). Both inversion strength and subsidence weaken farther west in the downstream region of the trade winds, and the stratus and stratocumulus eventually transition to scattered trade cumulus, which have a more minor cooling effect. These trade cumulus often occur within a deep, decoupled MBL (*Albrecht et al.*, 1995; *Norris*, 1998a; *Wood and Hartmann*, 2006).

Both stratus and stratocumulus and trade cumulus are intimately connected to the properties of the MBL in which they exist. In a well-mixed MBL, cloud-top radiative cooling induces negative buoyancy and thereby drives the turbulence that mixes heat and moisture within the MBL (*Lilly*, 1968). Cloud base resides at the lifting condensation level, and cloud top coincides with the MBL topat the base of a temperature inversion and sharp decrease in moisture. For a well-mxed MBL in steady state, radiative cooling at cloud top is largely balanced by entrainment heating, which equals the rate of cloud-top subsidence warming. Cloud-top subsidence and entrainment are thus crucial components of any realistic physical model of a cloudy MBL. When the MBL is decoupled, well-mixed subcloud and cloud layers are separated by a stable transition layer in which potential temperature increases with height. This inhibits the mixing of heat and moisture between the two layers, and transport of moisture from the subcloud layer to the cloud layer intermittently occurs in rising cumulus plumes.

Wood and Bretherton (2004) found that shallow, cloudy MBLs tend to be well mixed, whereas deep MBLs tend to be decoupled. Several physical mechanisms are thought to cause variations in MBL depth and the extent of decoupling (and thereby variations in MBL cloudiness). A strong inversion is thought to promote a shallow, well-mixed MBL containing stratus and stratocumulus (relatively large cloud fraction) by inhibiting entrainment, while a weak inversion is thought to promote a deep, decoupled MBL containing scattered trade cumulus (relatively small cloud fraction) by promoting entrainment (*Bretherton and Wyant*, 1997). Enhanced subsidence and the associated surface divergence are thought to promote a shallow MBL. This may lead to a more well-mixed MBL as well as reduced cloud thickness (*Deardorff*, 1976; *Schubert et al.*, 1979).

Several observational studies have investigated the relationship between low-level cloud amount and inversion strength and subsidence over various time scales that confirm the results from theoretical models. Over the seasonal cycle, lower tropospheric stability (LTS) and estimated inversion strength are in phase with and positively correlated to low-level cloud fraction and explain most of its seasonal variability (*Klein and Hartmann*, 1993; *Wood and Bretherton*, 2006; *Sun et al.*, 2011). *Clement et al.* (2009) found strong positive correlations between low-level cloud fraction and LTS and pressure vertical velocity at 500hPa over interannual and decadal time scales over the northeast Pacific. *Muñoz et al.* (2011) investigated the climatology of the MBL over a coastal site in northern Chile. They found that cloudy nights tend to be characterized by stronger inversions, enhanced subsidence, and a shallower MBL than clear nights.

Although providing strong observational evidence for some of the main physical mechanisms controlling MBL cloudiness, previous studies have not systematically taken into account the relationship between subsidence and inversion strength. Climatologically, strong inversions tend to occur where and when subsidence is enhanced. There are two reasons for this. If the free troposphere is statically stable, enhanced subsidence will act to locally warm air above the MBL. This will obviously act to increase the strength of the inversion. Furthermore, subsidence over eastern subtropical oceans is climatologically associated with equatorward winds and meridional cold air advection, which generally decreases with height. More cooling within the MBL than above it due to the vertical profile of advection also acts to increase the strength of the inversion. Considering the correlation between subsidence and inversion strength, one might wonder whether enhanced subsidence typically coincides with greater MBL cloudiness only because enhanced subsidence is associated with strong inversions.

Some recent studies have suggested that enhanced subsidence, when operating independently from inversion strength, actually reduces MBL cloudiness. Using a mixed-layer model forced by large-scale conditions, *Zhang et al.* (2009) showed that the probability of a cloud-free equilibrium solution increases as surface divergence ($\sim$subsidence) increases, although cloud fraction was found to be larger overall under subsidence than under ascent. *Sandu and Stevens* (2011) used a large-eddy simulation to explore the stratocumulus-to-cumulus (Sc-to-Cu) transition. Although the SST gradient and initial inversion strength were the dominant factors controlling the transition, reducing subsidence to zero enabled a thicker and less broken residual stratocumulus layer to persist to the end of the trajectory. *Mauger and Norris* (2010) used Lagrangian trajectories to assess the impact of reanalysis meteorological history on satellite-observed low-level cloud fraction over the northeast Atlantic. They found that enhanced subsidence and surface divergence are associated with reduced low-level cloud fraction 0–12 h later, whereas increased LTS is associated with increased low-level cloud fraction 24–48 h later. *Kubar et al.* (2012) examined correlations between reanalysis pressure vertical velocity at 500hPa and satellite low-level cloud fraction using daily through 90-day-mean values. They found that over the eastern subtropical oceans, enhanced subsidence is associated with a near-zero or negative change in cloud fraction.

What is needed is a globally based observational study that systematically investigates the independent effects of inversion strength and subsidence on MBL cloudiness. In the present work, we use compositing techniques to examine how low-level cloud fraction, liquid water path (LWP), estimated cloud-top height, and morphological cloud type vary with vertical velocity at 700 hPa and estimated inversion strength when either is held constant. The spatial domain comprises subsidence regions over tropical (30°S−30°N) oceans, and we analyze geographical, seasonal, and interannual relationships. By focusing only on areas experiencing subsidence rather than some arbitrarily defined geographic domain, we avoid the confounding effects of ascent – which has a fundamentally different relationship to MBL cloudiness than does subsidence – in our interpretation of the results. These results will increase our understanding of the dynamical and thermodynamical conditions controlling subtropical MBL cloudiness and may have relevance to the cloud response to climate change.

2.1 Data

Table 2.1 summarizes the data sources used. Satellite cloud records include monthly mean low+midlevel cloud fraction and cloud-top temperature from the International Satellite Cloud Climatology Project (ISCCP) (*Rossow and Schiffer*, 1999), low+midlevel cloud fraction from the Advanced Very High Resolution Radiometer (AVHRR) Pathfinder Atmospheres - Extended dataset (PATMOS-x) (*Heidinger et al.*, 2012), total liquid water path from microwave retrievals produced by the University of Wisconsin team (UWISC) (*O'Dell et al.*, 2008), and total cloud fraction and cloud-top height from the Moderate Resolution Imaging Spectroradiometer (MODIS) (*Minnis et al.*, 2011b,a). The ISCCP and PATMOS-x data were corrected for artifacts in a manner similar to that described in *Clement et al.* (2009), but use of uncorrected data has minimal impact on our results. Despite our focus on MBL clouds, we use combined low- and midlevel cloudiness because ISCCP and PATMOS-x tend to misplace some inversion-capped true low-level clouds in the midlevel category (*Mace et al.*, 2006). Since there are rarely true midlevel clouds in tropical ocean subsidence regions, combining retrieved low- and midlevel cloud fraction (CF) yields a more accurate estimate of true MBL cloudiness (*Minnis et al.*, 1992). Because ISCCP and PATMOS-x report only low- and midlevel CF unobstructed by higher clouds, we follow the method of *Rozendaal et al.* (1995) to estimate the true MBL cloud fraction L as

$$L = L' + M'/(1 - H'), \tag{2.1}$$

where L', M', and H' are the given low-, mid-, and high-level retrievals respectively. This assumes that the actual clouds are randomly overlapped.

Changes in cloud structure occurring in the Sc-to-Cu transition are not readily perceived by the passive remote sensing of ISCCP, PATMOS-x, and MODIS. As a complement to the satellite datasets, we examine variability in the frequency of occurrence of low cloud type reported by observers on ships. Previous research has demonstrated that visually identified ordinary stratocumulus, cumulus-under-stratocumulus, and large cumulus are associated with different average values of MBL depth and decoupling (*Norris*, 1998a). We obtained visual cloud type reports from the Extended Edited Cloud Report Archive (EECRA) (*Hahn and Warren*, 1999). We averaged individual cloud reports within $2.5° \times 2.5°$ grid boxes to monthly mean values of the frequency of occurrence of each low cloud type. Only daytime reports were used because observers have difficulty correctly identifying cloud type under conditions of poor illumination (*Norris*, 1998a).

The Climate Forecast System Reanalysis (CFSR) provided monthly mean atmospheric data for our analysis (*Saha et al.*, 2010). We supplemented this with the European Centre for Medium-Range Weather Forecasts (ECMWF) Interim ReAnalysis (ERA-Interim) (*Dee et al.*, 2011), the Japanese 25-year Reanalysis

Project (JRA-25) (*Onogi et al.*, 2007), and the Modern-Era Retrospective Analysis for Research and Applications (MERRA) (*Rienecker et al.*, 2011). For a measure of subsidence, we chose pressure vertical velocity at 700 hPa ω_{700} rather than at the more traditional level of 500hPa because the former is closer to the top of the MBL. Moreover, ω_{700} is more directly connected to estimated inversion strength through vertical temperature advection. For estimated inversion strength (EIS), we use the formula derived by *Wood and Bretherton* (2006); that is,

$$\mathrm{EIS} = \mathrm{LTS} - \Gamma_m^{850}(z_{700} - \mathrm{LCL}), \tag{2.2}$$

where lower tropospheric stability (LTS) is the difference in potential temperature between the 700-hPa level and the surface, Γ_m^{850} is the moist adiabatic lapse rate at 850hPa, z_{700} is the height of the 700-hPa level relative to the surface, and LCL is the height of the lifting condensation level relative to the surface. The calculation of EIS requires SST, temperature at 700 hPa T_{700}, surface relative humidity, sea level pressure (SLP), and z_{700}. As in *Wood and Bretherton* (2006), we assume a fixed relative humidity of 80%, which simplifies the calculation while introducing little error. To calculate the LCL, we use the method of *Georgakakos and Bras* (1984).

The ISCCP, PATMOS-x, and EECRA cloud data are available on an equal-angle grid with latitude-longitude spacing of $2.5^\circ \times 2.5^\circ$. This is the coarsest grid used in the investigation, and we bilinearly interpolated other data at finer resolutions onto this grid. For our climatological analysis, we examine how cloud and meteorological properties covary as a function of grid box and long-term monthly mean. For our interannual analysis, we examine how monthly anomalies covary in each grid box. Long-term trends were removed from the anomalies in each grid box to avoid problems caused by possible low-frequency artifacts in the cloud data and reanalyses, but use of undetrended data has minimal impact on our results.

The domain for our investigation comprises all oceanic grid boxes within $30^\circ\mathrm{S} - 30^\circ\mathrm{N}$ that have long-term mean $\omega_{700} > 0$ for every calendar month and monthly mean $\omega_{700} > 0$ for at least 80% of the time record. We only examine anomalies for months with $\omega_{700} > 0$. This selection is loosely based on the methods of *Bony et al.* (2004), who divided the tropics into dynamical regimes according to

ω_{500} to quantify separately the thermodynamic and dynamic components of cloud changes in models from phase 3 of the Coupled Model Intercomparison Project (CMIP3) (*Meehl et al.*, 2007). Almost all of the grid boxes lie over eastern subtropical oceans and include stratocumulus and trade cumulus regions. The time periods for each dataset used in our investigation are listed in Table 2.1.

Statistical significance of various quantities is provided by a t test for the difference between two sample means. We take into account temporal and spatial autocorrelation by estimating, for each cloud variable, the ratio of the number of statistically independent points (effective number) to the nominal number of points. Our assumption is that the number of dependent points is equal to the lag at which the zonal, meridional, or temporal autocorrelation coefficients crosses zero. Before calculating zonal and meridional autocorrelation, we subtract the zonal mean of each latitude band and the meridional mean of each longitude band, respectively, for both the long-term monthly means and monthly anomalies. To calculate the temporal autocorrelation of the seasonal cycle and monthly anomalies, we subtract the long-term annual mean from each grid box. We find that one out of six points is independent zonally and one out of two meridionally, for both the climatological data and interannual anomalies. For months of the seasonal cycle, one out of three points is independent temporally. For the interannual analysis, between one out of eight (for ISCCP low+midlevel cloud-top height) and one out of two (for MODIS total cloud fraction) monthly anomalies are independent temporally.

2.2 Results

Figure 2.1 shows climatological annual mean low+midlevel CF, EIS, ω_{700}, and total LWP over the tropics. Grid boxes used in the investigation are marked with an ×. Regions of large CF generally coincide with regions of strong EIS and strong ω_{700}. It is also evident that EIS and ω_{700} are highly spatially correlated and have coinciding maxima, suggesting that they are tightly linked. This is consistent with the paradigm that the descending branches of the Hadley circulation and trade winds promote a strong capping inversion via subsidence warming and horizontal cold air advection. CF maxima, however, are not always collocated with the EIS and ω_{700} maxima near western coasts of continents. One reason is that outflow of dry air from the continents dries the MBL. Second, the 24–48-h response time of cloudiness to EIS changes causes CF maxima to be downstream from the EIS maxima closer to the coast (*Klein et al.*, 1995; *Mauger and Norris*, 2010). Third, very strong subsidence along the coast may suppress cloudiness, as proposed by *Simon* (1977) and consistent with *Mauger and Norris* (2010), who found that strong subsidence nearly instantaneously leads to a reduction in CF. The reduction of cloudiness along the coasts is even more prominent in total LWP (Fig. 2.1d).

To investigate the EIS–ω_{700} relationship more deeply, we calculate joint frequency distributions of EIS and ω_{700}. The joint frequency distributions of the climatology and interannual anomalies are shown in Fig. 2.2. The climatological distribution (Fig. 2.2a) is clearly elliptical in shape and slopes from weak EIS and weak ω_{700} to strong EIS and strong ω_{700} ($r = 0.48$). Surprisingly, the interannual monthly anomaly distribution (Fig. 2.2b) exhibits no such behavior ($r = 0.06$). In fact, the distribution is essentially symmetric about both axes and nonsloped. The positive correlation between EIS and ω_{700} evident over the climatology is consistent with a relationship physically linked through vertical warm air advection and horizontal cold air advection. In contrast, the nonexistent correlation for interannual monthly anomalies indicates that these mechanisms can be overwhelmed by other influences.

Next, we average all cloud property values falling into each EIS–ω_{700} bin. Figures 2.3a and 2.4a show, respectively, climatological variations and interannual anomalies of ISCCP low+midlevel CF as a function of EIS and ω_{700}. In the climatological plot, large CF (red) is found where EIS is strong and small CF (blue) is found where EIS is weak. This indicates that EIS is the dominant predictor of CF in the parameter space of the plot, consistent with results from previous studies (*Klein and Hartmann*, 1993; *Wood and Bretherton*, 2006; *Sun et al.*, 2011). Closer examination of both plots reveals the independent impacts of EIS and ω_{700} on cloudiness. The overall occurrence of the largest CF values in the lower right quadrants and the smallest CF values in the upper left quadrants suggest that, under conditions of strong EIS, weaker ω_{700} enhances CF and that, under conditions of weak EIS, stronger ω_{700} reduces CF. This behavior is especially evident in the interannual plot, suggesting that both EIS and ω_{700} play a significant role in interannual variations of CF. Vertical columns in Figs. 2.3a and 2.4a, corresponding to conditions of uniform EIS, generally exhibit decreasing CF from bottom (weak ω_{700}) to top (strong ω_{700}). Horizontal rows in Figs. 2.3a and 2.4a, corresponding to conditions of uniform ω_{700}, generally exhibit increasing CF from left (weak EIS) to right (strong EIS).

To more clearly discern the impact of subsidence on CF, we partitioned adjacent pairs of vertical columns into upper and lower halves according to the median ω_{700} value of the column pair (lines across Figs. 2.3a and 2.4a). We then calculated the difference in mean CF between these two subsets divided by the difference in mean ω_{700}. This is essentially a centered finite-differencing scheme for estimating the CF/ω_{700} slope. At each value of uniform EIS, increasing ω_{700} is associated with reduced CF (Figs. 2.3c and 2.4c). We also partitioned adjacent pairs of horizontal rows into upper and lower halves according to the median EIS value of the row pair (other set of lines across Figs. 2.3a and 2.4a). At each value of uniform ω_{700}, increasing EIS is associated with enhanced CF (Figs. 2.3b and 2.4b).

Changes in CF with ω_{700} or EIS for individual intervals displayed in Figs. 2.3b, 2.3c, 2.4b, and 2.4c are not always statistically significant due to the small sample size. For this reason we calculated changes in CF with ω_{700} or EIS, averaged over all intervals, with weighting according to the number of values in each interval. Partitioning into upper and lower ω_{700} subsets according to the median ω_{700} value over all EIS intervals is akin to calculating the total derivative $D(\mathrm{CF})/D(\omega_{700})$ since the variation of ω_{700} with EIS is not taken into account. For the climatological data, the upper subset has stronger average EIS than the lower subset. Partitioning according to the median ω_{700} value in each individual EIS interval is akin to calculating the partial derivative $\partial(\mathrm{CF})/\partial(\omega_{700})|_{\mathrm{EIS}}$ because the upper subset has the same average EIS value as the lower subset. We calculated the total derivative $D(\mathrm{CF})/D(\mathrm{EIS})$ and the partial derivative $\partial(\mathrm{CF})/\partial(\mathrm{EIS})|_{\omega 700}$ in a similar manner.

Table 2.2 lists total and partial derivative results for ISCCP low+midlevel CF, PATMOS-x low+midlevel CF, and MODIS total CF with CFSR EIS and ω_{700}. Similar results were obtained for each of the five primary MBL cloud regions (Table A2.1) and using EIS and ω_{700} from the other three reanalyses (Table A2.2). All three satellite datasets exhibit positive values of $D(\mathrm{CF})/D(\omega_{700})$ but negative values of $\partial(\mathrm{CF})/\partial(\omega_{700})|_{\mathrm{EIS}}$ for climatological relationships. This indicates that the geographical and seasonal association between greater cloud fraction and stronger subsidence is, in fact, driven by stronger temperature inversions. When EIS is held constant, subsidence actually reduces CF. In contrast, $\partial(\mathrm{CF})/\partial(\omega_{700})|_{\mathrm{EIS}}$ is nearly equal to $D(\mathrm{CF})/D(\omega_{700})$ for interannual anomalies, consistent with a near-zero correlation between EIS and ω_{700} over this time scale. In almost all cases, negative $\partial(\mathrm{CF})/\partial(\omega_{700})|_{\mathrm{EIS}}$ values are statistically significant. Table 2.2 also shows that the satellite datasets exhibit more positive values for $\partial(\mathrm{CF})/\partial(\mathrm{EIS})|_{\omega 700}$ than for $D(\mathrm{CF})/D(\mathrm{EIS})$ for the climatological relationships, while the interannual values are nearly equal. Although the difference in the former case is not statistically significant, it suggests that the effect of subsidence partially offsets the effect of inversion strength on geographical and seasonal variations of cloudiness. Standard deviations of EIS and ω_{700} for the climatological data are approximately 3 K and 10 hPa day^{-1}. Given the $\partial(\mathrm{CF})/\partial(\mathrm{EIS})|_{\omega 700}$ and $\partial(\mathrm{CF})/\partial(\omega_{700})|_{\mathrm{EIS}}$ values in Table 2.2, this indicates that EIS is the dominant predictor of climatological variations of CF. Standard deviations of EIS and ω_{700} for the interannual anomalies are approximately 1 K and 10 hPa day^{-1}, indicating that the two parameters are approximately equal contributors to interannual variations of CF.

Figures 2.5a and 2.6a show climatological and interannual UWISC total LWP as a function of EIS and ω_{700}. Compared to CF, LWP is much more sensitive to changes in ω_{700} than to EIS changes. In the climatological and especially the interannual plot, reduced LWP (blue) occurs with stronger subsidence and enhanced LWP (red) occurs with weaker subsidence. This suggests that ω_{700} is more dominant than EIS in predicting interannual variations of LWP. For each

EIS interval, LWP decreases as ω_{700} increases (Figs. 2.5c and 2.6c), with high statistical significance for the interannual relationships. For each ω_{700} interval in the climatological plot, LWP increases as EIS increases (Fig. 2.5b), but this effect is only statistically significant for middle values of ω_{700}.

Table 2.3 lists total and partial derivative results for UWISC LWP with CFSR EIS and ω_{700} (results using other reanalyses are in Table A2.3). Climatological and interannual values of $\partial(\mathrm{LWP})/\partial(\omega_{700})|_{\mathrm{EIS}}$ are negative and strongly statistically significant. Climatological values of $D(\mathrm{LWP})/D(\omega_{700})$ are less negative than values of $\partial(\mathrm{LWP})/\partial(\omega_{700})|_{\mathrm{EIS}}$, suggesting that strengthening of the temperature inversion partially offsets the reduction in LWP caused by stronger subsidence. Climatological values of $D(\mathrm{LWP})/D(\mathrm{EIS})$ are less positive than values of $\partial(\mathrm{LWP})/\partial(\mathrm{EIS})|_{\omega 700}$, suggesting that stronger subsidence partially offsets the enhancement of LWP caused by a stronger inversion. Interannual values of $D(\mathrm{LWP})/D(\mathrm{EIS})$ and $\partial(\mathrm{LWP})/\partial(\mathrm{EIS})|_{\omega 700}$ are near zero and slightly negative. Values derived from the other reanalyses are near zero or slightly positive. This indicates that EIS plays almost no role in interannual variations in LWP; rather, ω_{700} is the overwhelmingly dominant predictor here. Recalling the climatological standard deviations of EIS and ω_{700} noted earlier, it is clear that the two parameters contribute nearly equally to climatological variations of LWP.

Since total LWP retrievals include both cloudy and clear portions of the grid box, observed reductions in LWP caused by enhanced subsidence can result from decreased cloud thickness, decreased horizontal cloud fraction, and/or decreased liquid water content. The fact that CF responds less to subsidence, relative to EIS, than does LWP suggests that decreased cloud thickness is a substantial contributor to reduced LWP. We investigate this hypothesis by examining changes in cloud-top height z_{top}. Since no global multidecadal datasets of cloud-top height exist, we estimate z_{top} as $(\mathrm{SST} - T_{\mathrm{top}})/\Gamma$, where T_{top} is ISCCP low+midlevel cloud-top temperature, and Γ is the environmental lapse rate [assumed to be 7.1 Kkm^{-1} following *Minnis et al.* (1992)].

Figure 2.7a shows climatological z_{top} as a function of EIS and ω_{700}. It is apparent that z_{top} is lowest (<1400 m) when EIS and ω_{700} are both strong and highest (>2200 m) when EIS and ω_{700} are both weak. The physically plausible cloud-top height distribution provides confidence in the quality of the z_{top} estimates; a similar plot made using MODIS z_{top} looks qualitatively similar. Values of z_{top} decrease as EIS increases for each interval of ω_{700} (Fig. 2.7b), consistent with previous reports of lower MBL heights for stronger temperature inversions (*Norris*, 1998a). Values of z_{top} decrease as ω_{700} increases for intervals of EIS < 2 K (Fig. 2.7c), as might be expected from stronger subsidence pushing down cloud top. Although not statistically significant, z_{top} increases as ω_{700} increases for intervals of EIS > 2 K. It may be the case that this behavior in the climatology partially results from our assumption of a constant lapse rate. A shallower MBL under stronger subsidence is more likely to be well mixed and have a lapse rate closer to adiabatic (*Wood and Bretherton*, 2004), thus producing a colder cloud-top temperature as an alternative to greater cloud-top height. Assuming a fixed cloud-top height instead of a fixed lapse rate enabled us to test our hypothesis by creating a composite plot with lapse rate as a function of EIS and ω_{700} (not shown). Lapse rate did, indeed, become closer to adiabatic under stronger subsidence within the EIS > 2 K regime.

Figure 2.8 shows interannual anomalies in z_{top} as a function of EIS and ω_{700}. Values of z_{top} decrease as EIS increases for every interval of ω_{700}, and values of z_{top} decrease as ω_{700} increases for every interval of EIS. Although not shown, the MODIS z_{top} plot shows similar behavior. All of these relationships are statistically significant. Table 2.4 lists total and partial derivative results for ISCCP-derived z_{top} with CFSR EIS and ω_{700} (results using other reanalyses are in Table A2.4). Climatological and interannual values of $\partial(z_{\mathrm{top}})/\partial(\omega_{700})|_{\mathrm{EIS}}$ and $\partial(z_{\mathrm{top}})/\partial(\mathrm{EIS})|_{\omega700}$ are negative and statistically significant. Climatological values of $D(z_{\mathrm{top}})/D(\omega_{700})$ and $D(z_{\mathrm{top}})/D(\mathrm{EIS})$ are more negative than their respective partial derivatives, suggesting that the strengthening of the temperature inversion and stronger subsidence supplement each other in reducing cloud-top height.

For further insight into the response of cloudiness to changes in inversion strength and subsidence, we examine the climatological and interannual variations in the frequency of low cloud types reported by surface observers on ships. These provide a qualitative measure of the depth of and degree of mixing in the MBL. Ship sampling is sparse over many areas of the ocean, so we required at least 10 observations per month to create a monthly anomaly. Figure 2.9a shows the climatologically most frequently occurring low cloud type within each EIS–ω_{700} bin. The Sc-to-Cu transition is clearly apparent (*Wyant et al.*, 1997). Beginning in the upper right portion of the plot, where EIS and ω_{700} are strong, and proceeding to the lower left, where EIS and ω_{700} are weak, the dominant cloud types progress from stratocumulus and stratus (Sc+St) to cumulus under stratocumulus (Cu-under-Sc) to small cumulus (small Cu) and, finally, to large cumulus (large Cu). This transition in EIS, ω_{700}, and cloud types parallels what occurs along a trajectory following the trade winds over the eastern subtropical ocean (*Norris*, 1998b). The composite plots using the other reanalyses (not shown) behave similarly.

The climatological distribution of low cloud types with EIS and ω_{700} is also consistent with previous figures (Figs. 2.3a, 2.5a, and 2.7a). The middle right portion of the plot (strong EIS and median ω_{700}) is dominated by Sc+St. It has the largest CF, large LWP, and low z_{top}, as expected for relatively thick stratocumulus. The lower left portion of the plot (weak EIS and weak ω_{700}) is dominated by large Cu. It has relatively small CF, large LWP, and highest z_{top}, as expected for vertically extensive cumulus. The middle left portion of the plot (weak EIS and median ω_{700}) is dominated by small Cu, and occurrences of no low cloud are most frequent here. It has the smallest CF and smallest LWP, as expected for vertically limited cumulus or a cloudless MBL.

Figure 2.9b shows the low cloud type with the largest positive interannual anomaly in frequency of occurrence within each EIS-ω_{700} bin. Although not shown, composite plots using the other reanalyses look similar. For intervals of ω_{700} anomalies near zero, there is general progression from Sc+St to large Cu for positive to negative anomalies in EIS. This is associated with a decrease in CF, almost no change in LWP, and an increase in z_{top} (Figs. 2.4a, 2.6a, and 2.8a). For intervals of EIS anomalies near zero, there is general progression from Sc+St to small Cu for negative to positive anomalies in ω_{700}. This is associated with a decrease in CF, a large decrease in LWP, and a decrease in z_{top}. Although weaker

EIS and stronger subsidence both promote more cumulus and less stratocumulus, the differences in CF, LWP and z_{top} suggest that the underlying processes are not identical.

2.3 Conceptual model

We now consider a highly idealized one-dimensional conceptual model of a cloud within the MBL to understand how changes in subsidence and inversion strength independently affect cloud properties. We assume that the marine boundary layer is in equilibrium and ignore horizontal advection so that subsidence ω_{sub} balances the rate of entrainment ω_{ent} at cloud top (approximately the top of the MBL). For the monthly data on which our study is based, ignoring horizontal advection is reasonable (*Wood and Bretherton*, 2004; *Wang et al.*, 2011). We also assume that entrainment rate is inversely proportional to inversion strength, which is reasonable if we ignore variations in cloud-top radiative cooling and surface heating (*Lilly*, 1968). Figure 2.10 shows a schematic of our conceptual model. The lower troposphere has subsidence profile $\omega_{\text{sub}}(z)$ that is zero at the surface and increases monotonically with height. Cloud-top height z_{top} occurs at the elevation where ω_{ent} matches $\omega_{\text{sub}}(z)$. Stratocumulus cloud-base height z_{base} is at the saturation level for the upper part of the MBL and may differ from the lifting condensation level of surface air if the MBL is decoupled.

The schematic shows two possible pathways by which z_{top} decreases by some distance Δz. In the first case (Fig. 2.10a) we imagine that the vertical velocity profile is perturbed by some amount $\Delta\omega > 0$ so that subsidence increases throughout the lower troposphere. For simplicity, we assume that enhanced subsidence warming is offset by enhanced horizontal cold air advection or some other factor so that inversion strength, and therefore entrainment rate, does not change. To satisfy equilibrium, cloud top must decrease to some new height $z_{\text{top}} - \Delta z$ where the unchanged rate of entrainment balances the perturbed subsidence profile (*Schubert et al.*, 1979). Since the entrainment rate does not change, we assume that the relative humidity in the upper MBL does not change, implying no change in z_{base}. The net result is a reduction of cloud thickness and LWP. Subsidence may push the MBL top below the saturation level in some places (if cloud-base height is horizontally inhomogeneous) or all places (*Zhang et al.*, 2009). This will reduce CF and favor small cumulus. Although not illustrated in Fig. 2.10a, a weakening of subsidence with unchanged entrainment rate will promote increasing z_{top}, cloud thickness, LWP, CF, and stratocumulus (*Deardorff*, 1976; *Sandu and Stevens*, 2011). This is consistent with the large-eddy simulation results of *Blossey et al.* (2013) and *Bretherton et al.* (2013), who examined the response of stratocumulus, cumulus-under-stratocumulus, and shallow cumulus to idealized climate perturbations. For each cloud type, they found increased cloud thickness due to a rise in cloud top under reduced subsidence and warming SSTs compared to warming SSTs alone (with nearly the same slight increase in inversion strength for the two cases).

In the second case (Fig. 2.10b), we imagine that the vertical velocity profile is unchanged while the inversion becomes stronger and entrainment weakens. To satisfy equilibrium, cloud top must decrease to some new height $z_{\text{top}} - \Delta z$ where the reduced entrainment rate $\omega_{\text{ent}} - \Delta\omega$ balances lesser subsidence at lower elevation. Since the entrainment rate weakens, we assume there is less drying and the relative humidity in the upper MBL increases, resulting in a lowering of z_{base} by some distance Δz^*. If stratocumulus cloud base lowers more than cloud top ($\Delta z^* > \Delta z$), cloud thickness and LWP increase. If humidity is horizontally inhomogeneous, then moistening may lower the saturation level below the MBL top in some places. This will enhance CF and favor stratocumulus. This mechanism is consistent with the modeling results of *Bretherton et al.* (2013), who found that an increase in EIS for constant subsidence caused increased thickness of cumulus-under-stratocumulus and shallow cumulus due to cloud base lowering more than cloud top, and almost no change in stratocumulus thickness due to cloud base lowering approximately as much as cloud top. Although not illustrated in Fig. 2.10b, a reduction of inversion strength and enhancement of entrainment rate will promote rising z_{top} and increased MBL drying (*Deardorff*, 1976). This will favor large cumulus whereby an increase in cumulus thickness offsets the reduction in

LWP associated with smaller CF, perhaps explaining why LWP appears to be less sensitive to EIS changes than ω_{700} changes.

2.4 Conclusions

This study used a combination of satellite cloud data, visual cloud observations, and reanalysis meteorological parameters to investigate how variations in subsidence and inversion strength independently affect marine boundary layer cloud fraction, liquid water path, cloud-top height, and morphological cloud type. Compositing cloud data into intervals of estimated inversion strength and ω_{700} prevented the climatological association between stronger temperature inversions and stronger subsidence from producing a confounding correlation with cloudiness that affected previous studies. Using this approach, we have found the following.

- For uniform estimated inversion strength, enhanced subsidence reduces cloud fraction, total liquid water path, cloud-top height, and frequency of stratocumulus.
- For uniform subsidence, enhanced estimated inversion strength reduces cloud-top height but increases cloud fraction and frequency of stratocumulus.
- Estimated inversion strength is the dominant contributor to climatological variability in cloud fraction.
- Subsidence is the dominant contributor to interannual variability in liquid water path.
- Estimated inversion strength and subsidence contribute approximately equally to climatological variability in liquid water path and interannual variability in cloud fraction.

A simple conceptual model helps explain the above results by assuming that 1) subsidence balances entrainment at cloud top and 2) entrainment rate and drying is inversely proportional to inversion strength. Assuming no change in inversion strength, stronger subsidence pushes down cloud top and thereby reduces cloud thickness and cloud fraction. This favors small cumulus. Weaker subsidence allows cloud top to rise and thereby enhances cloud thickness and cloud fraction. This favors stratocumulus. Assuming no change in subsidence, a stronger inversion results in lower cloud top due to less entrainment but greater cloud thickness and cloud fraction due to less drying. This also favors stratocumulus. A weaker inversion results in higher cloud top due to more entrainment but reduced stratocumulus thickness and less cloud fraction due to more drying. This favors large cumulus.

Climatologically, inversion strength and subsidence are positively correlated. Thus, subsidence partially offsets enhanced cloud fraction due to a stronger inversion, and a stronger inversion partially offsets reduced liquid water path due to stronger subsidence. These cancelling effects, however, probably do not apply to projected climate change. Models currently predict that inversion strength over eastern subtropical oceans will increase, while subsidence will weaken (*Held and Soden*, 2006; *Vecchi and Soden*, 2007; *Webb et al.*, 2012). In this case, our results suggest that greater inversion strength and weaker subsidence will work together to favor greater marine boundary layer cloud fraction and liquid water path over eastern subtropical oceans. These processes act to increase albedo from cloudiness and may counteract other processes acting to decrease it, such as warmer sea surface temperature and greater downwelling radiation from more CO_2 in the atmosphere (*Norris and Leovy*, 1994; *Gregory and Webb*, 2008; *Blossey et al.*, 2013; *Bretherton et al.*, 2013). The effects of weakening subsidence on marine boundary layer cloudiness will likely exert a negative feedback to global warming that will oppose other positive cloud feedbacks.

Acknowledgments

This study was funded by NSF award AGS-0946094 and NASA Earth and Space Science graduate fellowship 12-EARTH12R-56. ISCCP data were downloaded from the Atmospheric Science Data Center located at NASA Langley Research Center. PATMOS-x data were provided by Amato Evan. UWISC data were provided by Chris ODell. MODIS data were obtained from the NASA Langley Research Center CERES ordering tool at http://ceres.larc.nasa.gov/; we use the CERES Terra SSF1deg-lite_Ed2.6 dataset. The CFSR and JRA-25 data were provided by the Data Support Section of the Computational and Information Systems Laboratory at the National Center for Atmospheric Research. NCAR is sponsored by the National Science Foundation. ERA-Interim data were downloaded from the ECMWF data server at data-portal.ecmwf.int. The Global Modeling and Assimilation Office and the Goddard Earth Sciences Data and Information Services Center provided the MERRA data. The authors thank several individuals whose contributions immensely improved the present study. Amy Clement suggested investigating liquid water path in addition to cloud fraction. A plot created by Rob Wood and one of his undergraduate assistants encouraged the authors to pursue the compositing techniques of the present study. Chris Bretherton provided helpful comments on a draft manuscript. The authors lastly thank Steve Klein and two anonymous reviewers for insightful comments and suggestions. This chapter is published in its entirety in **Myers, T.A., and Norris, J.R., "Observational evidence that enhanced subsidence reduces subtropical marine boundary layer cloudiness", *J. Climate*, 26(19), 2013**. The dissertation author was the primary investigator and author of this paper.

Tables and Figures

Table 2.1: Summary of data used in the investigation.

Cloud dataset	Time period used	Variables used
ISCCP	1984–2009	Low+midlevel CF, T_{top}
PATMOS-x	1984–2007	Low+midlevel CF
UWISC	1988–2008	Total LWP
MODIS	2001–09	Total CF, z_{top}
EECRA	1979–2008	Cloud-type frequency of occurrence
Reanalyses		
CFSR	Coincident w/paired cloud data	SST, SLP, T_{700}, z_{700}, ω_{700}
ERA-Interim	Same	Same
JRA-25	Same but through 2007	Same
MERRA	Same	Same

Table 2.2: Ratio of average CF difference over average CFSR ω_{700} or EIS difference for above- and below-median ω_{700} or EIS. Boldface and italicized text indicates statistical significance at the 90% level.

	Climatological value			Interannual value			
Estimate	ISCCP low+mid	PATMOS-x low+mid	MODIS total	ISCCP low+mid	PATMOS-x low+mid	MODIS total	Units
$D(\mathrm{CF})/D(\omega_{700})$	***2.6 ± 1.9***	1.4 ± 1.6	***2.6 ± 1.7***	***−0.86 ± 0.16***	***−0.6 ± 0.2***	***−1.2 ± 0.24***	$\%\ 10\,\mathrm{hPa}^{-1}\,\mathrm{day}^{-1}$
$\partial(\mathrm{CF})/\partial(\omega_{700})\|_{\mathrm{EIS}}$	***−2.4 ± 2.1***	***−2.4 ± 1.8***	−1.5 ± 1.9	***−0.9 ± 0.16***	***−0.62 ± 0.2***	***−1.2 ± 0.24***	$\%\ 10\,\mathrm{hPa}^{-1}\,\mathrm{day}^{-1}$
$D(\mathrm{CF})/D(\mathrm{EIS})$	***4.3 ± 0.59***	***3.5 ± 0.53***	***4 ± 0.59***	***1.1 ± 0.21***	***0.85 ± 0.27***	***1.2 ± 0.35***	$\%\ \mathrm{K}^{-1}$
$\partial(\mathrm{CF})/\partial(\mathrm{EIS})\|_{\omega700}$	***4.9 ± 0.68***	***4 ± 0.61***	***4.4 ± 0.68***	***1.1 ± 0.21***	***0.9 ± 0.27***	***1.3 ± 0.35***	$\%\ \mathrm{K}^{-1}$

Table 2.3: As in Table 2.2, but for LWP.

Estimate	Climatological value UWISC total	Interannual value UWISC total	Units
$D(\mathrm{LWP})/D(\omega_{700})$	−2 ± 2.1	***−3 ± 0.42***	$\mathrm{g\,m}^{-2}\ 10\,\mathrm{hPa}^{-1}\,\mathrm{day}^{-1}$
$\partial(\mathrm{LWP})/\partial(\omega_{700})\|_{\mathrm{EIS}}$	***−5.3 ± 2.2***	***−3.1 ± 0.42***	$\mathrm{g\,m}^{-2}\ 10\,\mathrm{hPa}^{-1}\,\mathrm{day}^{-1}$
$D(\mathrm{LWP})/D(\mathrm{EIS})$	***1.1 ± 0.81***	−0.56 ± 0.57	$\mathrm{g\,m}^{-2}\,\mathrm{K}^{-1}$
$\partial(\mathrm{LWP})/\partial(\mathrm{EIS})\|_{\omega700}$	***2.5 ± 0.9***	−0.28 ± 0.57	$\mathrm{g\,m}^{-2}\,\mathrm{K}^{-1}$

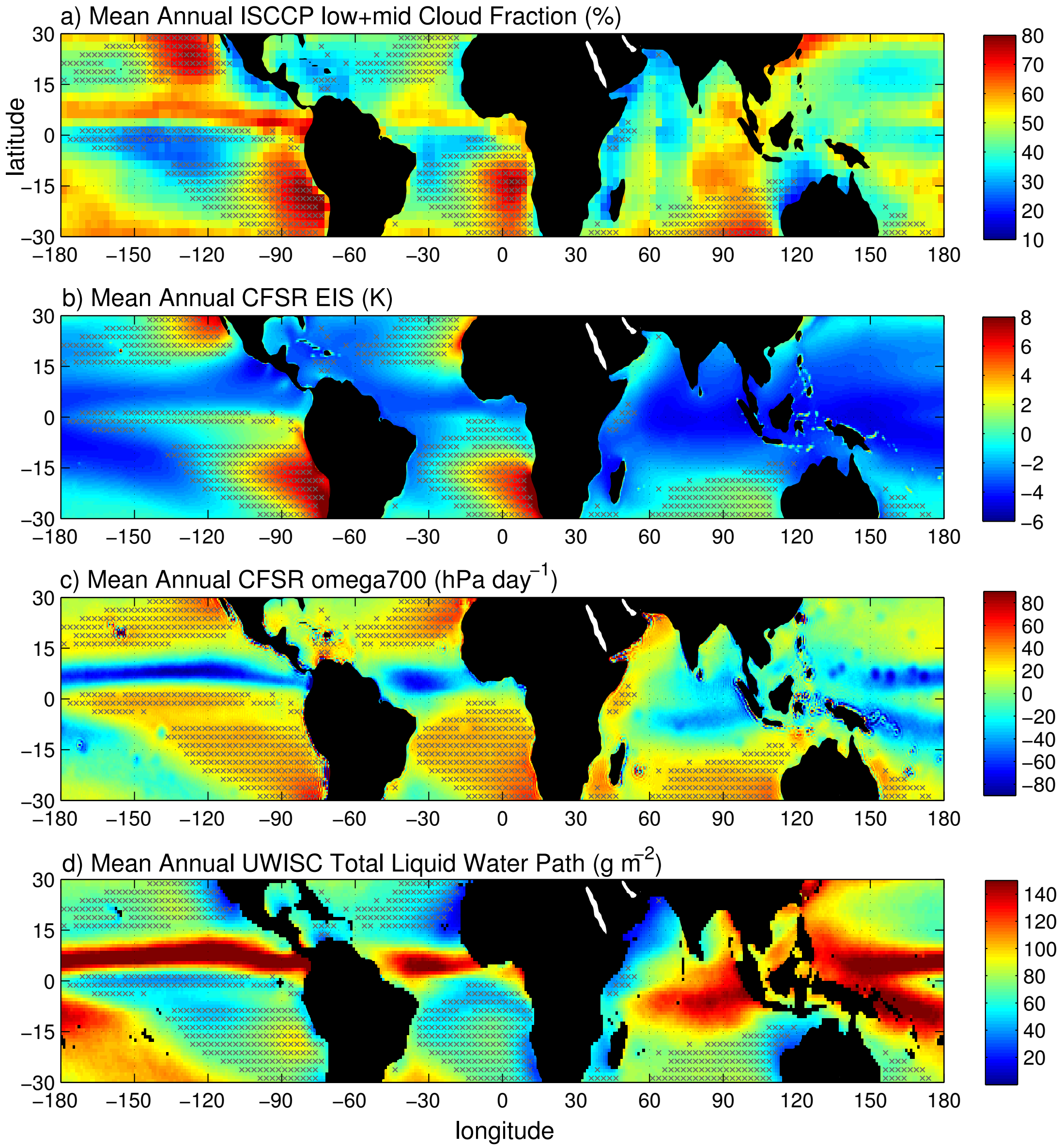

Figure 2.1: (a) 1984–2009 mean annual ISCCP low+midlevel cloud fraction, (b) CFSR estimated inversion strength, (c) CFSR pressure vertical velocity at 700 hPa, and (d) 1988–2008 mean annual UWISC total liquid water path. The × indicates grid boxes used in subsequent analyses.

Table 2.4: As in Table 2.2, but for z_{top}.

Estimate	Climatological value ISCCP low+mid	Interannual value ISCCP low+mid	Units
$D(z_{\text{top}})/D(\omega_{700})$	***−135 ± 45***	***−47 ± 9***	$\text{m}\,10\,\text{hPa}^{-1}\,\text{day}^{-1}$
$\partial(z_{\text{top}})/\partial(\omega_{700})\vert_{\text{EIS}}$	***−75 ± 51***	***−44 ± 9***	$\text{m}\,10\,\text{hPa}^{-1}\,\text{day}^{-1}$
$D(z_{\text{top}})/D(\text{EIS})$	***−69 ± 17***	***−87 ± 11***	$\text{m}\,\text{K}^{-1}$
$\partial(z_{\text{top}})/\partial(\text{EIS})\vert_{\omega 700}$	***−55 ± 20***	***−83 ± 11***	$\text{m}\,\text{K}^{-1}$

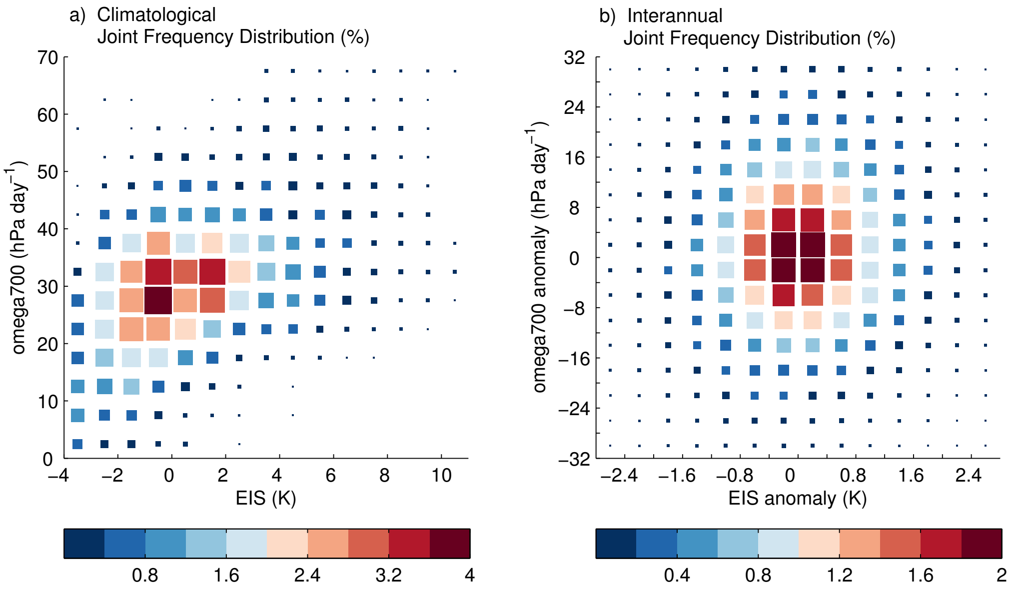

Figure 2.2: EIS–ω_{700} joint frequency distributions of (a) 1984–2009 CFSR geographical and seasonal climatology and (b) interannual anomalies. In each plot, the size of the box within each bin is proportional to the number of values contributing to the average.

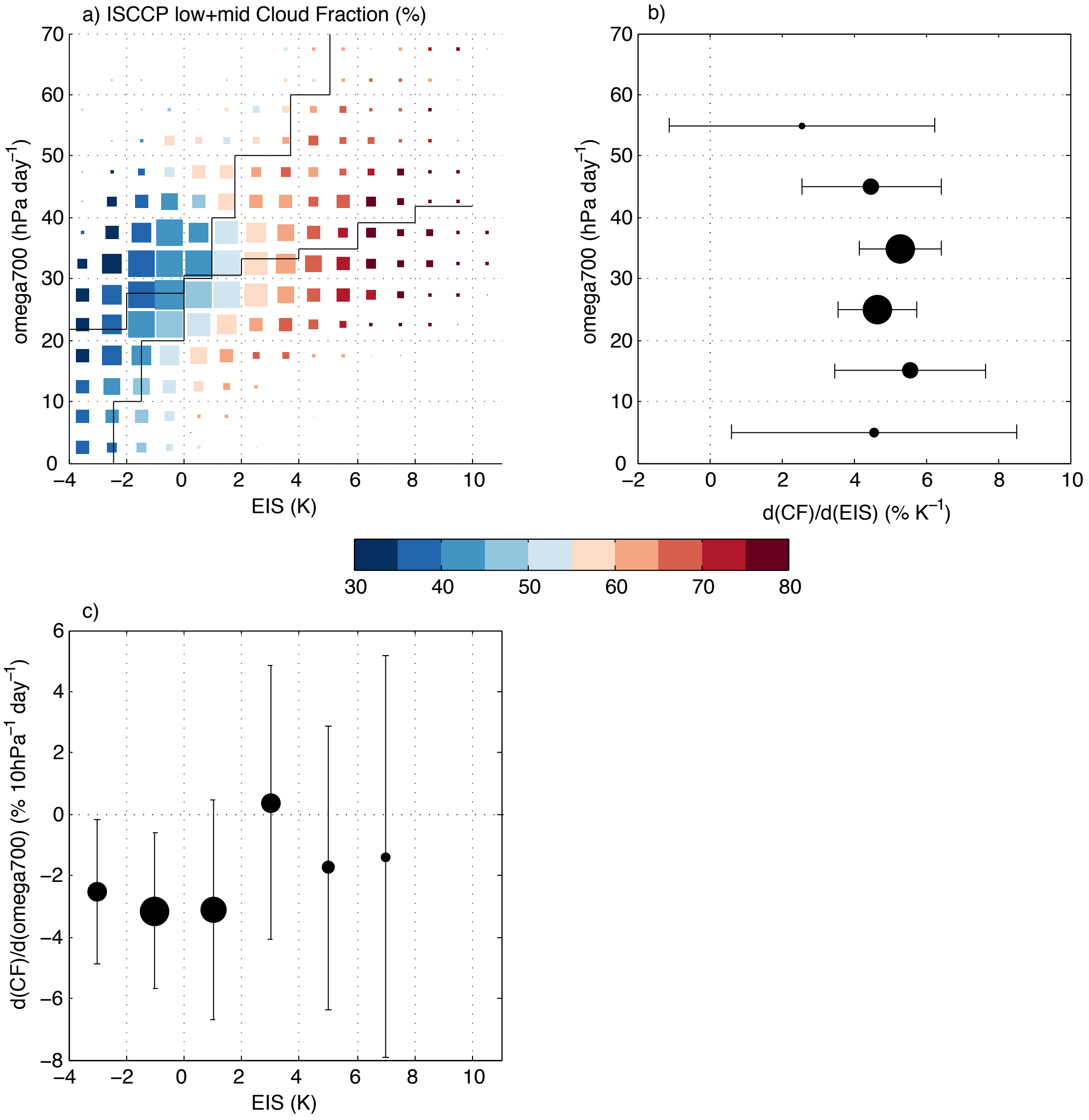

Figure 2.3: (a) Average ISCCP low+midlevel CF plotted as colors in EIS–ω_{700} bins for the geographical and seasonal climatology. (b) Ratio of the difference in average CF over the difference in average EIS for above- and below-median EIS in each ω_{700} interval. (c) Ratio of the difference in average CF over the difference in average ω_{700} for above- and below-median ω_{700} in each EIS interval. Error bars indicate 90% confidence limits. In each plot, the size of the box within each bin or circle within each interval is proportional to the number of values contributing to the average. Also, the black solid lines in (a) demarcate the median EIS values used in (b) and median ω_{700} values used in (c).

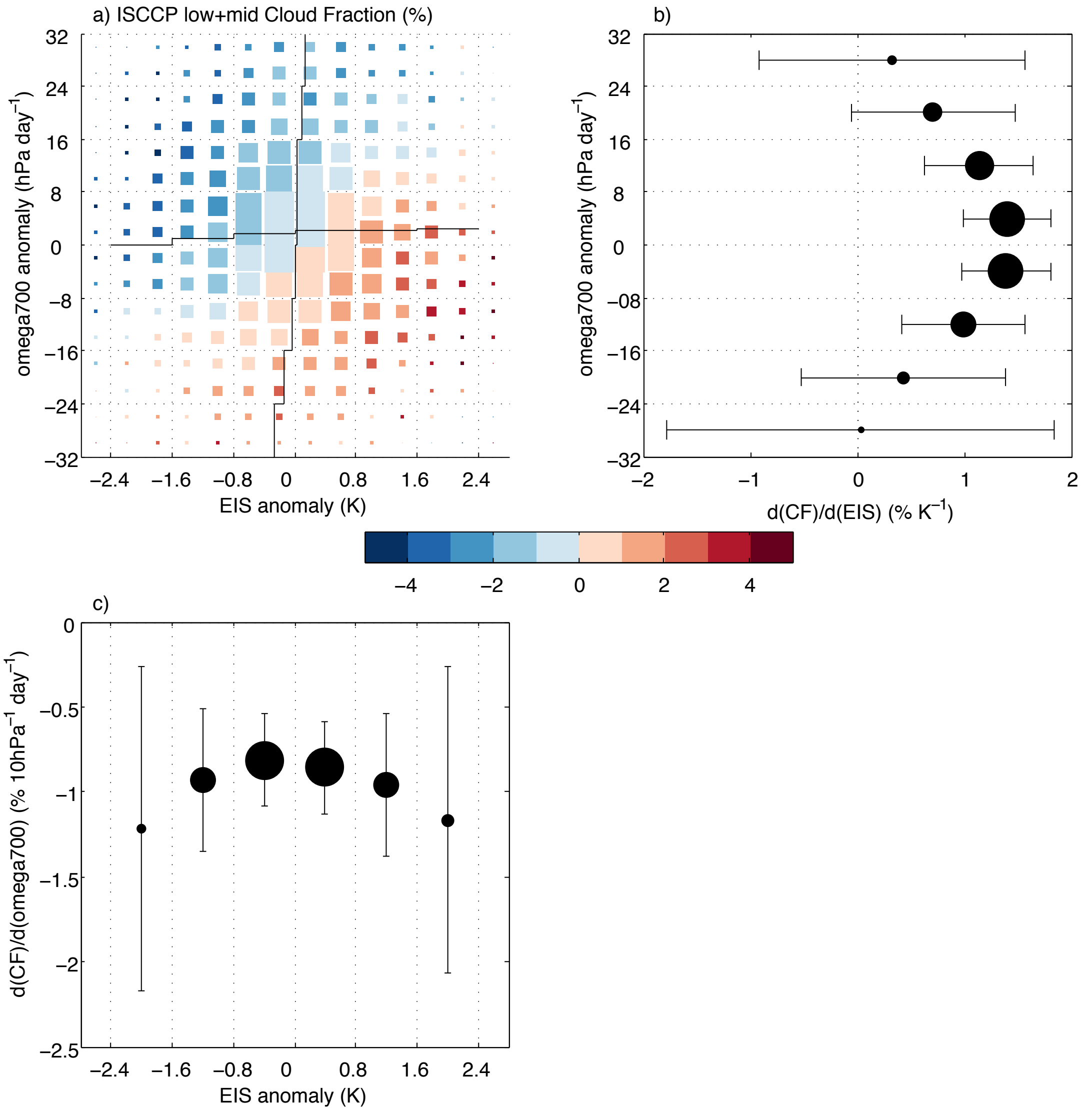

Figure 2.4: As in Fig. 2.3, but for ISCCP low+midlevel CF interannual anomalies.

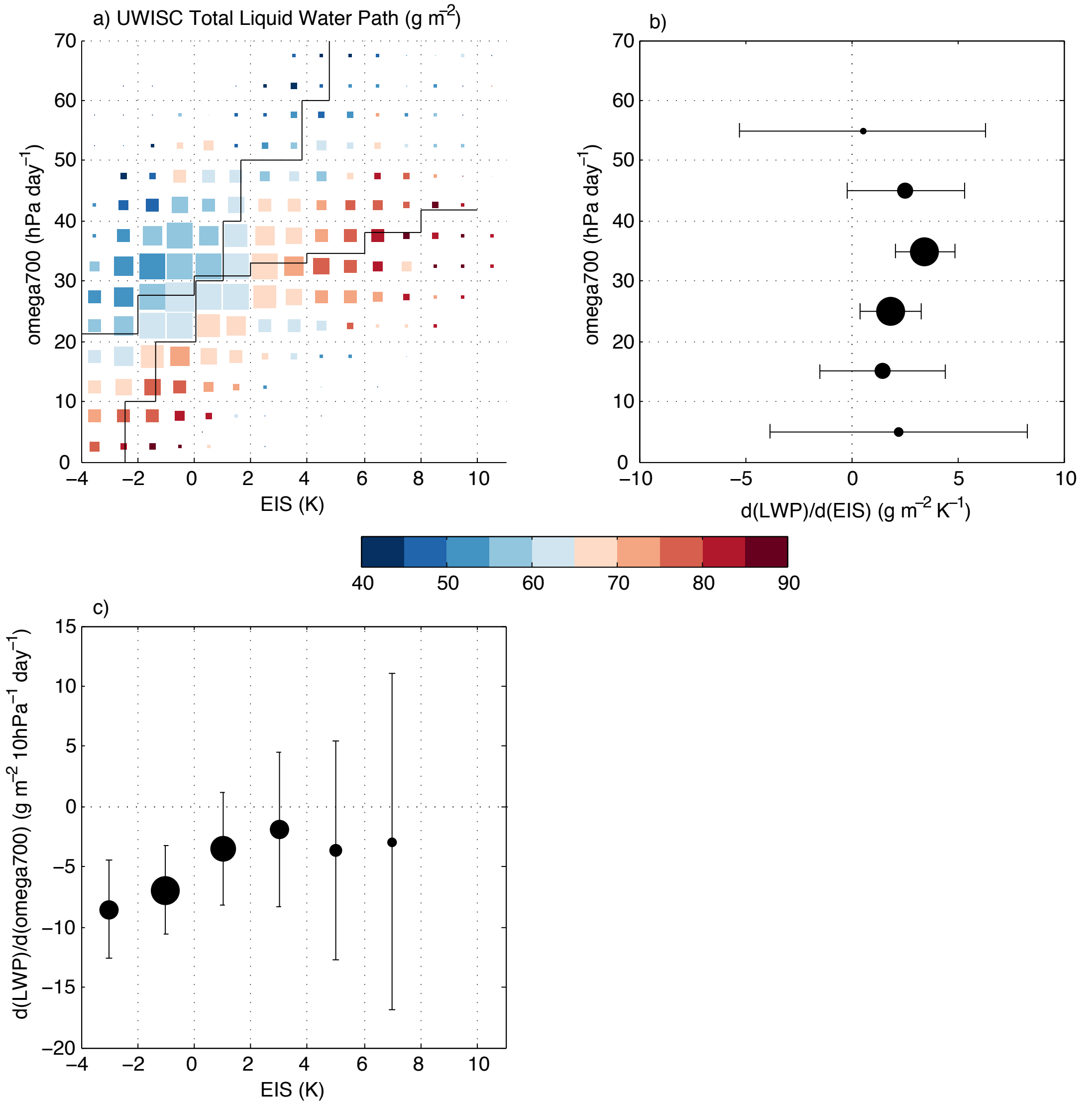

Figure 2.5: As in Fig. 2.3, but for UWISC total LWP geographical and seasonal climatology.

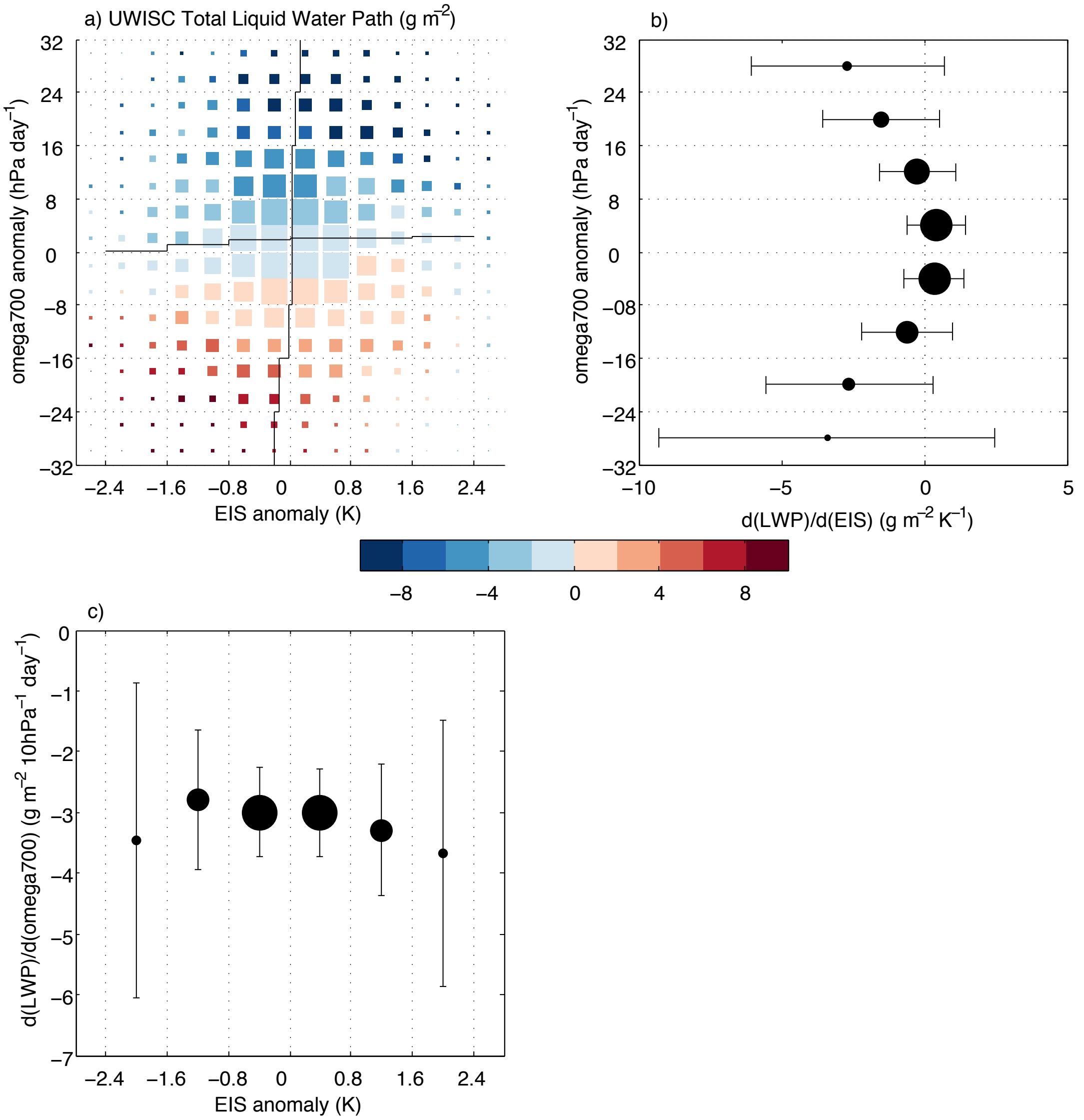

Figure 2.6: As in Fig. 2.3, but for UWISC total LWP interannual anomalies.

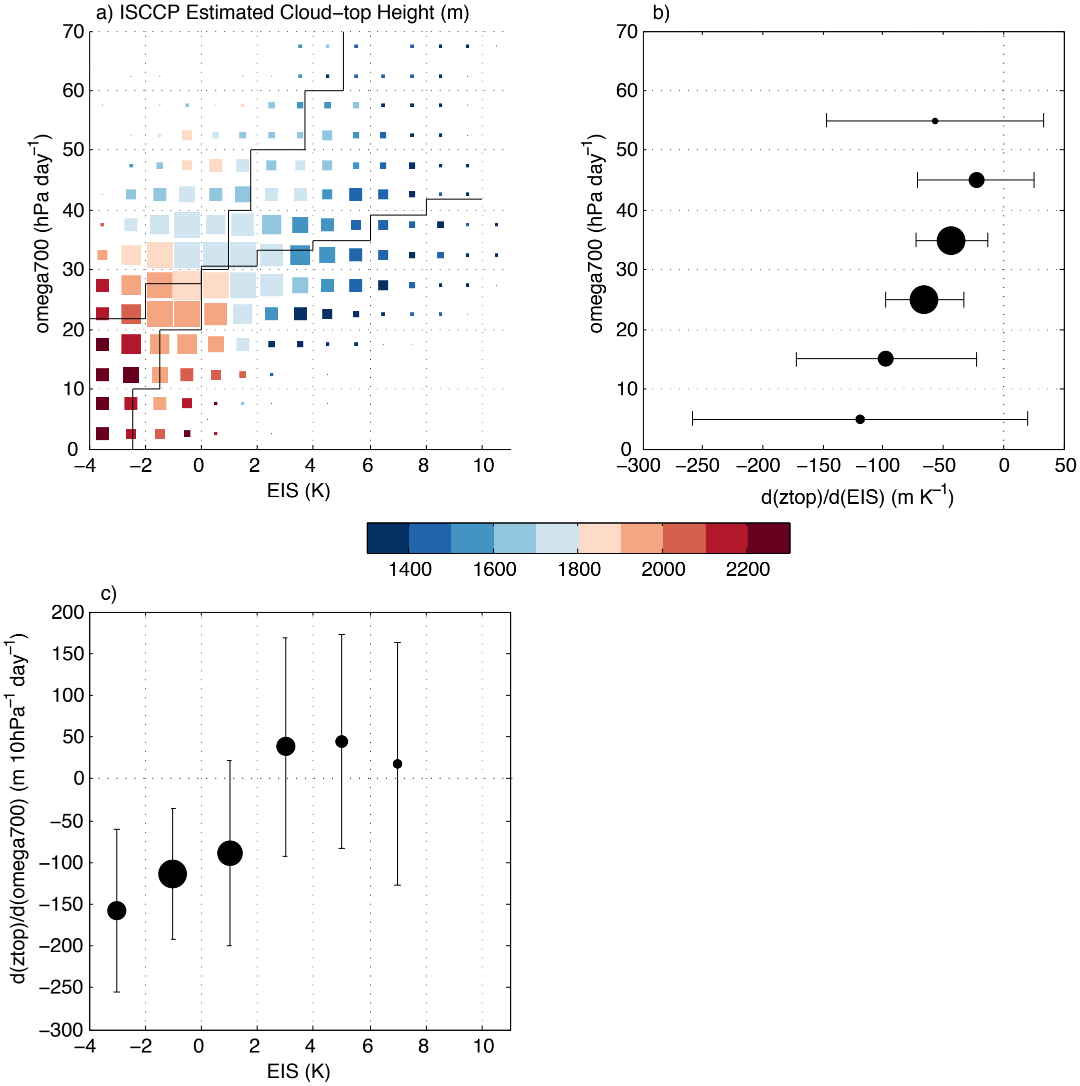

Figure 2.7: As in Fig. 2.3, but for ISCCP estimated cloud-top height geographical and seasonal climatology.

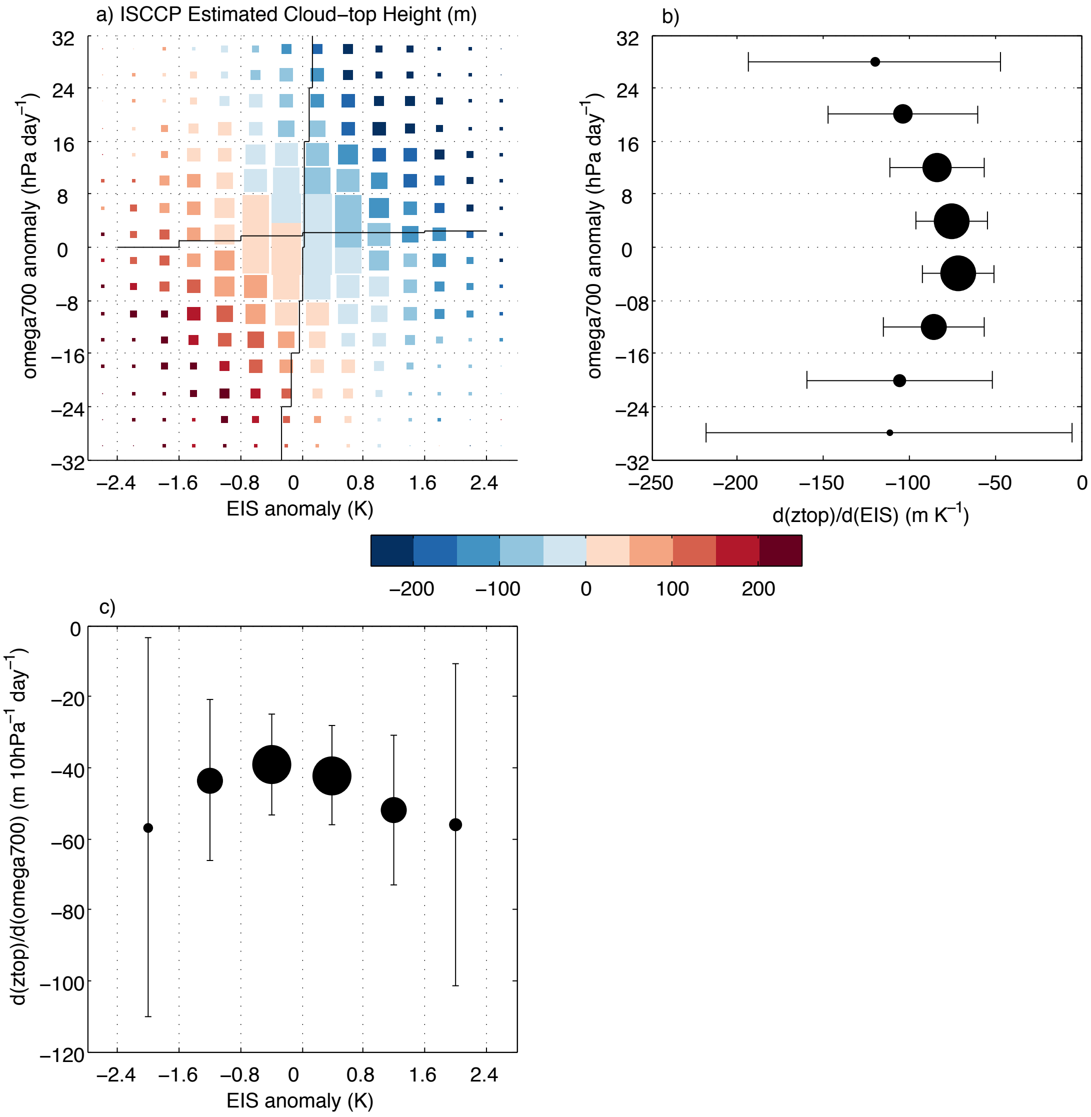

Figure 2.8: As in Fig. 2.3, but for ISCCP estimated cloud-top height interannual anomalies.

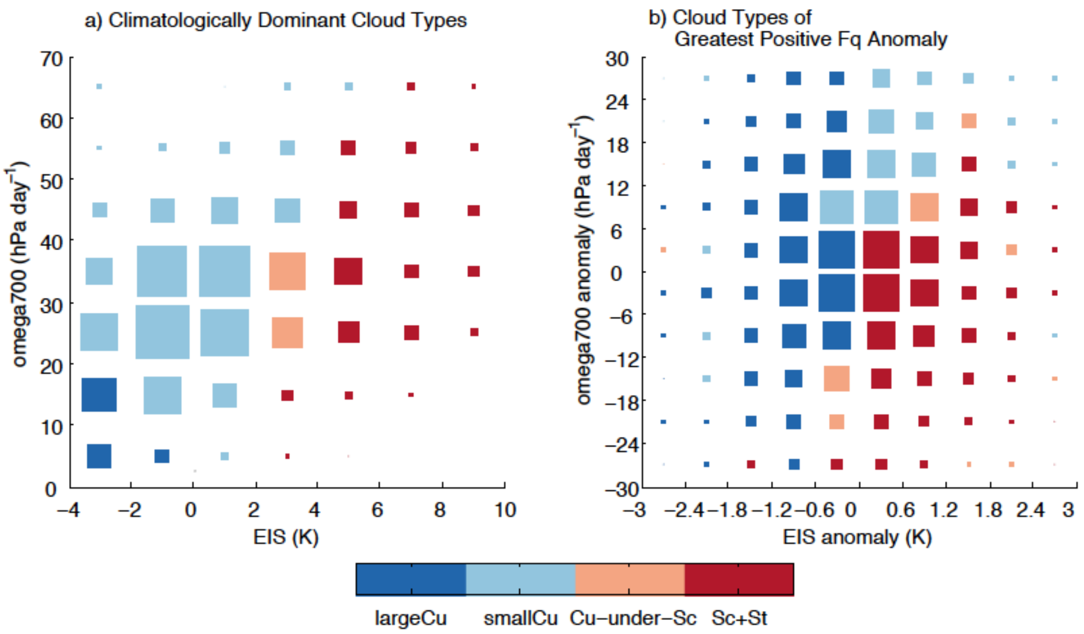

Figure 2.9: (a) Most frequently occurring low cloud type plotted as colors in EIS–ω_{700} bins for the geographical and seasonal climatology and (b) low cloud type with the largest positive interannual anomaly in frequency of occurrence. In each plot the size of the box within each bin is proportional to the number of contributing values. Sc+St includes C_L 5 (stratocumulus) and C_L 6 (fair-weather stratus). Cu-under-Sc includes C_L 8 (cumulus occurring with stratocumulus but not spreading into it) and C_L 4 (cumulus spreading into stratocumulus). SmallCu includes C_L 1 (cumulus with little vertical extent) and C_L 0 (no low cloud present). LargeCu is C_L 2 (cumulus with moderate or large vertical extent). See Table 1 of *Norris* (1998a) for details.

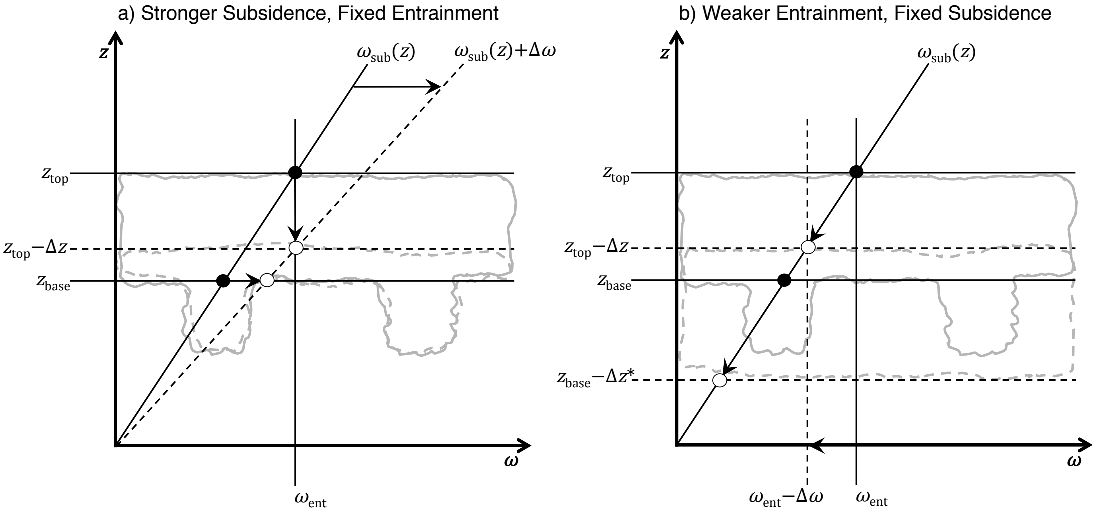

Figure 2.10: Conceptual model of cloud-top and cloud-base height variations due to changes in subsidence and inversion strength for an MBL in equilibrium. The lower troposphere has a monotonic subsidence profile $\omega_{\mathrm{sub}}(z)$ [solid diagonal line in (a) and (b)] that is zero at the surface. Cloud-top height z_{top} occurs where entrainment rate ω_{ent} matches $\omega_{\mathrm{sub}}(z_{\mathrm{top}})$ [filled circles in (a) and (b)], and stratocumulus cloud-base height z_{base} is at the saturation level for the upper part of the MBL (other filled circles). The diagram shows two possible pathways by which z_{top} decreases by some distance Δz. Gray solid (dashed) lines illustrate initial (final) cloud states. In (a), the vertical velocity profile is perturbed by $\Delta\omega > 0$ so that subsidence increases throughout the lower troposphere (dashed diagonal line) with no change in inversion strength or ω_{ent}. For equilibrium, cloud top must decrease to new height $z_{\mathrm{top}} - \Delta z$ (dashed horizontal line) where ω_{ent} balances $\omega_{\mathrm{sub}}(z_{\mathrm{top}} - \Delta z) + \Delta\omega$ [open circle in (a)]. We assume that no change in ω_{ent} results in no change in MBL moisture and no change in z_{base} [other open circle in (a)]. The net result is a reduction of cloud thickness. In (b), the vertical velocity profile is unchanged while the inversion strengthens and entrainment weakens by $\Delta\omega$ (dashed vertical line). For equilibrium, cloud top must decrease to new height $z_{\mathrm{top}} - \Delta z$ (dashed horizontal line) where $\omega_{\mathrm{ent}} - \Delta\omega$ balances $\omega_{\mathrm{sub}}(z_{\mathrm{top}} - \Delta z)$ [open circle in (b)]. We assume the MBL moistens due to less entrainment drying, resulting in a lowering of z_{base} by some distance Δz^* [other open circle in (b)]. If $\Delta z^* > \Delta z$, cloud thickness increases.

Appendix

Results for Individual MBL Cloud Regions, Additional Reanalyses, and Different Satellite Cloud Datasets

We checked to see whether the climatological relationships found in the investigation individually hold for the five primary MBL cloud regions (clearly evident in Fig. 2.1) within our domain. The total and partial derivative values for cloud fraction, liquid water path, and z_{top} with respect to estimated inversion strength or ω_{700} for each individual region are similar to those attained using climatological data from all regions. CF/EIS and CF/ω_{700} slope values for each individual region are displayed in Table A2.1. Enhanced subsidence, independent of inversion strength, reduces cloud fraction in all regions except for the southeast Indian Ocean. Statistical significance of quantities is less than when all regions are used to compute the slopes because of reduced sample size. To ensure robustness of the results, we also used four reanalyses (CFSR, ERA-Interim, JRA-25, and MERRA). Tables A2.2, A2.3, and A2.4 list the same partial and total derivatives as in Tables 2.2, 2.3, and 2.4, except derived from the other reanalyses. Results are in most cases quantitatively similar, especially within the range of uncertainty. We also repeated the analysis for ISCCP data that were not corrected for artifacts and for ISCCP, PATMOS-x, and UWISC anomalies without the long-term trends removed. The results (not shown) are robust to these choices of data.

Table A2.1: As in Table 2.2, but for climatological estimates for ISCCP low1midlevel cloud fraction in each primary MBL cloud region within the domain. Derivatives are with respect to EIS or ω_{700} from CFSR (top), ERA-Interim (second from top), JRA-25 (second from bottom), and MERRA (bottom).

MBL cloud region					
Northeast Pacific	Southeast Pacific	Northeast Atlantic	Southeast Atlantic	Southeast Indian	Units
		$D(\mathrm{CF})/D(\omega_{700})$			
3.3 ± 4.9	3.1 ± 4.6	1.2 ± 2.2	***5 ± 4.7***	***5.2 ± 2.8***	% 10 hPa^{-1} day^{-1}
6.7 ± 4.7	***12.1 ± 4.5***	0.64 ± 2.6	***7 ± 5.4***	***4.8 ± 2.6***	
2.1 ± 5.8	***5.3 ± 6.2***	0.94 ± 4.2	3.3 ± 6.4	***4.6 ± 2.8***	
5.7 ± 5	***12 ± 4.4***	1 ± 3.2	***12 ± 5***	***4.5 ± 2.9***	
		$\partial(\mathrm{CF})/\partial(\omega_{700})\vert_{\mathrm{EIS}}$			
−3.6 ± 5.8	−2.8 ± 4.9	−0.4 ± 3.2	−1.7 ± 5.6	3 ± 3.7	% 10 hPa^{-1} day^{-1}
−1.1 ± 6.2	0.69 ± 6.8	−0.41 ± 3.6	−1.2 ± 6.9	3.1 ± 3.3	
−4.3 ± 6.4	−1.7 ± 7.4	0.1 ± 5.4	−4.5 ± 7.5	3.1 ± 3.5	
−2.4 ± 6.5	−0.78 ± 6.6	0.1 ± 4.4	0.26 ± 7.6	1.8 ± 3.8	
		$D(\mathrm{CF})/D(\mathrm{EIS})$			
5.2 ± 1.3	***5.1 ± 0.86***	***2.2 ± 1.4***	***4.7 ± 1.2***	***3.7 ± 2.3***	% K^{-1}
5 ± 1.3	***5.7 ± 1***	***1.9 ± 1.8***	***5.3 ± 1.2***	***3.5 ± 2.5***	
3.7 ± 1.3	***5.6 ± 0.87***	1.1 ± 2.3	***5 ± 1.3***	***3.2 ± 2.5***	
5.1 ± 1.3	***5.8 ± 0.96***	1.5 ± 2.1	***5.2 ± 1.2***	***3.6 ± 2.5***	
		$\partial(\mathrm{CF})/\partial(\mathrm{EIS})\vert_{\omega700}$			
5.6 ± 1.8	***5.5 ± 1.1***	2.2 ± 2.5	***4.8 ± 1.5***	2.8 ± 2.9	% K^{-1}
5.3 ± 2.2	***5.2 ± 2***	2 ± 2.6	***5.4 ± 1.8***	2.3 ± 3.1	
4.4 ± 1.7	***5.9 ± 1.3***	0.96 ± 3.1	***5.5 ± 1.7***	2.2 ± 3.2	
5.6 ± 2.1	***5.5 ± 1.8***	1.2 ± 3	***4.7 ± 2***	2.4 ± 3.2	

Table A2.2: As in Table 2.2, but for derivative estimates with respect to EIS and ω_{700} from (top) ERA-Interim, (middle) JRA-25, and (bottom) MERRA.

Climatological value			Interannual value			
ISCCP low+mid	PATMOS-x low+mid	MODIS total	ISCCP low+mid	PATMOS-x low+mid	MODIS total	Units
		$D(\mathrm{CF})/D(\omega_{700})$				
6.3 ± 1.9	***4.8 ± 1.7***	***5.2 ± 1.8***	***−0.8 ± 0.22***	***−0.45 ± 0.28***	***−1.1 ± 0.34***	% 10 hPa^{-1} day^{-1}
3.5 ± 2.6	***2 ± 2.3***	1.2 ± 2.5	***−0.78 ± 0.24***	***−0.43 ± 0.3***	***−1 ± 0.4***	
6.3 ± 2	***4.9 ± 1.8***	***4.9 ± 1.9***	***−0.97 ± 0.23***	***−0.64 ± 0.3***	***−1.7 ± 0.36***	
		$\partial(\mathrm{CF})/\partial(\omega_{700})\vert_{\mathrm{EIS}}$				
0.35 ± 2.4	−0.2 ± 2.1	0.56 ± 2.1	***−0.95 ± 0.22***	***−0.56 ± 0.28***	***−1.3 ± 0.34***	% 10 hPa^{-1} day^{-1}
−2.4 ± 3	***−3 ± 2.6***	−2.1 ± 2.7	***−0.98 ± 0.24***	***−0.6 ± 0.3***	***−1.1 ± 0.4***	
−1.3 ± 2.6	−1.4 ± 2.3	−0.5 ± 2.3	***−1.2 ± 0.23***	***−0.79 ± 0.29***	***−1.8 ± 0.36***	
		$D(\mathrm{CF})/D(\mathrm{EIS})$				
4.2 ± 0.66	***3.6 ± 0.59***	***4 ± 0.63***	***1.9 ± 0.24***	***1.5 ± 0.31***	***2.3 ± 0.39***	% K^{-1}
4.5 ± 0.65	***3.8 ± 0.58***	***4.3 ± 0.63***	***1.9 ± 0.25***	***1.7 ± 0.31***	***2 ± 0.44***	
4.7 ± 0.66	***4 ± 0.59***	***4.3 ± 0.6***	***1.7 ± 0.24***	***1.3 ± 0.31***	***2.1 ± 0.38***	
		$\partial(\mathrm{CF})/\partial(\mathrm{EIS})\vert_{\omega700}$				
4.3 ± 0.84	***3.7 ± 0.74***	***4 ± 0.8***	***2 ± 0.25***	***1.6 ± 0.32***	***2.4 ± 0.39***	% K^{-1}
5 ± 0.77	***4.3 ± 0.69***	***4.5 ± 0.71***	***2 ± 0.25***	***1.7 ± 0.31***	***2.1 ± 0.44***	
4.8 ± 0.91	***4.2 ± 0.81***	***4.3 ± 0.75***	***1.8 ± 0.24***	***1.4 ± 0.31***	***2.2 ± 0.38***	

Table A2.3: As in Table A2.2, but for LWP

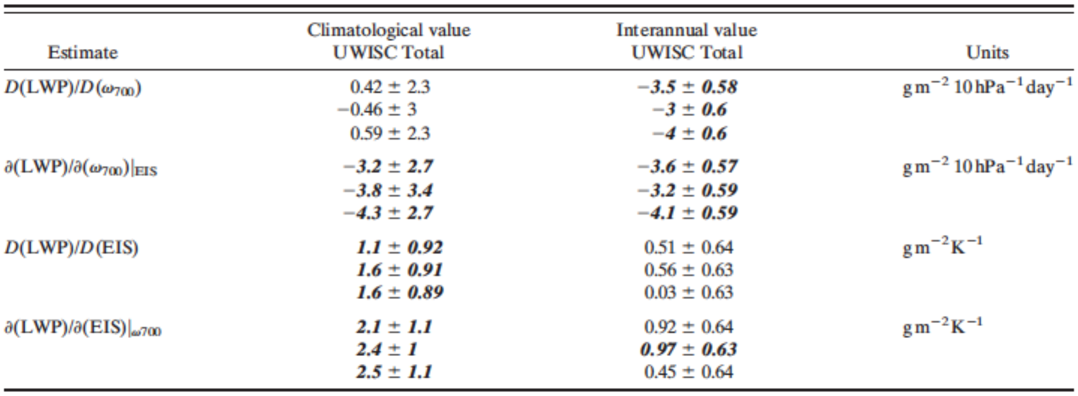

Estimate	Climatological value UWISC Total	Interannual value UWISC Total	Units
$D(\mathrm{LWP})/D(\omega_{700})$	0.42 ± 2.3 −0.46 ± 3 0.59 ± 2.3	***−3.5 ± 0.58*** ***−3 ± 0.6*** ***−4 ± 0.6***	$\mathrm{g\,m^{-2}\,10\,hPa^{-1}\,day^{-1}}$
$\partial(\mathrm{LWP})/\partial(\omega_{700})\|_{\mathrm{EIS}}$	***−3.2 ± 2.7*** ***−3.8 ± 3.4*** ***−4.3 ± 2.7***	***−3.6 ± 0.57*** ***−3.2 ± 0.59*** ***−4.1 ± 0.59***	$\mathrm{g\,m^{-2}\,10\,hPa^{-1}\,day^{-1}}$
$D(\mathrm{LWP})/D(\mathrm{EIS})$	***1.1 ± 0.92*** ***1.6 ± 0.91*** ***1.6 ± 0.89***	0.51 ± 0.64 0.56 ± 0.63 0.03 ± 0.63	$\mathrm{g\,m^{-2}\,K^{-1}}$
$\partial(\mathrm{LWP})/\partial(\mathrm{EIS})\|_{\omega 700}$	***2.1 ± 1.1*** ***2.4 ± 1*** ***2.5 ± 1.1***	0.92 ± 0.64 ***0.97 ± 0.63*** 0.45 ± 0.64	$\mathrm{g\,m^{-2}\,K^{-1}}$

Table A2.4: As in Table A2.2, but for z_{top}

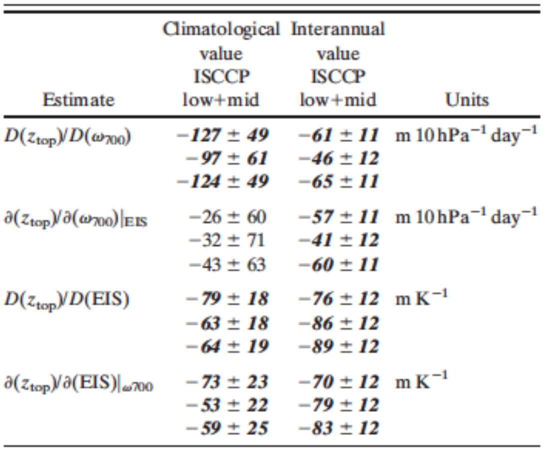

Estimate	Climatological value ISCCP low+mid	Interannual value ISCCP low+mid	Units
$D(z_{\mathrm{top}})/D(\omega_{700})$	***−127 ± 49*** ***−97 ± 61*** ***−124 ± 49***	***−61 ± 11*** ***−46 ± 12*** ***−65 ± 11***	$\mathrm{m\,10\,hPa^{-1}\,day^{-1}}$
$\partial(z_{\mathrm{top}})/\partial(\omega_{700})\|_{\mathrm{EIS}}$	−26 ± 60 −32 ± 71 −43 ± 63	***−57 ± 11*** ***−41 ± 12*** ***−60 ± 11***	$\mathrm{m\,10\,hPa^{-1}\,day^{-1}}$
$D(z_{\mathrm{top}})/D(\mathrm{EIS})$	***−79 ± 18*** ***−63 ± 18*** ***−64 ± 19***	***−76 ± 12*** ***−86 ± 12*** ***−89 ± 12***	$\mathrm{m\,K^{-1}}$
$\partial(z_{\mathrm{top}})/\partial(\mathrm{EIS})\|_{\omega 700}$	***−73 ± 23*** ***−53 ± 22*** ***−59 ± 25***	***−70 ± 12*** ***−79 ± 12*** ***−83 ± 12***	$\mathrm{m\,K^{-1}}$

Chapter 3

On the Relationships between Subtropical Clouds and Meteorology in Observations and CMIP3 and CMIP5 Models

Estimates of the global mean equilibrium temperature response due to a doubling of CO_2 relative to the preindustrial level range from 2.1 to 4.7 K among models in phase 5 of the Coupled Model Intercomparison Project (CMIP5) (*Taylor et al.*, 2012; *Stocker et al.*, 2014). This is almost identical to the range produced by CMIP3 models (*Meehl et al.*, 2007; *Randall et al.*, 2007). This spread in climate sensitivity is mostly a result of the wide intermodel spread of simulated changes in the shortwave cloud radiative effect (SW CRE; defined as clear-sky minus all-sky top-of-atmosphere outgoing solar radiation) (*Webb et al.*, 2006; *Andrews et al.*, 2012b). Model disagreement on changes in marine boundary layer (MBL) clouds over eastern subtropical oceans was identified as the dominant driver of the spread of projections of SW CRE among CMIP3 models (*Bony and Dufresne*, 2005). In fact, neither CMIP3 nor CMIP5 models agree on whether subtropical MBL cloud fraction will increase or decrease under anthropogenic climate change (*Qu et al.*, 2013). An understanding of MBL clouds and their simulation in models is therefore important in order to evaluate climate change projections.

MBL clouds, including stratocumulus and shallow cumulus, are prevalent over eastern subtropical oceans. Stratocumulus clouds tend to occur under strongly descending air, a sharp temperature inversion, and within a shallow, well-mixed MBL (*Albrecht et al.*, 1995; *Norris*, 1998a; *Wood and Hartmann*, 2006). Shallow cumulus clouds tend to occur under more weakly descending air, a less sharp temperature inversion, and within a deeper, more decoupled MBL. Geographical and seasonal-to-decadal statistical relationships between MBL cloud fraction (CF) and the large-scale meteorology have been extensively examined in observations. These studies have found that large CF is favored by strong inversions (*Klein and Hartmann*, 1993; *Wood and Bretherton*, 2006; *Sun et al.*, 2011; *Myers and Norris*, 2013), cool sea surface temperature (*Hanson*, 1991; *Norris and Leovy*, 1994; *Clement et al.*, 2009), enhanced horizontal cold air advection near the surface (*Klein et al.*, 1995; *Park and Leovy*, 2004; *Norris and Iacobellis*, 2005), and weaker subsidence (*Myers and Norris*, 2013). The relationship between free-tropospheric moisture and MBL CF is not as clear from an observational perspective. *Klein et al.* (1995) found that enhanced free-tropospheric moisture over the eastern subtropical Pacific was associated with small low-level CF, whereas *Lacagnina and Selten* (2013) found that it was associated with large low-level CF.

These observed relationships can be understood in terms of their connections to the turbulent processes occurring within the MBL. Strong inversions may favor larger MBL CF by reducing entrainment dying and promoting a moister MBL in addition to being associated with cool sea surface temperature (*Bretherton and Wyant*, 1997; *Wood*, 2012). Cool sea surface temperature may favor larger CF by leading to a shallower, more well-mixed MBL containing predominantly stratocumulus by reducing surface latent heating (*Bretherton and Wyant*, 1997). Weaker subsidence leads to larger MBL CF by increasing cloud-top height and stratocumulus cloud thickness (*Blossey et al.*, 2013; *Bretherton et al.*, 2013; *Myers and Norris*, 2013). A moister free troposphere may act to reduce cloud-top radiative cooling (leading to a lowering of cloud top) and reduce entrainment drying (leading to a lowering of stratocumulus cloud base) (*Betts and Ridgway*, 1989).

This may result in either an increase or decrease in stratocumulus cloud thickness. The reduction of radiative cooling may also lead to decoupling, favoring cumulus and thinner stratocumulus, by reducing turbulent mixing (*Sandu et al.*, 2010).

The simulation of these observed relationships in climate models serves as a test for how well models represent MBL cloud processes. *Clement et al.* (2009) found that most CMIP3 models fail to simulate the interannual to decadal positive correlation between lower tropospheric stability and total CF over the eastern subtropical North Pacific. They also found that CMIP3 models exhibit a wide intermodel spread in the magnitude and the sign of the correlations between total CF and both sea surface temperature and pressure vertical velocity at 500 hPa. Similarly, *Caldwell et al.* (2013) found that most CMIP3 models fail to simulate the climatological positive correlation between estimated inversion strength and total CF. They also found negligible interannual relationships between total CF and both sea surface temperature and horizontal surface temperature advection in CMIP3 models. *Webb et al.* (2012) found that most models fail to simulate the observed climatological enhancement of SW CRE (i.e., more SW radiation reflected to space) associated with stronger lower tropospheric stability. These findings suggest considerable deficiencies in models' representation of MBL clouds.

One drawback of the aforementioned model evaluation studies is that total CF was examined rather than the vertical profile of CF. The relationships found in those studies therefore represent mixed effects of low-level and higher-level clouds. Indeed, *Broccoli and Klein* (2010) note that if low-level CF is examined in the GFDL CM2.1 model, the simulated relationships examined in *Clement et al.* (2009) are all of the correct sign. This motivates looking beyond the total CF metric in examining the simulation of clouds in climate models. It is also suggests that variability of higher-level CF over the eastern subtropics may be non-negligible in models and oppose variability of low-level CF, yielding confounding total CF changes.

Previous model evaluation studies generally have not compared the vertical profile of CF in models to satellite observations because satellites cannot, unlike a model, perfectly specify cloud fraction, liquid water content, and other cloud properties at each vertical level in the atmosphere. For example, passive satellites, such as those used for the International Satellite Cloud Climatology Project (ISCCP) (*Rossow and Schiffer*, 1999), can only detect low clouds unobstructed by higher clouds. Active satellites, such as the Cloud-Aerosol Lidar and Infrared Pathfinder Satellite Observations (CALIPSO) (*Chepfer et al.*, 2010), provide a more realistic vertical profile of cloud properties than passive satellites, but this type of observational data has only existed since 2006 compared to 1983 for passive satellite data. Still, both types of data represent retrieved cloud properties, not actual cloud properties. Contrastingly, within climate models and regardless of their realism, the values of various cloud properties are known exactly. Several CMIP5 models utilize "simulator" packages that provide cloud properties that an imaginary satellite orbiting the modeled world would detect (*Bodas-Salcedo et al.*, 2011). One such property is CF obtained using simulated retrieval methods similar to those of ISCCP and the CALIPSO-GCM Oriented CALIPSO Cloud Product (CALIPSO-GOCCP) (*Chepfer et al.*, 2010). Differences between observed CF and modeled CF using simulator packages can be mostly attributed to deficiencies in model physics rather than differences in the definition of CF.

Motivated by the shortcomings of previous studies, in this work we examine the interannual relationships of top-of-atmosphere SW, longwave (LW), and net CRE over eastern subtropical oceans to sea surface temperature, estimated inversion strength, horizontal surface temperature advection, free-tropospheric humidity, and subsidence in 11 CMIP3 models, 14 CMIP5 models, and observations. We complement this with an analysis of the relationship between the vertical profile of CF and the same meteorological variables. This will allow us to physically interpret the SW, LW, and net-CRE relationships in models and observations. Furthermore, assessment of CMIP5 CF derived from ISCCP and CALIPSO-GOCCP simulators will make possible an apples-to-apples comparison between models and observations.

3.1 Data and methods

3.1.1 Observational data

Tables 3.1 and 3.2 summarize the observational cloud and meteorological data used in this investigation, respectively. Each dataset was bilinearly interpolated onto a 2.5° × 2.5° equal-angle grid, which is the grid with the coarsest resolution of all datasets. SW, LW, or net CRE is defined as clear-sky minus all-sky top-of-atmosphere SW, LW, or net outgoing radiation (positive outward). According to this definition, clouds almost always exert a negative SW CRE and a positive LW CRE, acting to increase outgoing SW radiation (cooling effect) and decrease outgoing LW radiation (warming effect) at the top of the atmosphere, respectively. Therefore, hereafter, more negative (positive) SW CRE will be referred to as enhanced (weaker) SW CRE, and more positive (negative) LW CRE will be referred to as enhanced (weaker) LW CRE. The CRE data are provided by the Clouds and Earth's Radiant Energy System (CERES) Energy Balanced and Filled (EBAF) dataset version 2.7 (*Loeb et al.*, 2009).

We use CF from the GCM simulator-oriented ISCCP cloud product (*Pincus et al.*, 2012; *Zhang et al.*, 2012) and CALIPSO-GOCCP datasets. ISCCP provides CF in 7 pressure layers and 6 optical thickness categories. CALIPSO provides CF in 40 vertical layers specified in geometric height. We converted these height coordinates to pressure coordinates by assuming that pressure p decreases exponentially with height z such that $p = p_0 e^{-z/H}$, where surface pressure $p_0 = 1010$ hPa and scale height $H = 8000$ m. Total ISCCP CF for each pressure layer was computed by summing CF over all optical thickness categories. We use two versions of ISCCP cloud data: one that assumes clouds are not overlapped, which is what the ISCCP retrieval method assumes (satellite view), and one that assumes clouds are randomly overlapped. To estimate the true total CF at some level using the random overlap assumption, we divided the retrieved, unobstructed total CF by the clear-sky fraction above that level (*Rozendaal et al.*, 1995). The use of ISCCP CF data corrected for artifacts as in *Norris and Evan* (2015) yields no appreciable difference to our results.

We use meteorological variables from four atmospheric reanalyses, including the Climate Forecast System Reanalysis (CFSR) (*Saha et al.*, 2010), the Interim European Centre for Medium-Range Weather Forecasts (ECMWF) Re-Analysis (ERA-Interim) (*Dee et al.*, 2011), the Japanese 55-year Reanalysis Project (JRA-55) (*Ebita et al.*, 2011), and the Modern-Era Retrospective Analysis for Research and Applications (MERRA) (*Rienecker et al.*, 2011). Because meteorological observations over the oceans are sparse, using four reanalyses ensures that we robustly capture the range of observational uncertainty. The meteorological variables include sea surface temperature (SST), estimated inversion strength (EIS), advection by the surface wind over the SST gradient (SSTadv), specific humidity at 700hPa (q_{700}), and pressure vertical velocity at 700 hPa (ω_{700}). For JRA-55, air temperature two meters above the surface (T_{2m}) was used since SST was not provided.

EIS was calculated as in *Wood and Hartmann* (2006), who derived the formulation

$$\mathrm{EIS} = \mathrm{LTS} - \Gamma_m^{850}(z_{700} - \mathrm{LCL}). \tag{3.1}$$

Here, LTS stands for lower tropospheric stability and is the difference in potential temperature between the 700-hPa level and the surface, Γ_m^{850} is the moist adiabatic lapse rate at 850hPa, z_{700} is the height of the 700-hPa level relative to the surface, and LCL is the height of the lifting condensation level relative to the surface. We assume a surface relative humidity of 80% as in *Wood and Hartmann* (2006) and use the method of *Georgakakos and Bras* (1984) for the calculation of LCL. We computed SSTadv as the advection by reanalysis near-surface wind over the SST gradient (or T_{2m} gradient for JRA-55) using a centered finite differencing scheme in spherical coordinates.

3.1.2 Model output

We use monthly output from 25 coupled climate models from 10 different modeling centers participating in both CMIP3 and CMIP5, summarized in Table 3.3. This will allow us to assess the overall progress, if any, in modeling of subtropical cloud processes from CMIP3 to CMIP5. For a particular modeling center, each of the model variants examined incorporates a different atmospheric model.

For the CMIP3 models, we use output from the climate of the twentieth-century experiment runs, and the “run1” ensemble member is used for each model. For the CMIP5 models, we use output from the historical runs, and the “r1i1p1” ensemble member is used for each model. These scenarios use anthropogenic and natural forcing constituents, and run from the late 1800s until 1999 for CMIP3 and until 2005 for CMIP5. So that the time periods examined are the same length as the ISCCP record (26 yr), time periods of 1974-99 and 1980-2005 were used for CMIP3 and CMIP5 data, respectively. The results of our study, however, are insensitive to the chosen time period.

The model variables used are the same as the observed variables, with the exception of CF. We use the vertical profile of CF of each model in our analysis, but these profiles cannot be directly compared to those of ISCCP or CALIPSO-GOCCP due to the imperfect retrievals of cloud properties by satellites and inconsistent definitions of CF between models and the satellite datasets. Nonetheless, qualitative analysis of these profiles will provide insight into the relationships between CRE and the meteorology. ISCCP and CALIPSO-GOCCP simulator-derived CF will be examined from the six CMIP5 models providing such data (indicated in Table 3.3).

3.1.3 Computation of cloud relationships to meteorological variables

Because we are primarily interested in MBL clouds, we chose to define our domain dynamically, rather than spatially, as in *Bony et al.* (2004). The domain includes all ocean grid boxes within $30°\mathrm{S} - 30°\mathrm{N}$ that have long-term mean $\omega_{700} > 0$ for every calendar month and monthly-mean $\omega_{700} > 0$ for at least 80% of the time record; only months for which $\omega_{700} > 0$ were examined. This method allows us to focus on dynamically similar regimes predominantly containing MBL clouds. It also implies that positive (negative) anomalies of ω_{700} represent strong (weak) subsidence relative to the mean. Since the models have different subsidence climatologies, each domain is specific to each reanalysis and model. The percentage of ocean grid boxes within $30°\mathrm{S} - 30°\mathrm{N}$ satisfying our criteria are shown in Tables

3.2 and 3.3 for reanalyses and models, respectively.

Before examining relationships between the cloud and meteorological variables, we computed linearly detrended interannual monthly anomalies for each grid box. By detrending, we avoided the possibility of our results being affected by potential unphysical, low-frequency artifacts in the satellite cloud observations and reanalyses. We calculated relationships of CRE or CF to a meteorological property x by splitting values of x from all grid boxes into two subsets, one with anomalies above the median x and one with anomalies below the median. This is nearly identical to separating values of x according to positive and negative anomalies. We then took the difference in mean CRE or CF between these two subsets and divided by the difference in mean x for each subset. This is essentially a centered finite-differencing scheme for estimating the slope. We refer to the resulting quantity as the relationship of CRE or CF to x, which we write mathematically as $D(\mathrm{CRE})/D(x)$ or $D(\mathrm{CF})/D(x)$. Although not shown in the paper, slopes were also computed using linear regression, and the results are quantitatively similar. It is important to note that the computed relationships are not necessarily independent because the predictor variables may covary. They can therefore be thought of as total derivatives. This is in contrast to *Myers and Norris* (2013), who examined the independent effects of subsidence and inversion strength on subtropical MBL clouds (i.e., partial derivatives).

Each relationship is normalized by the 1984-2012 standard deviation of observed interannual anomalies of each meteorological variable x. This allows us to more easily compare the magnitudes of each relationship, which can be viewed as the response of CRE or CF to a typical anomaly in x. Because there are four reanalyses, there are four standard deviations for each x. We use the average of these four standard deviations of each x to normalize each observed and modeled quantity. Since observed and modeled values of a given relationship are normalized by a single standard deviation, relative differences among values and their statistical significance are unchanged compared to nonnormalized values.

A two-tailed t test for the difference between two sample means provided an assessment of the statistical significance of individual relationships and the difference between modeled and observed relationships. The range of observational uncertainty of a CRE relationship is defined as the envelope of 95% confidence intervals of the four observed values (one derived from each reanalysis), and statistical significance of the observations is gauged by this range of uncertainty. A modeled CRE relationship is considered to be outside the range of observational uncertainty if it is more positive or more negative than each of the four observational estimates with 95% confidence. We also assess whether models simulate the correct sign of each CRE relationship. A model is considered to simulate an incorrect sign if 1) it simulates a statistically significant CRE relationship of opposite sign to the observed relationship, 2) it simulates a statistically significant CRE relationship when the observed relationship is statistically insignificant, or 3) it simulates a statistically insignificant CRE relationship when the observed relationship is statistically significant. If none of these conditions occurs, the model is considered to simulate the correct sign of the CRE relationship.

The cloud data are autocorrelated because processes affecting clouds on monthly time scales have a large spatial scale. To take this into account in statistical significance tests, for each observational cloud variable we computed the ratio of the number of statistically independent points [effective number (n_{eff})] to the nominal number of points n by determining the lag at which the zonal, meridional, or temporal autocorrelation coefficients cross zero. The inverse of this lag is assumed to be equal to this ratio. Zonal and meridional anomalies of each latitude and longitude band, respectively, were used to compute zonal and meridional autocorrelation. The temporal ratio multiplied by the zonal and meridional ratios is assumed to be equal to the overall ratio of effective to nominal number of points. Table 3.1 shows the ratios for observed cloud variables. We assume that the modeled ratios are equal to the observed ratios multiplied by $(i \times j)/(2.5^\circ \times 2.5^\circ)$, where i (j) is the average latitude (longitude) increment of each model's grid. This ensures that the total number of effective points in models with resolutions higher (lower) than $2.5^\circ \times 2.5^\circ$ is not overestimated (underestimated).

3.2 Results

3.2.1 Observed climatology

Figure 3.1 shows observed mean annual fields of SW and LW CRE, SST and surface wind velocity, EIS, SSTadv, q_{700}, and ω_{700}. Over the eastern subtropical oceans, SW CRE (Fig. 3.1a) is strongly negative due to high amounts of reflection of shortwave radiation by abundant, optically thick low-level clouds. LW CRE (Fig. 3.1b) is weakly positive due to approximately equal amounts of absorption of longwave radiation by these low-level clouds and by less abundant, optically thin high-level clouds. Inspection of the meteorology reveals that regions of enhanced SW CRE and weaker LW CRE are characterized by cool SST (Fig. 3.1c), strong EIS (Fig. 3.1d), cold SSTadv (Fig. 3.1e), low q_{700} (Fig. 3.1f), and strong ω_{700} (Fig. 3.1g). This is qualitatively consistent with previous observational studies that have found large CF of low-level, optically thick clouds and small CF of overlying high-level, optically thin clouds associated with these meteorological conditions (*Hanson*, 1991; *Klein and Hartmann*, 1993; *Klein et al.*, 1995; *Wood*, 2012; *Christensen et al.*, 2013).

3.2.2 Observed and multimodel mean CRE and CF interannual relationships

One might expect these geographical relationships to also occur on interannual time scales, and this is generally confirmed in Fig. 3.2, which shows interannual relationships of SW, LW, and net CRE to the meteorological variables for both observations and multimodel means. Since subtropical optically thick, low-level (around 700 hPa and lower in elevation) clouds dominate SW CRE and subtropical optically thin, high-level (around 400 hPa and higher in elevation) clouds contribute substantially to LW CRE, Fig. 3.3 complements the results of Fig. 3.2 by showing vertical profiles of the observed and multimodel mean CF relationships. Because strongly negative SW CRE is a primary climatological feature over the eastern subtropical oceans, in our discussion we speak in terms of which observed meteorological conditions are associated with anomalously enhanced SW CRE.

CRE AND CF RELATIONSHIPS TO SST, EIS, AND SSTadv

Observations show that anomalously cool SST, strong EIS, and cool SSTadv are each associated with enhanced SW CRE (Fig. 3.2a), a small decrease or no change in LW CRE (Fig. 3.2b), and more negative net CRE (i.e., more outgoing net radiation at the top of the atmosphere, Fig. 3.2c). This is physically consistent with the observed increase in low-level CF and small decrease or almost no change in high-level CF for the same meteorological conditions (Figs. 3.3a–c) and is consistent with previous observational studies (*Hanson*, 1991; *Klein and Hartmann*, 1993; *Klein et al.*, 1995). The above interpretation is corroborated by composite plots of the ISCCP CF relationships binned according to cloud-top pressure and optical thickness, multiplied by identically binned cloud radiative kernels (Figs. A3.1–A3.3; see the appendix for discussion of kernels). It is important to recognize that SST and EIS are anticorrelated ($r = 0.6$ over all grid boxes for the detrended interannual monthly anomalies), so that the observed and modeled CRE and CF relationships to these variables are qualitatively similar but with opposite signs. We also note that the maximum magnitude of each of the observed low-level CF relationships occurs at a higher elevation for ISCCP than for CALIPSO, likely because of the well-known problem of ISCCP mistaking low-level clouds for midlevel clouds when there are strong inversions (*Garay et al.*, 2008) or overlying cirrus (*Mace et al.*, 2006). We consider the elevation where CALIPSO places the maximum magnitude of the relationships to be more representative of reality.

In agreement with observations, the CMIP3 and CMIP5 multimodel means simulate enhanced SW CRE and larger low-level CF for anomalously cool SST and strong EIS, but the magnitude of each relationship is slightly weaker than observed. This is consistent with *Bony and Dufresne* (2005), who found that CMIP3 models tend to underestimate the enhancement of SW CRE associated with cooler SST in the tropical ocean subsidence regime. In contrast to observations, the multimodel means simulate no change in SW CRE when SSTadv is anomalously cold, physically consistent with producing too little increase in low-level CF for this condition. This indicates that the SW-CRE-SSTadv relationship is on average poorly simulated by the models. There is a substantial increase in intermodel spread of $D(\mathrm{SW})/D(\mathrm{SST})$ and $D(\mathrm{SW})/D(\mathrm{EIS})$ among CMIP5 models compared to CMIP3, physically consistent with the increase in intermodel spread of $D(\mathrm{CF})/D(\mathrm{SST})$ and $D(\mathrm{CF})/D(\mathrm{EIS})$ for low–level clouds evident in Figs. 3a and 3b. In fact, a two-tailed F test for two sample variances indicates that the CMIP5 intermodel standard deviations of $D(\mathrm{SW})/D(\mathrm{SST})$ and $D(\mathrm{SW})/D(\mathrm{EIS})$ are significantly greater than those of CMIP3 with 95% confidence. Since the multimodel means of these two relationships are well simulated for both generations of models, this suggests on average worse performance by the CMIP5 models.

Both the CMIP3 and CMIP5 multimodel means also simulate weaker LW CRE and decreased high-level CF when EIS is anomalously strong, in agreement with observations. However, the CMIP5 ensemble mean relationships are closer to observations, and the CMIP5 intermodel standard deviation of $D(\mathrm{LW})/D(\mathrm{EIS})$ is significantly less than that of CMIP3 with 90% confidence. This is probably because the intermodel spread of $D(\mathrm{CF})/D(\mathrm{EIS})$ for high-level clouds is smaller among CMIP5 models than among CMIP3 models. The CMIP3 and CMIP5 ensemble means exhibit statistically significant weaker LW CRE for anomalously cool SST and cold SSTadv, while the observed values do not. Composite plots of binned LW-CRE relationships to SST and SSTadv (as in Fig. A3.2) of models employing the ISCCP simulator suggest that this can be explained by models' simulating too little increase in optically thick, low-level CF for cooler SST and colder SSTadv (results not shown). This allows the overall weaker LW CRE associated with these meteorological conditions to be dominated by reduced absorption of LW radiation due to a decrease in optically thin, high-level CF. In observations, this reduced absorption is equally offset by greater absorption of LW radiation due to a relatively large increase in low-level CF (Fig. A3.2).

An important feature of Fig. 3.2 is that, for both CMIP3 and CMIP5, the intermodel spread of each of the SW-CRE relationships to SST, EIS, and SSTadv is much larger than that of the LW-CRE relationships. This is physically consistent with the greater intermodel spread of $D(\mathrm{CF})/D(\mathrm{SST})$ and $D(\mathrm{CF})/D(\mathrm{EIS})$ for low-level clouds than for high-level clouds in the case of CMIP5.

Finally, the multimodel means produce net-CRE relationships to SST, EIS, and SSTadv that are generally similar to the respective SW-CRE relationships. However, for $D(\mathrm{net})/D(\mathrm{SST})$ and $D(\mathrm{net})/D(\mathrm{SSTadv})$, there is some degree of compensating errors by the SW and LW components. This yields changes in net CRE that are artificially closer to the observations relative to the changes in SW CRE for anomalies in SST and SSTadv.

CRE AND CF RELATIONSHIPS TO q_{700} AND ω_{700}

In observations, anomalously high q_{700} and weak ω_{700} are each associated with enhanced SW CRE (Fig. 3.2a) and an approximately equal enhancement of LW CRE (i.e., less LW radiation emitted to space; Fig. 3.2b), yielding no change in net CRE (Fig. 3.2c). The increase in mid- and high-level CF associated with these meteorological conditions is physically consistent with the enhancement of both SW and LW CRE and is sufficient to offset the radiative effects of the decrease in low-level CF also seen in the profiles (Figs. 3d,e; see also Figs. A3.1–A3.3). The decrease in low-level CF for weaker ω_{700} evident in the CALIPSO profile may seem to contradict the finding of *Myers and Norris* (2013) that weaker ω_{700}, independent of variations in EIS, increases low-level CF. But the present study does not attempt to remove possible confounding factors affecting the low-level CF–ω_{700} relationship. The results of the two studies may therefore not be comparable. It is important to recognize that ω_{700} and q_{700} are anticorrelated ($r = 0.3$), so that the observed and modeled CRE and CF relationships to these variables are qualitatively similar but with opposite signs. Examination of the vertical profile of q_{700} (not shown) indicates that when q_{700} increases, so does q throughout the troposphere. Higher q_{700} and weaker ω_{700} may favor more mid- and high-level clouds by increasing relative humidity. Anomalously high q_{700} is also associated with a decrease in CF in the 850–700-hPa layer, and an increase in CF just below and above that layer (Fig. 3.3d). This peculiar vertical structure may explain why previous observational studies have found differing effects of free-tropospheric moisture on low-level clouds over the subtropical oceans (*Klein et al.*, 1995; *Lacagnina and Selten*, 2013).

In agreement with observations, the CMIP3 and CMIP5 multimodel means simulate enhanced SW CRE and enhanced LW CRE for relatively high q_{700} and weak ω_{700}. This is physically consistent with the simulated vertical profiles of $D(\mathrm{CF})/D(q_{700})$ and $D(\mathrm{CF})/D(\omega_{700})$, which qualitatively resemble the observed profiles. The offsetting changes in low-level CF when q_{700} is anomalously high, however, are considerably smaller than observed. As in observations, the ensemble mean $D(\mathrm{net})/D(q_{700})$ is nearly indistinguishable from zero for both CMIP3 and CMIP5. Unlike in observations, though, each ensemble mean simulates more negative net CRE for anomalously weak ω_{700}, and the relationship is statistically significant. This is because models on average overestimate the magnitude of the SW-CRE relationship more strongly than they overestimate the magnitude of the LW-CRE relationship. One reason for this may be that the ensemble means do not simulate a decrease in low-level CF at around 900 hPa for relatively weak ω_{700}, a feature evident in the CALIPSO profile that partially offsets the enhancement of SW CRE associated with higher-level CF. Like the relationships discussed in the previous section, the intermodel spread of each of the SW-CRE relationships to q_{700} and ω_{700} is much larger than that of the LW-CRE relationships.

3.2.3 Individual model CRE relationships

In addition to the multimodel means, we also examine CRE relationships to the meteorological variables in individual models. Figure 3.4 shows the CRE relationships to SST, EIS, and SSTadv for observations, individual CMIP3 and CMIP5 models, and multimodel means for completeness. Figure 3.5 shows the CRE relationships to q_{700} and ω_{700}. A sizeable number of models (more than half in several cases) simulate SW and net-CRE relationships outside the range of observational uncertainty. For several relationships, this is true for a majority of models even when the multimodel mean is not outside the range of observational uncertainty. In addition, some models do not even predict the correct signs of the SW and net-CRE relationships. A relatively small number of models simulate the

LW-CRE relationships outside the range of observational uncertainty. Generally, when the intermodel spread of a relationship is large relative to the observational uncertainty (Fig. 3.2), a high percentage of models simulate the relationship outside this range of uncertainty of observations, and vice versa.

Examining Fig. 3.4 in more detail, CMIP3 models generally simulate the correct sign and magnitude of the SW and net-CRE relationships to SST and EIS, whereas CMIP5 models do not. Strikingly, half of CMIP5 models simulate the wrong sign of the SW-CRE relationship to EIS, whereas only two CMIP3 models do so. Moreover, in contrast to observations, most CMIP3 and CMIP5 models simulate a negligible relationship or weaker SW CRE for anomalously cold SSTadv, consistent with the bias of the multimodel means (Fig. 3.2a). Third, most CMIP3 and CMIP5 models exhibit weaker LW CRE for anomalously cool SST or cold SSTadv, whereas observations show no change in LW CRE for either of these meteorological conditions. This is consistent with the bias of the multimodel means (Fig. 3.2b). Last, Fig. 3.5 reveals that most models simulate a statistically significant change in net CRE for variations in both q_{700} and ω_{700} despite observations showing no change in net CRE for the same variations. In the case of $D(\text{net})/D(\omega_{700})$, this is consistent with the bias of the multimodel means (Fig. 3.2c).

3.2.4 Connection between CF and SW-CRE relationships in CMIP5 models

We next assess the physical connection between the sign of individual SW-CRE relationships and the vertical profile of the CF relationships in CMIP5 models. CMIP3 models are not examined because they do not provide vertical profiles of CF derived from the ISCCP and CALIPSO simulators.

In Figs. 3.6a–c we show the CMIP5 simulated vertical profiles of $D(\text{CF})/D(\text{SST})$, $D(\text{CF})/D(\text{EIS})$, and $D(\text{CF})/D(\text{SSTadv})$ of models that simulate the correct sign of the respective SW-CRE relationships. Observed profiles are also shown. The CF relationships to q_{700} and ω_{700} are not shown since, as previously noted, the SW-CRE relationships to these variables represent varying effects of changes in low-, mid-, and high-level CF (Figs. 3.2 and 3.3) and are thus more complicated to interpret. All of these CMIP5 models simulate an increase in low-level CF for anomalously cool SST, strong EIS, and cold SSTadv. Thus they simulate enhanced SW CRE for the appropriate physical reason.

Shown in Figs. 3.6d–f are the CMIP5 simulated vertical profiles of $D(\mathrm{CF})/D(\mathrm{SST})$, $D(\mathrm{CF})/D(\mathrm{EIS})$, and $D(\mathrm{CF})/D(\mathrm{SSTadv})$ of models that simulate the wrong sign of the respective SW-CRE relationships. Some of these models simulate no change or an unrealistic decrease in low-level CF when SST is cooler, EIS is stronger, and SSTadv is colder. This explains why these models simulate no change or unrealistically weaker SW CRE for these meteorological conditions. Some models, however, appear to simulate the correct sign of the low-level CF relationships despite simulating the wrong sign of the SW-CRE relationships. One such model is FGOALS-g2. When SST is cooler, EIS is stronger, and SSTadv is colder, this model simulates an unrealistically large decrease in CF above roughly 800 hPa in elevation that offsets the enhancement of SW CRE associated with an increase in CF at a lower elevation. Another model that exhibits similar behavior is GFDL-CM3. This model produces the correct sign of the low-level CF relationship to SSTadv despite simulating the wrong sign of the SW-CRE relationship to SSTadv. When SSTadv is anomalously cold, GFDL-CM3 simulates an unrealistically large decrease in CF in the middle-to-upper troposphere that offsets the enhancement of SW CRE associated with an increase in CF near the surface. These examples show that for models to realistically simulate the relationship between SW CRE and the meteorology in regions of climatological subsidence, they must not only accurately simulate the low-level CF relationships; they must accurately simulate the mid- and high-level CF relationships as well.

In yet another case, CCSM4 simulates the correct sign of the low-level CF relationships to EIS and SSTadv despite simulating the wrong sign of the corresponding SW-CRE relationships. While most models simulate a maximum in mean annual cloud water content (CWC) between 700 and 900 hPa, CCSM4 simulates a local minimum in CWC at around 900 hPa and a local maximum in CWC at around 500 hPa (Fig. A3.4). Therefore, the simulated decrease in CF above roughly 700 hPa associated with anomalously strong EIS and cold SSTadv, though small, leads to substantially weaker SW CRE because the clouds are optically thick. In turn this more than offsets the enhancement of SW CRE associated with an increase in CF below 700hPa where the clouds are optically thin. This shows that for models to realistically simulate the relationships between SW CRE and the meteorology, they must not only accurately simulate the low-level CF relationships; they must reasonably simulate the mean state of cloud optical thickness as well.

For those models for which ISCCP simulator-derived CF was available, vertical profiles of the CF relationships are additionally examined as a more direct comparison with the observations. Among these models, Fig. 3.7 shows the simulated vertical profiles of $D(\mathrm{CF})/D(\mathrm{SST})$, $D(\mathrm{CF})/D(\mathrm{EIS})$, and $D(\mathrm{CF})/D(\mathrm{SSTadv})$ of models that simulate the correct and incorrect signs of the respective SW-CRE relationships. Observed ISCCP profiles are also shown for reference. In all of these models, the low-level CF relationships are sufficient to explain the signs of the respective SW-CRE relationships. This is corroborated by the observed and modeled vertical profiles of the same ISCCP CF relationships multiplied by the SW cloud radiative kernel profile (Fig. A3.5). We also note that for these six models, the intermodel spread of each of the low-level CF relationships is larger than that of the corresponding high-level CF relationships, explaining why the intermodel spread of the SW-CRE relationships is larger than that of the LW-CRE relationships. Although not shown, Fig. 3.7 was replicated using CALIPSO simulator-derived CF, and the results are qualitatively similar.

Before continuing, we note that changes in cloud optical depth are also found to influence the response of SW CRE to variations in the meteorology (Fig. A3.6) in models and observations. However, changes in total cloud amount are sufficient to explain the sign of each of the SW-CRE–meteorology relationships and explain more of the intermodel spread of the SW-CRE–meteorology relationships compared to changes in optical depth. This justifies our focus on CF in the present study.

3.2.5 Model performance and climate change

Is there a relationship between models' simulation of subtropical MBL cloud-meteorology relationships and their projections of anthropogenic climate change? To address this question, we compare SW-CRE changes and equilibrium climate sensitivity (ECS) estimates to models' root-mean-square error (RMSE) of all five $D(\mathrm{SW})/D(x)$ values relative to the observed values. Mathematically, the RMSE is expressed as

$$\mathrm{RMSE} = \sqrt{\frac{1}{5}\sum_{i=1}^{5}\Big(\frac{D(\mathrm{SW})}{D(x_i)}^{\mathrm{model}} - \frac{D(\mathrm{SW})}{D(x_i)}^{\mathrm{obs}}\Big)^2}, \tag{3.2}$$

where $D(\mathrm{SW})/D(x_i)^{\mathrm{model}}$ is one of the five simulated relationships for a given model, and $D(\mathrm{SW})/D(x_i)^{\mathrm{obs}}$ is the mean value of the observed relationship over all reanalyses. Twenty-first-century changes in SW CRE (2080–99 minus 2000–19 mean annual SW CRE averaged over the five main low-level cloud regions over the eastern subtropical oceans) are taken from *Qu et al.* (2013). The simulations examined include the A1B (*Nakicenovic and Swart*, 2000) forcing scenario for the CMIP3 models and the representative concentration pathway (RCP) 8.5 (*Taylor et al.*, 2012) for the CMIP5 models. ECS is defined as the equilibrium global mean surface temperature change due to a doubling of CO2, and CMIP3 and CMIP5 values are taken from *Randall et al.* (2007) and *Stocker et al.* (2014), respectively. We note that SW-CRE changes are positively correlated with ECS ($r = 0.92$ for CMIP3 and $r = 0.6$ for CMIP5; Fig. 3.8a).

Figures 3.8b and 3.8c show the RMSE of the SW-CRE relationships plotted against twenty-first-century SW-CRE trends and ECS values for all available models. The plots show that models that simulate large RMSE (unrealistic models) tend to exhibit more negative SW-CRE changes and low ECS compared to models with smaller RMSE (more realistic models). In fact, of the CMIP5 models shown in Fig. 3.8b, the two with the largest RMSE are the only models simulating enhanced SW CRE. To quantify these inferences, we divide models into two subsets according to whether their RMSE values are less than or greater than the median RMSE (vertically dashed lines in Figs. 3.8b and 3.8c). We show the mean SW-CRE change and ECS of each subset in Table 3.4. For both CMIP3 and CMIP5, models with RMSE less than the median RMSE have a higher mean ECS and more positive mean SW-CRE change compared to models with RMSE greater than the median, although the difference between the means is statistically significant ($p < 0.1$) in only two cases. Figures 3.8b and 3.8c also show that the intermodel spread of twenty-first-century SW-CRE changes and ECS is generally higher among the more realistic models compared to the less realistic models. Collectively, these results suggest that a positive SW cloud feedback associated with subtropical MBL clouds and a high ECS is more likely than a negative cloud feedback and a low ECS. It is clear, however, that accurate simulation of SW-CRE–meteorology relationships is not sufficient to constrain either the SW-CRE feedback or ECS in a statistically robust manner. One reason for this may be that the climate change scenarios examined here include changes in aerosols, which can cause changes in cloudiness independent of the meteorology.

3.3 Conclusions

We have evaluated the performance of CMIP3 and CMIP5 models in simulating the interannual relationships of shortwave, longwave, and net cloud radiative effect to sea surface temperature, estimated inversion strength, horizontal surface temperature advection, free-tropospheric moisture, and subsidence. To ensure dynamically consistent domains among models and observations, we examined grid boxes occurring within the tropical (30°S – 30°N) oceanic subsidence regime for each particular model and reanalysis. Examining the relationships of the vertical profile of cloud fraction to the same meteorological variables allowed us to physically assess the connection between changes in cloud radiative effect and changes in cloud fraction.

We find that, in observations, anomalously cool SST, strong EIS, and cold SSTadv are each associated with larger low-level CF and enhanced SW CRE (i.e., more shortwave radiation reflected to space). Higher q_{700} and weaker ω_{700} are each associated with larger mid- and high-level CF and enhanced SW CRE, enhanced LW CRE (i.e., less LW emitted radiation to space), and no change in net CRE. Changes in LW CRE associated with variability of q_{700} and ω_{700} can thus be as large as changes in SW CRE over the eastern subtropical oceans, even though climatologically the magnitude of SW CRE is much stronger than that of LW CRE. Both the CMIP3 and CMIP5 multimodel means generally simulate the above relationships realistically. Moreover, the intermodel spread of the SW-CRE relationships is larger than that of the LW-CRE relationships. Since previous findings that trends in SW CRE, not LW CRE, are responsible for the wide spread of cloud feedbacks simulated in CMIP3 and CMIP5 models (*Webb et al.*, 2006; *Andrews et al.*, 2012a), this suggests that interannual estimates of CREmeteorology relationships may project onto the longer time scale of anthropogenic climate change.

A larger percentage of CMIP5 than CMIP3 models are found to simulate the wrong sign or magnitude of the relationship of SW CRE to SST and EIS. In fact, half of CMIP5 models simulate the wrong sign of the SW-CRE relationship to EIS. To the extent that EIS strengthens over the eastern subtropical oceans in simulations of anthropogenic climate change (*Webb et al.*, 2012), this suggests that for this change a substantial percent- age of CMIP5 models simulate the wrong sign of the SW cloud feedback to warming. Furthermore, most CMIP3 and CMIP5 models exhibit the wrong sign of the SW- CRE relationship to SSTadv. Insofar as cold SSTadv will amplify over the eastern subtropical oceans due to anthropogenic climate change (*Caldwell et al.*, 2013), this suggests that for this change most models fail to simulate the implied negative SW cloud feedback to warming.

We find that for CMIP5 models to realistically produce SW-CRE relationships to SST, EIS, and SSTadv, it is necessary but not sufficient for models to realistically simulate corresponding low-level CF relationships. To produce these observed SW-CRE– meteorology relationships, models must also reasonably simulate the mid and high-level CF relationships and the mean cloud water content. While changes in low-level CF explain much of the CMIP5 intermodel spread in the simulated SW-CRE relationships, some of the spread is explained by changes in mid and high- level CF and differences in the mean cloud water content. Studies that examine the intermodel spread of changes in SW CRE in regions of climatological subsidence (*Bony and Dufresne*, 2005) should therefore use caution in attributing those changes exclusively to low-level clouds.

Comparing overall model performance of the SW-CRE–meteorology relationships to twenty-first-century trends in SW CRE and equilibrium climate sensitivity suggests that the more realistic models simulate more positive SW-CRE changes and higher climate sensitivities compared to the less realistic models. This is consistent with recent studies that have found that climate models most closely resembling observations simulate strong positive cloud feedbacks and enhanced global warming (*Fasullo and Trenberth*, 2012; *Klein et al.*, 2013; *Sherwood et al.*, 2014; *Su et al.*, 2014). Despite this, there is not a one- to-one relationship between the root-mean-square error of the modeled $D(\mathrm{SW})/D(x)$ values and either SW-CRE trends or climate sensitivity. A thorough assessment of projections of the meteorological and cloud changes in a future study is necessary in order to understand why this is the case.

Acknowledgments

This study was funded by NSF award AGS-0946094 and NASA Earth and Space Science graduate fellowship 13-EARTH13R-0006. CERES data were obtained from the NASA Langley Research Center CERES ordering tool at “http://ceres.larc.nasa.gov/”. The CFSR and JRA-55 data were provided by the Data Support Section of the Computational and Information Systems Laboratory at the National Center for Atmospheric Research. NCAR is sponsored by the National Science Foundation. ERA-Interim data were downloaded from the ECMWF data server at “http://apps.ecmwf.int/datasets/”. The Global Modeling and Assimilation Office and the Goddard Earth Sciences Data and Information Services Center provided the MERRA data. The authors thank both the World Climate Research Programme’s Working Group on Coupled Modeling, which is responsible for CMIP, as well as the climate modeling groups for producing and making available their model output. Thanks to Mark Zelinka, who provided the cloud radiative kernel data, and Xin Qu, who provided values of the twenty-first-century SW-CRE trends projected by the models. Lastly, the authors thank three anonymous reviewers for their valuable comments. This chapter is published in its entirety in **Myers, T.A., and Norris, J.R., "On the relationships between subtropical clouds and meteorology in observations and CMIP3 and CMIP5 models", *J. Climate*, 28(8), 2015**. The dissertation author was the primary investigator and author of the paper.

Tables and Figures

Table 3.1: Summary of satellite data used in the investigation. The values in the n_{eff}/n column are the ratio of the number of statistically independent points to the nominal number of points for the different cloud variables, computed as described in the text.

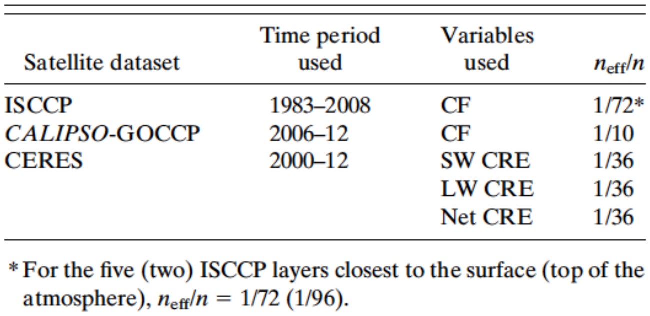

Satellite dataset	Time period used	Variables used	n_{eff}/n
ISCCP	1983–2008	CF	1/72*
CALIPSO-GOCCP	2006–12	CF	1/10
CERES	2000–12	SW CRE	1/36
		LW CRE	1/36
		Net CRE	1/36

* For the five (two) ISCCP layers closest to the surface (top of the atmosphere), n_{eff}/n = 1/72 (1/96).

Table 3.2: Summary of reanalysis data used in the investigation. Values in the $\omega_{700} > 0$ column are the percentage of ocean grid boxes within 30°S – 30°N satisfying the criteria specified in the text for the different reanalyses.

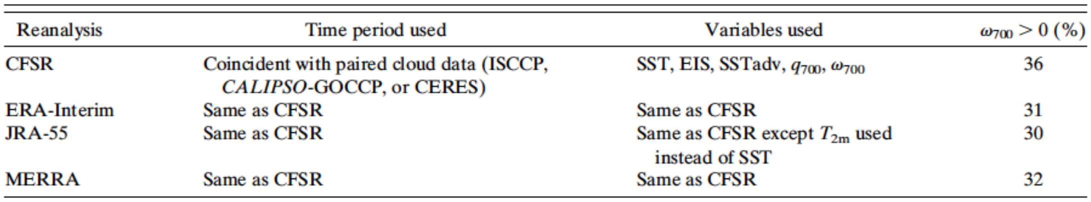

Reanalysis	Time period used	Variables used	$\omega_{700} > 0$ (%)
CFSR	Coincident with paired cloud data (ISCCP, *CALIPSO*-GOCCP, or CERES)	SST, EIS, SSTadv, q_{700}, ω_{700}	36
ERA-Interim	Same as CFSR	Same as CFSR	31
JRA-55	Same as CFSR	Same as CFSR except T_{2m} used instead of SST	30
MERRA	Same as CFSR	Same as CFSR	32

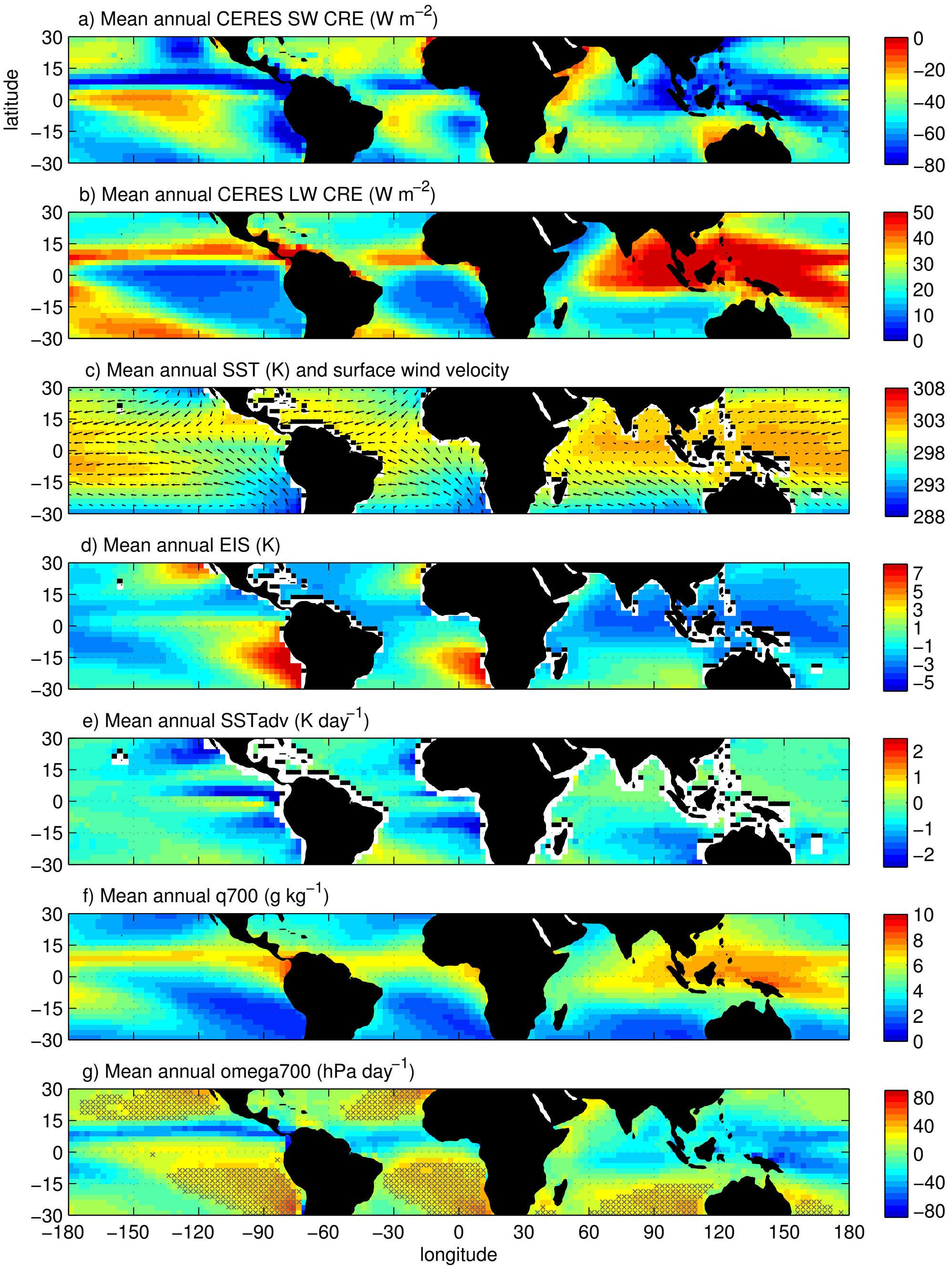

Figure 3.1: Mean annual: (a),(b) 2000–12 CERES shortwave and longwave cloud radiative effect, respectively, (c) 1984–2012 ERA-Interim sea surface temperature and surface wind velocity, (d) estimated inversion strength, (e) horizontal surface temperature advection, (f) specific humidity at 700 hPa, and (g) pressure vertical velocity at 700 hPa with the × symbol indicating grid boxes used in the ERA-Interim observational analysis.

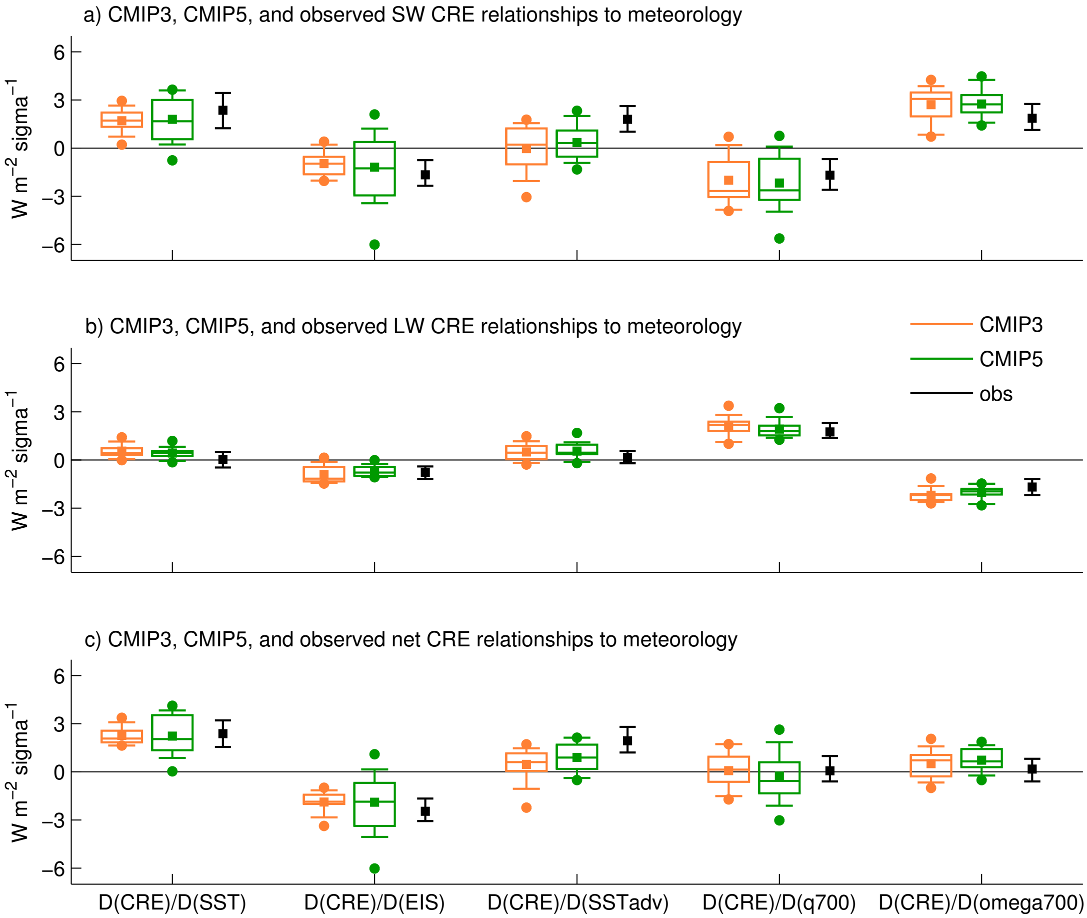

Figure 3.2: (a) Shortwave cloud radiative effect relationship to meteorological variables in CMIP3 models (orange box plots), CMIP5 models (green box plots), and observations (black squares and error bars); (b) as in (a), but for longwave cloud radiative effect; (c) as in (a), but for net cloud radiative effect. For each modeled relationship, the square denotes the multimodel mean, the horizontal line denotes the median of all modeled values, the box spans the interquartile range of all modeled values, the whiskers extend to the 10th and 90th percentiles of all modeled values, and the two circles are the modeled values outside the 10th and 90th percentiles. For each observed relationship, the error bars span the four 95% confidence intervals derived from CERES and the four reanalyses, and the square is the mean of the four reanalysis values.

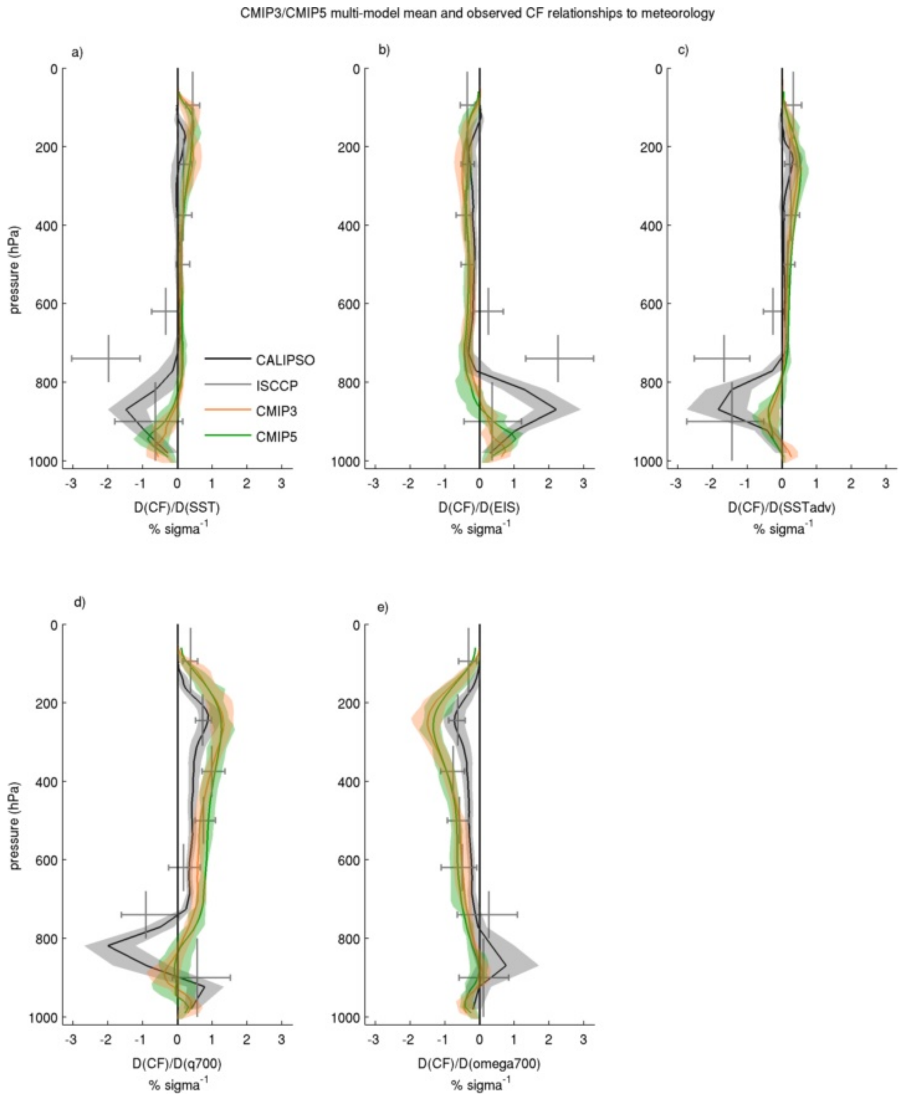

Figure 3.3: Cloud fraction relationship to (a) sea surface temperature, (b) estimated inversion strength, (c) horizontal surface temperature advection, (d) specific humidity at 700 hPa, and (e) pressure vertical velocity at 700 hPa as a function of pressure in CMIP3 models (orange lines and shading), CMIP5 models (green lines and shading), ISCCP (gray lines), and CALIPSO (black lines and gray shading). For each modeled relationship, the multimodel mean is plotted as a line, and the shading spans the interquartile range among all modeled values. For ISCCP, the horizontal error bars span the eight 95% confidence intervals derived from the four reanalyses and either the “random overlap” or “satellite view” version of ISCCP. Each vertical line spans one of the seven ISCCP cloud-top pressure categories and represents the mean among all reanalyses and both versions of ISCCP. For CALIPSO, the shading spans the four 95% confidence intervals derived from the four reanalyses, and the black line is the mean of the four reanalyses values.

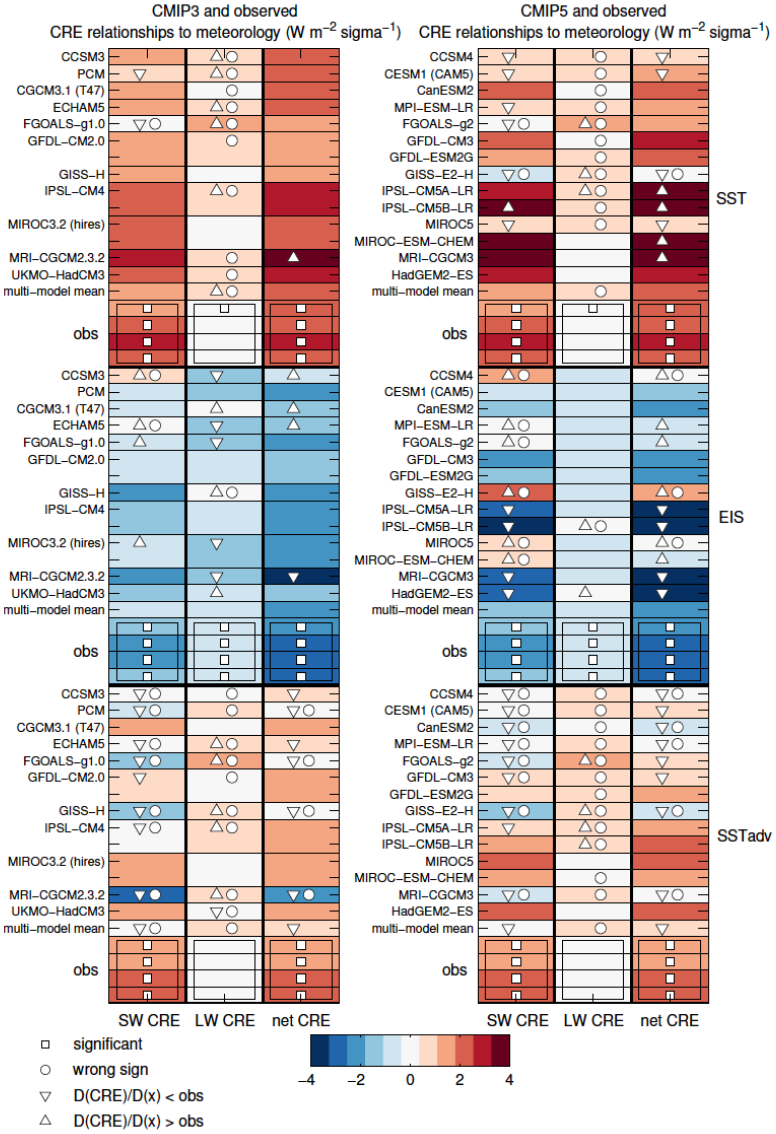

Figure 3.4: The (from left to right) shortwave, longwave, and net cloud radiative effect relationships to (from top to bottom) sea surface temperature, estimated inversion strength, and horizontal surface temperature advection for (left) CMIP3 and (right) CMIP5 models and observations. Each meteorological variable listed on the vertical axis represents x in $D(\text{CRE})/D(x)$, where CRE is SW, LW, or net CRE, listed on the horizontal axis. Observed values for each relationship from top to bottom are derived from CERES paired with CFSR, ERA-Interim, JRA-55, and MERRA. A square indicates that the observed value is significant at the 95% confidence level. A circle indicates that the simulated value has the wrong sign relative to observations. A downward (an upward)-pointing arrow indicates that the simulated value is less (greater) than each of the four observed values with 95% confidence.

Table 3.3: CMIP models used in the investigation. Values in the $\omega_{700} > 0$ column are the percentage of ocean grid boxes within 30°S – 30°N satisfying the criteria specified in the text for the different models. Asterisks denote those models providing ISCCP and CALIPSO-GOCCP simulator-derived cloud fraction. (Expansions of model acronyms are available online at "http://www.ametsoc.org/PubsAcronymList".)

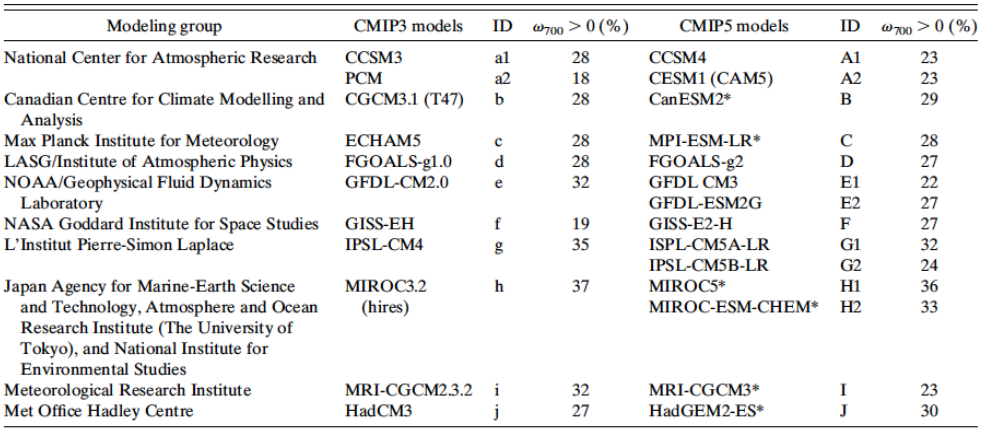

Modeling group	CMIP3 models	ID	$\omega_{700} > 0$ (%)	CMIP5 models	ID	$\omega_{700} > 0$ (%)
National Center for Atmospheric Research	CCSM3	a1	28	CCSM4	A1	23
	PCM	a2	18	CESM1 (CAM5)	A2	23
Canadian Centre for Climate Modelling and Analysis	CGCM3.1 (T47)	b	28	CanESM2*	B	29
Max Planck Institute for Meteorology	ECHAM5	c	28	MPI-ESM-LR*	C	28
LASG/Institute of Atmospheric Physics	FGOALS-g1.0	d	28	FGOALS-g2	D	27
NOAA/Geophysical Fluid Dynamics Laboratory	GFDL-CM2.0	e	32	GFDL CM3	E1	22
				GFDL-ESM2G	E2	27
NASA Goddard Institute for Space Studies	GISS-EH	f	19	GISS-E2-H	F	27
L'Institut Pierre-Simon Laplace	IPSL-CM4	g	35	ISPL-CM5A-LR	G1	32
				IPSL-CM5B-LR	G2	24
Japan Agency for Marine-Earth Science and Technology, Atmosphere and Ocean Research Institute (The University of Tokyo), and National Institute for Environmental Studies	MIROC3.2 (hires)	h	37	MIROC5*	H1	36
				MIROC-ESM-CHEM*	H2	33
Meteorological Research Institute	MRI-CGCM2.3.2	i	32	MRI-CGCM3*	I	23
Met Office Hadley Centre	HadCM3	j	27	HadGEM2-ES*	J	30

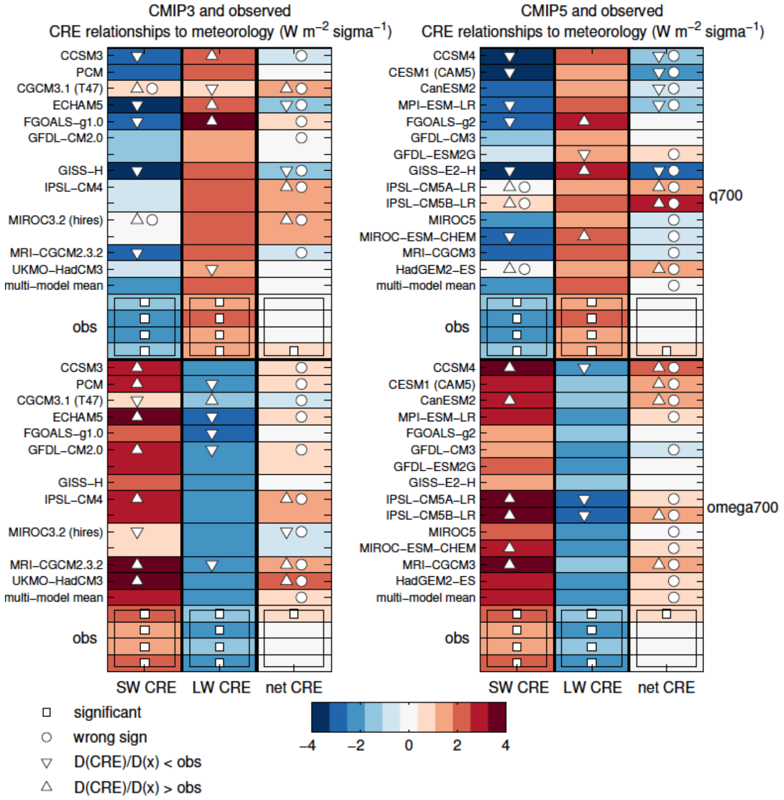

Figure 3.5: As in Fig. 3.4, but for (from top to bottom) specific humidity and pressure vertical velocity at 700 hPa.

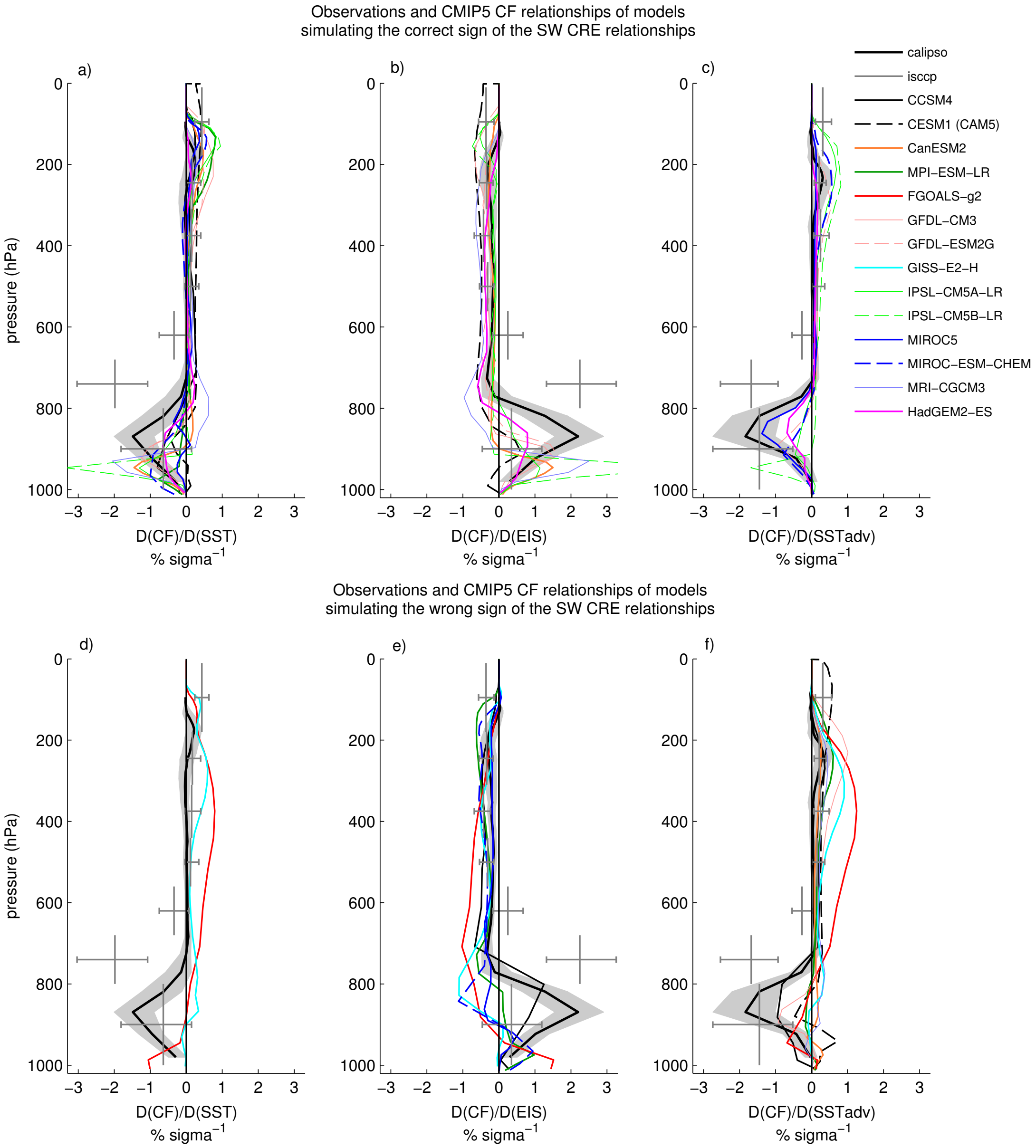

Figure 3.6: Cloud fraction relationship to sea surface temperature, estimated inversion strength, and horizontal surface temperature advection as a function of pressure in CMIP5 models, ISCCP, and CALIPSO. For each relationship, only those models that simulate the (a)–(c) correct or (d)–(f) incorrect sign of the shortwave cloud radiative effect relationship to the same meteorological variable are shown.

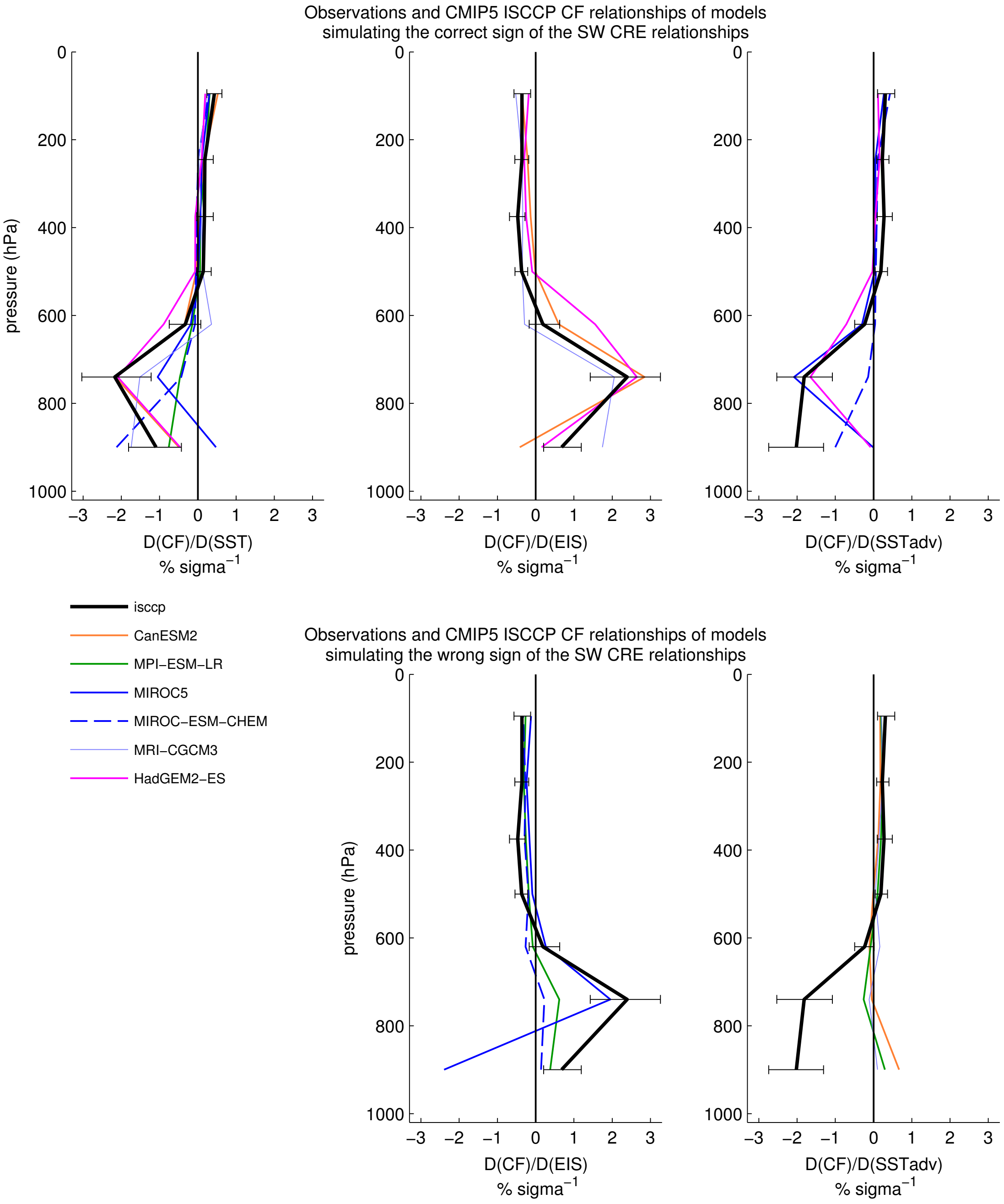

Figure 3.7: Cloud fraction relationship for sea surface temperature, estimated inversion strength, and horizontal surface temperature advection as a function of pressure in CMIP5 models employing the ISCCP simulator and ISCCP observations. For each relationship, only those models that simulate the (top) correct and (bottom) wrong sign of shortwave cloud radiative effect relationship to the same meteorological variable are shown. For both models and observations, only the random overlap version of ISCCP is shown. The error bars span the four 95% confidence intervals computed from the four reanalyses.

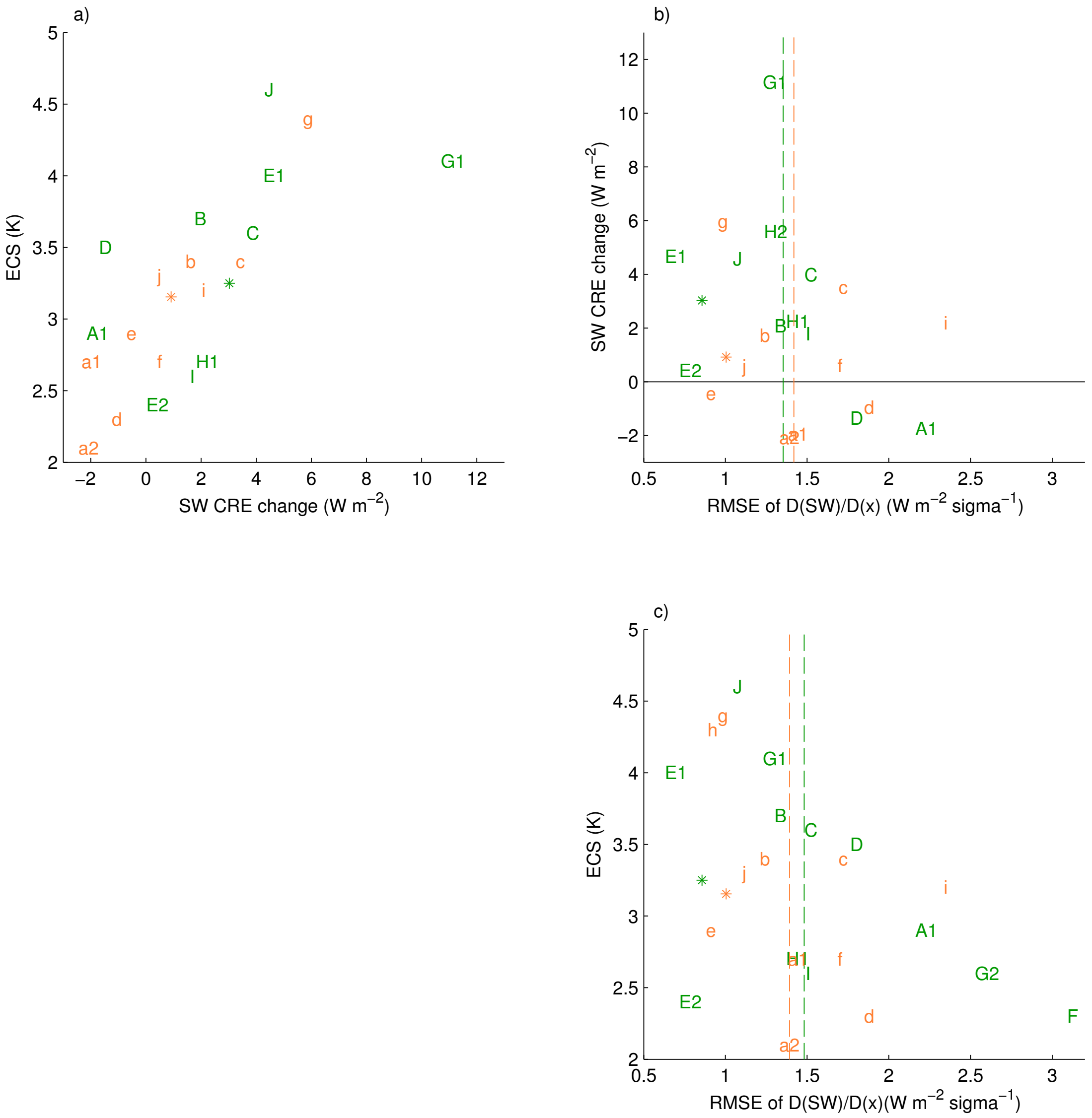

Figure 3.8: (a) Twenty-first-century change in SW CRE plotted against equilibrium climate sensitivity in models, (b) root-mean-square error (RMSE) of the simulated SW-CRE–meteorology relationships relative to observations plotted against simulated twenty-first-century SW-CRE change, and (c) RMSE of the simulated SW-CRE–meteorology relationships relative to observations plotted against equilibrium climate sensitivity. CMIP3 (CMIP5) models are denoted as orange (green) letters, which are defined in Table 3.3. The asterisks denote either the multimodel mean SW-CRE change or equilibrium climate sensitivity and the RMSE of the multimodel mean relationships. Vertical dashed lines show the median RMSE separately for CMIP3 and CMIP5 models. The median RMSEs of (b) and (c) are not identical because data for all models were not available.

Appendix

Quantifying the Relationship between Changes in CF and CRE

We also performed a more rigorous assessment of how observed and modeled changes in CF associated with meteorological variability are related to changes in CRE. To do this, we took advantage of the ISCCP CF data, binned according to cloud-top pressure (CTP) and cloud optical thickness (τ), as well as observational (*Zhou et al.*, 2013) and model-derived (*Zelinka et al.*, 2012) cloud radiative kernel datasets binned in an identical manner. A cloud radiative kernel is the change in top-of-atmosphere SW, LW, or net radiation per unit change in CF. For a given month, it depends primarily on τ, CTP, clear-sky albedo, and latitude. The radiative kernels we use are annually averaged between 30°S and 30°N for a clear-sky albedo of 0.07, which is the albedo of the ocean surface used in the ERA-Interim. The observational kernels are very similar to those derived from models.

We computed $D(\mathrm{CF})/D(x)$ as described in the data and methods section for the binned ISCCP data and multiplied the values by the cloud radiative kernels. For each bin, this essentially yields the change in top-of-atmosphere CRE associated with a change in a typical anomaly of the meteorological property x. Mathematically, this can be written as $[D(\mathrm{CF})/D(x)] \times [D(\mathrm{CRE})/D(CF)]$. For the observations, the binned relationships of SW, LW, and net CRE to the meteorological variables are shown in Figs. A3.1–A3.3. The overall (i.e., integrated over all CTP layers and τ categories) enhancement of SW CRE associated with anomalously cool SST, strong EIS, and cold SSTadv is dominated by an increase in CF of clouds in the lower troposphere with medium τ. Because the binned LW-CRE changes associated with such meteorological conditions are small, the binned net-CRE changes resemble those of SW CRE. The binned relationships between CRE and both q_{700} and ω_{700} are more complicated. The overall enhancement and offsetting components of SW and LW CRE associated with anomalously high q_{700} and weak ω_{700} each have large contributions from an increase in CF of clouds in the middle and upper troposphere with varying values of τ. The sum of each of the binned relationships between CRE and the meteorology over all CTP layers and τ categories is quantitatively similar to the CRE relationships computed from CERES (Figs. 3.2, 3.4, and 3.5). This establishes confidence in both sets of results.

Not all CMIP5 models provide the ISCCP simulator output that allows us to compute binned SW-CRE relationships. Therefore, to infer qualitatively how changes in CF in each model impact SW CRE in models not employing the ISCCP simulator, we show in Fig. A3.4 the 1980–2005 mean annual vertical profile of cloud water content (CWC) of the CMIP5 models (data for CMIP3 models were unavailable). CWC at each model level is defined as $(\rho_a m_t)/\mathrm{CF}$, where ρ_a is the density of dry air, and m_t is the total (liquid plus ice) water mixing ratio in a grid box. Dividing by CF allowed us to examine the total water content within a cloud. The relevant features of Fig. A3.4 are described in the results section.

For the six models providing ISCCP simulator output, we computed binned SW-CRE relationships to SST, EIS, and SSTadv in the manner described above. For these models and observations, we summed the relationships over all τ categories for each CTP layer to yield profiles of changes in SW CRE for the same meteorological variations, shown in Fig. A3.5. The results confirm that for these models and observations, changes in low-level CF drive the overall changes in SW CRE associated with variability of SST, EIS, and SSTadv.

Components of SW CRE relationships to SST, EIS, and SSTadv

Changes in top-of-atmosphere SW CRE arise primarily due to changes in total cloud amount and cloud optical depth. Changes in cloud-top altitude play a minor role. To determine the relative contributions of each factor to the SW CRE relationships to SST, EIS, and SSTadv, we use the method of *Zelinka et al.* (2012) for the ISCCP observations and those models providing ISCCP simulator output. The method is outlined below.

Cloud amount component

To compute the cloud amount component of the relationship between SW CRE and a meteorological variable x, $D(\mathrm{SW}_{\mathrm{amt}})/D(x)$, first we express the climatological mean total cloud fraction, $\langle \mathrm{CF}_{\mathrm{tot}} \rangle$, as

$$\langle \mathrm{CF}_{\mathrm{tot}} \rangle = \sum_{\tau=1}^{T} \sum_{p=1}^{P} \langle \mathrm{CF}[p,\tau] \rangle, \tag{A3.1}$$

where $\langle \mathrm{CF}[p,\tau] \rangle$ is the climatological mean cloud fraction at a given cloud-top pressure layer p and optical thickness category τ, and P and T are the total number of respective bins of cloud-top pressure and optical thickness. Next, we express the relationship between total CF and x as

$$\frac{D(\mathrm{CF})_{\mathrm{tot}}}{D(x)} = \sum_{\tau=1}^{T} \sum_{p=1}^{P} \frac{D(\mathrm{CF}[p,\tau])}{D(x)}, \tag{A3.2}$$

where $D(\mathrm{CF}[p,\tau])/D(x)$ is the relationship between CF and x at a given p and τ. Finally, $D(\mathrm{SW}_{\mathrm{amt}})/D(x)$ is computed as

$$\frac{D\mathrm{SW}_{\mathrm{amt}}}{D(x)} = \sum_{\tau=1}^{T} \sum_{p=1}^{P} \frac{D(\mathrm{CF}_{\mathrm{tot}})}{D(x)} \times \frac{\langle \mathrm{CF}[p,\tau] \rangle}{\langle \mathrm{CF}_{\mathrm{tot}} \rangle} \times \mathrm{SW}_k[p,\tau], \tag{A3.3}$$

where $\mathrm{SW}_k[p,\tau]$ is the shortwave cloud radiative kernel at a given p and τ. The resulting quantity is interpreted as the change in SW radiation, in response to a perturbation in x, due to a change in total cloud amount independent of the change in the clouds' optical depth and vertical distribution.

Cloud optical depth component

To compute the cloud optical depth component of the relationship between SW CRE and x, $D(\mathrm{SW}_\tau)/D(x)$, first we calculate the mean $D(\mathrm{CF}[p,\tau])/D(x)$ over all τ for a given p. Mathematically this is written as

$$\left\langle \frac{D(\mathrm{CF}[p])}{D(x)} \right\rangle = \frac{1}{T} \sum_{\tau=1}^{T} \frac{D(\mathrm{CF}[p,\tau])}{D(x)}. \tag{A3.4}$$

Then $D(\mathrm{SW}_\tau)/D(x)$ is computed as

$$\frac{D(\mathrm{SW}_\tau)}{D(x)} = \sum_{\tau=1}^{T}\sum_{p=1}^{P}\Big(\Big(\frac{D(\mathrm{CF}[p,\tau])}{D(x)} - \Big\langle\frac{D(\mathrm{CF}[p])}{D(x)}\Big\rangle\Big) \times \mathrm{SW}_k[p,\tau]\Big). \tag{A3.5}$$

The resulting quantity is interpreted as the change in SW radiation, in response to a perturbation in x, due to a change in the clouds' optical depth distribution independent of the change in the clouds' vertical distribution and change in total cloud amount.

Results

Note that the overall change in SW radiation in response to a change in x, $D(\mathrm{SW})/D(x)_k$ is expressed as

$$\frac{D(SW)}{D(x)_k} = \sum_{\tau=1}^{T}\sum_{p=1}^{P}\frac{D(\mathrm{CF}[p,\tau])}{D(x)} \times \mathrm{SW}_k[p,\tau]. \tag{A3.6}$$

For observations and models, Fig. A3.6 shows this quantity plotted against the relationship between SW CRE and x, which we call $D(\mathrm{SW})/D(x)$. The two quantities are nearly identical for all observations and models.

Figure A3.6 also shows $D(\mathrm{SW})/D(x)_k$ plotted against $D(\mathrm{SW}_{\mathrm{amt}})/D(x)$, $D(\mathrm{SW}_{\mathrm{tau}})/D(x)$, and $D(\mathrm{SW}_{\mathrm{amt}})/D(x)+D(\mathrm{SW}_{\mathrm{tau}})/D(x)$ for observations and models. The sum of the cloud amount and optical depth components is sufficient to explain the sign and magnitude of all observed and modeled $D(\mathrm{SW})/D(x)_k$ values. Interestingly, the cloud amount and optical depth components have similar signs in most models, so that individually either can generally explain the sign of $D(\mathrm{SW})/D(x)_k$. Their magnitudes are also similar. However, $D(\mathrm{SW}_{\mathrm{amt}})/D(x)$ explains more inter-model variance in $D(\mathrm{SW})/D(x)_k$ compared to $D(\mathrm{SW}_{\mathrm{tau}})/D(x)$, justifying our focus on cloud fraction in the main text. In observations, $D(\mathrm{SW})/D(\mathrm{SST})_k$ and $D(\mathrm{SW})/D(\mathrm{EIS})_k$ each have cloud amount and optical depth contributions of the same sign, whereas $D(\mathrm{SW})/D(\mathrm{SSTadv})_k$ only has a cloud amount contribution.

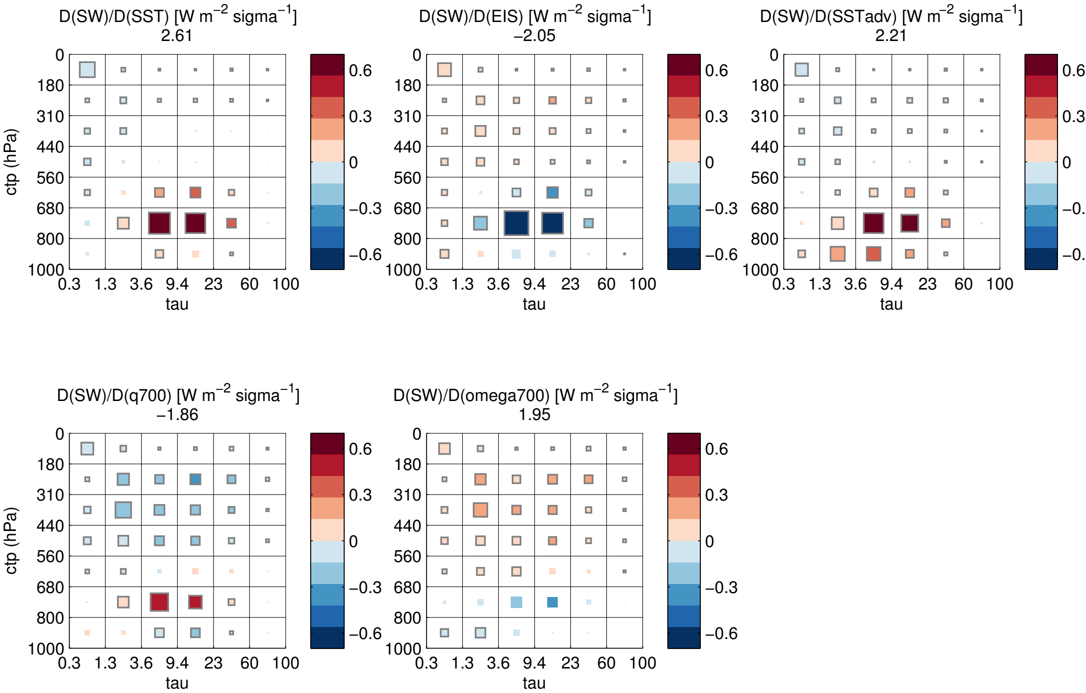

Figure A3.1: Observed ISCCP cloud fraction relationships to meteorological variables multiplied by the shortwave cloud radiative kernel, binned by CTP and τ. The area of the box within each bin is proportional to the $D(\mathrm{CF})/D(x)$ value therein, and a solid gray line around a box indicates that a value is significant at the 95% confidence level. The sum of values over all CTP layers and τ categories is shown at the top of each subplot.

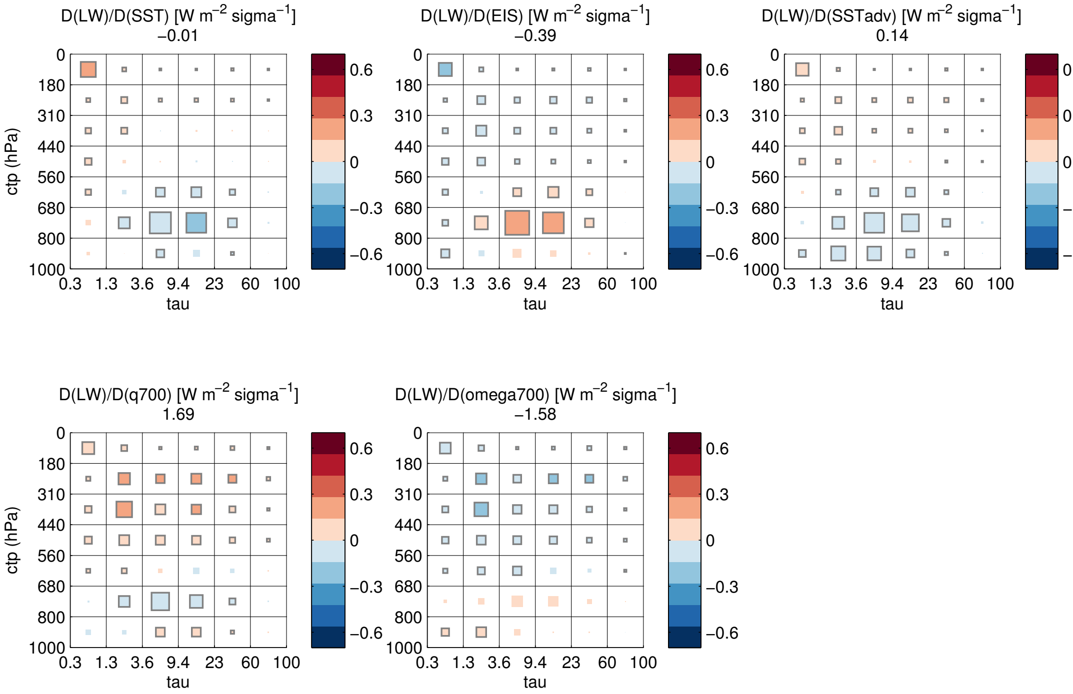

Figure A3.2: As in Fig. A3.1, but for the longwave cloud radiative kernel.

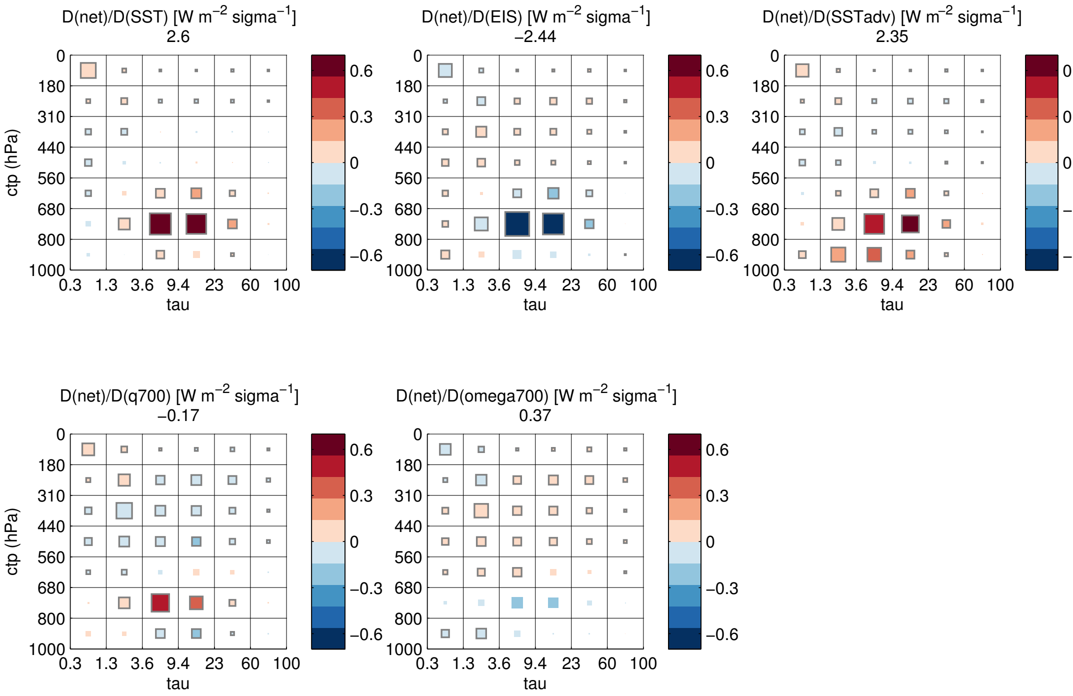

Figure A3.3: As in Fig. A3.1, but for the net cloud radiative kernel.

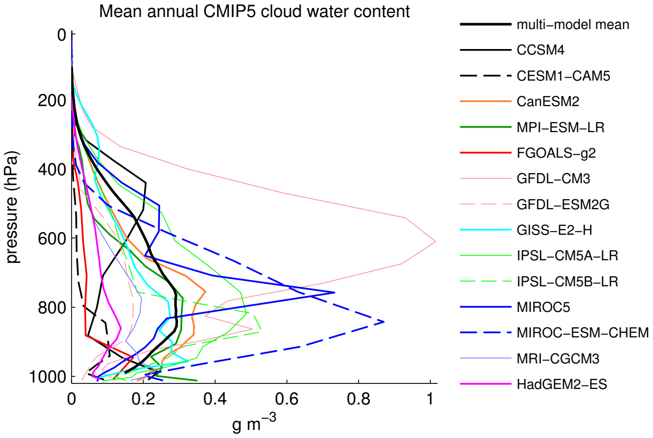

Figure A3.4: The 1980–2005 mean annual cloud water content as a function of pressure in CMIP5 models.

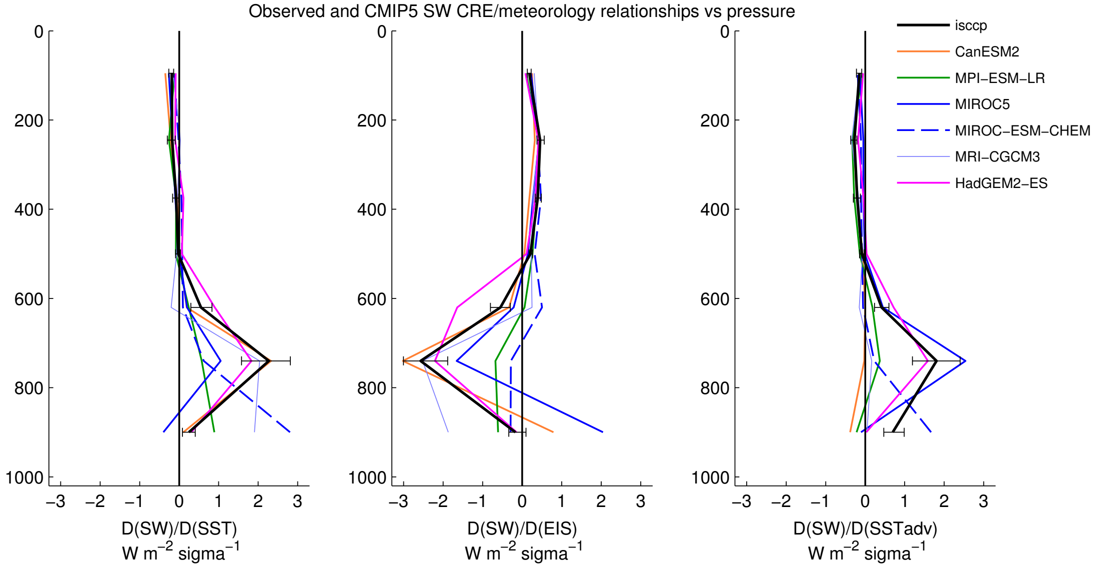

Figure A3.5: Observed and modeled ISCCP cloud fraction relationships to (left)–(right) SST, EIS, and SSTadv multiplied by the shortwave cloud radiative kernel, summed over all optical thickness categories. The error bars span the four 95% confidence intervals computed from the four reanalyses.

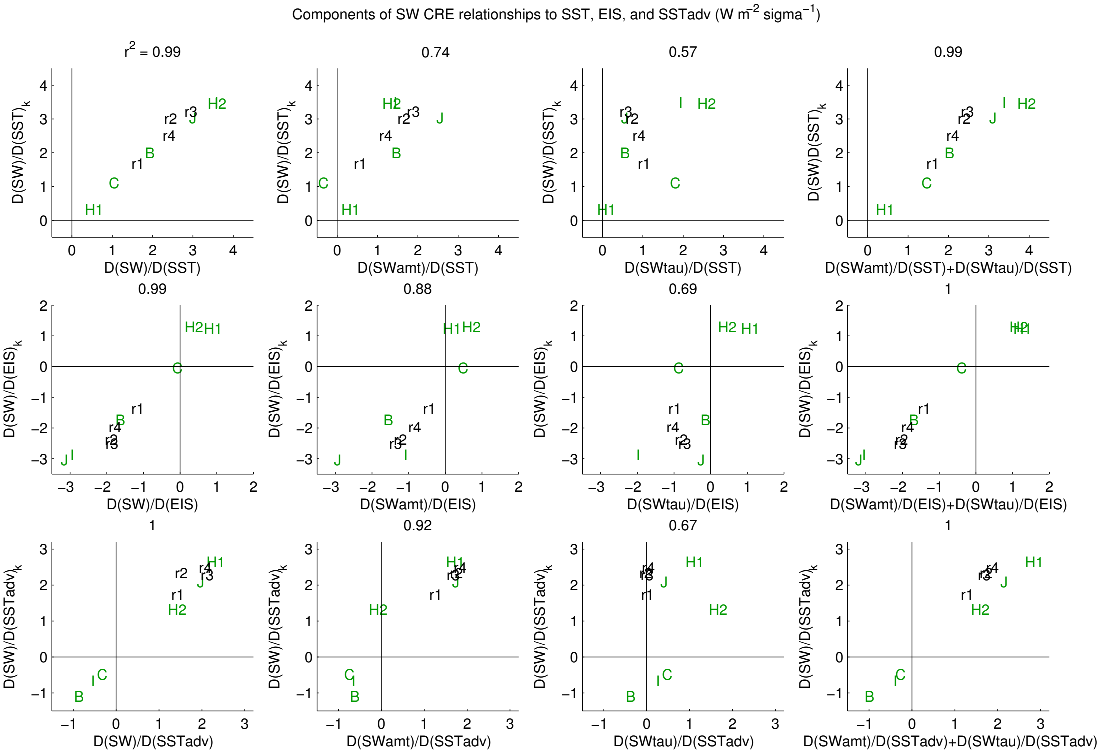

Figure A3.6: SW CRE relationships to SST, EIS and SSTadv plotted against SW/meteorology relationships computed using cloud radiative kernel method (left panels). Cloud amount component of SW/meteorology relationships plotted against SW/meteorology relationships (second from left panels). Cloud optical depth component of SW/meteorology relationships plotted against SW/meteorology relationships (second from right panels). Sum of cloud amount and optical depth components of SW/meteorology relationships plotted against SW/meteorology relationships (right panels). Observations are denoted as black letters, where r1 stands for CFSR, r2 for ERA-Interim, r3 for JRA55, and r4 for MERRA, each paired with CERES (for CRE method) or ISCCP (for kernel method). Models are denoted as green letters (defined in Table 3.3 in the main text). Numbers on the top of each subplot are the r-squared values of the modeled quantities.

Chapter 4

Observational and model estimates of subtropical marine boundary layer cloud feedbacks

Low-level clouds over the eastern subtropical oceans strongly modulate the energy budget of the climate due to their high albedo (*Hartmann et al.*, 1992). Just a fractional change in their global horizontal coverage exerts a radiative forcing at the top of the atmosphere greater than that caused by a doubling of the atmospheric concentration of CO_2 (*Wood*, 2012). Climate models project a wide spread of changes in these clouds in anthropogenic warming simulations (*Bony and Dufresne*, 2005; *Qu et al.*, 2013). A decrease (increase) in subtropical cloudiness in the future climate implies a positive (negative) feedback to global warming. Models that predict a decrease in subtropical cloudiness in the future climate tend to simulate more global warming than models that predict an increase in cloudiness (*Myers and Norris*, 2015). Evaluating and seeking to constrain the inter-model spread in the subtropical cloud feedback should thus play a key role in any effort to reduce uncertainty in global warming estimates.

Stratocumulus and shallow cumulus are the primary low-level cloud types occurring over the subtropical oceans. Collectively, we refer to them as marine boundary layer (MBL) clouds because they occur within the planetary boundary layer in similar climatological conditions. These include a cool ocean surface relative to the zonal mean, a temperature inversion separating the MBL from the free troposphere, cold air advection near the surface, a dry free troposphere, and subsidence (*Albrecht et al.*, 1995; *Norris*, 1998a; *Myers and Norris*, 2015). Such meteorological properties are key to generating and sustaining MBL clouds and can be considered as external cloud forcing parameters in both simple and complex models of the cloudy MBL (*Lilly*, 1968; *Blossey et al.*, 2013).

Given that the meteorological environment of MBL clouds will change in the future climate, determining the sensitivity of MBL clouds to perturbations in external forcing parameters has been the focus of many studies (see e.g. *Wood*, 2012, and references therein). Observational studies tackling this problem have found that smaller low-level cloud fraction (CF) and/or less solar reflection by subtropical clouds is associated with relatively warm sea-surface temperature (*Hanson*, 1991; *Norris and Leovy*, 1994; *Clement et al.*, 2009; *Myers and Norris*, 2015), a weaker temperature inversion (*Klein and Hartmann*, 1993; *Wood and Bretherton*, 2006; *Sun et al.*, 2011; *Myers and Norris*, 2013), reduced cold advection by surface winds (*Klein et al.*, 1995; *Park and Leovy*, 2004; *Norris and Iacobellis*, 2005; *Myers and Norris*, 2015), and enhanced subsidence (*Myers and Norris*, 2013). Theoretical studies have found similar relationships (*Bretherton and Wyant*, 1997; *Blossey et al.*, 2013; *Bretherton et al.*, 2013). In the previous chapter, also published in *Myers and Norris* (2015), we discovered that climate models simulate a wide range of these relationships on interannual timescales in terms of both sign and magnitude, suggesting why models predict vastly different subtropical cloud feedbacks and hence climate sensitivities.

Can these relationships be used to evaluate and constrain the inter-model spread of changes in subtropical clouds? A recent study by *Qu et al.* (2013) suggests that this is possible. In that study, a statistical model employing the CF/SST relationship was able to explain 50–64% of the inter-model variability of subtropical CF trends in climate change simulations of models participating in phases 3 and 5 of the Coupled Model Intercomparison Project (CMIP3 and CMIP5, respectively) (*Meehl et al.*, 2007; *Taylor et al.*, 2007). *Qu et al.* (2013) argued that the general decrease in CF projected by the models in a perturbed climate is likely to occur based on the observed sensitivity of CF to increases in SST and estimated inversion strength (EIS). *Caldwell et al.* (2013) predicted future changes in CF using a mixed-layer model forced by the climate change perturbations simulated by an ensemble of CMIP3 models. Perhaps surprisingly, they found that the inter-model variability in CF trends was not reduced compared with what the models actually predict. Their mixed-layer model predicted an increase in CF due primarily to an increase in EIS in the future climate, which they argued was more realistic than the general decrease in CF simulated by the CMIP3 ensemble.

One drawback of these studies is that changes in CF are not guaranteed to produce proportional changes in shortwave cloud radiative effect (SW CRE), which is the parameter that is more directly related to the subtropical cloud feedback and ultimately to climate sensitivity. Furthermore, even if models project the same change in SW CRE, they may simulate different cloud feedbacks – defined as the trend in SW CRE per unit change in global mean surface temperature. A more insightful approach to investigating inter-model differences in subtropical cloud trends would be to examine and attempt to constrain cloud feedbacks rather than changes in SW CRE or CF alone.

In this study, we seek to explain the sign and strength of the subtropical cloud feedback in idealized climate change simulations of 19 CMIP5 models. Specifically, we will assess the trends in subtropical mean SW CRE in an instantaneous quadrupling of CO_2 experiment mediated purely by an increase in global mean temperature. A multi-linear regression model based on the simulated interannual variability of the current climate will be employed to predict changes in SW CRE per unit change in global mean temperature based on perturbations in SST, EIS, horizontal advection over the SST gradient (SSTadv), relative humidity at 700 hPa (RH_{700}), and pressure vertical velocity at 700 hPa (ω_{700}). We also seek to constrain the subtropical cloud feedback using observations provided by satellite data and reanalyses.

4.1 Data and methods

4.1.1 Observational data

SW CRE is defined as clear-sky minus all-sky radiation at the top of the atmosphere. 2000–2012 and 1984–1999 observed monthly mean values of this quantity are taken respectively from the Clouds and Earth's Radiant Energy System (CERES) Energy Balanced and Filled (EBAF) dataset version 2.7 (*Loeb et al.*, 2009) and the International Satellite Cloud Climatology Project (ISCCP) (*Rossow and Schiffer*, 1999). ISCCP data were corrected for artifacts as in *Norris and Evan* (2015). Although ISCCP provides data through 2009, we only use retrievals from the period that does not overlap with the CERES record, allowing for an assessment of two truly independent cloud datasets.

Four different reanalyses provide 1984–2012 monthly mean values of SST, EIS, SSTadv, RH_{700}, and ω_{700}. These include the Climate Forecast System Reanalysis (CFSR) (*Saha et al.*, 2010), the Interim European Centre for Medium Range Weather Forecasts (ECMWF) Re-Analysis (ERA-Interim) (*Dee et al.*, 2011), the Japanese 55-year Reanalysis Project (JRA-55) (*Ebita et al.*, 2011), and the Modern-Era Retrospective Analysis for Research and Applications (MERRA) (*Rienecker et al.*, 2011). EIS – a measure of the strength of the temperature inversion above cloud top formulated by *Wood and Bretherton* (2006) – and SSTadv are computed as described in the preceding chapter and *Myers and Norris* (2015). Each dataset was bilinearly interpolated onto a $2.5^\circ \times 2.5^\circ$ grid. It is unclear which reanalysis is the best representation of the climate record, so we averaged each of the five meteorological fields over the four reanalyses to attain a single merged reanalysis product. We consider the resulting dataset to be the best approximation of observations.

4.1.2 Model output

We analyze monthly mean output from 19 coupled climate models participating in CMIP5, listed in Table 4.1. All fields were interpolated onto a $2.5^\circ \times 2.5^\circ$ grid prior to analysis. Only models with unique atmospheric components from each modeling center were chosen. In this way, we exclude examination of multiple model variants with identical atmospheric components but different land or ocean components or resolutions. This is justified by our focus on the factors affecting the inter-model spread of the subtropical cloud feedback, which is likely uniquely determined by the atmospheric component of a particular model.

A single realization of both the "piControl" and "abrupt4xCO_2" experiments is used for each model. The former is a control simulation in which forcing constituents are held fixed at preindustrial values. The latter is a simulation lasting at least 150 years in which, at the start of the run, the concentration of atmospheric CO_2 is quadrupled instantaneously relative to pre-industrial values. All other forcing constituents are identical to those in the control run.

4.1.3 Computation of cloud feedbacks and multi-linear regression model

Our domain is defined dynamically similar to the method used in previous chapters, published in *Myers and Norris* (2013) and *Myers and Norris* (2015). For the observations, we examine all grid boxes occurring under 1984–2012 long–term mean subsidence ($\omega_{700} > 0$) for each calendar month within the ocean region between 30°N and 30°S and for which monthly mean subsidence occurs for 80% of the time record. Only months experiencing mean subsidence are included in the analysis. For the models, this constraint applies jointly for the control and 4xCO_2 runs. This ensures that regions that occur under mean subsidence in the control climate but not in the perturbed climate (e.g. due to a shift in convection) are excluded. Note that since observations and models may have different areas experiencing mean subsidence, the geographical area satisfying our criteria is not guaranteed to be identical across reanalyses and models.

We quantify the subtropical cloud feedback in each model as the domain mean SW CRE of years 121–140 of the 4xCO_2 run minus that of years 1–20, divided by the increase in global mean temperature between the two time periods. By examining the normalized change in SW CRE over the 4xCO_2 run, the so called fast cloud adjustment to the abrupt increase in CO_2 (not mediated by the increase in global mean temperature) is omitted in our computation of cloud feedback (*Gregory and Webb*, 2008; *Andrews et al.*, 2012a). Note that the choice of years here corresponds to periods for which ISCCP simulator output (*Pincus et al.*, 2012; *Zhang et al.*, 2012) is available. Output from models employing the ISCCP simulator will be used to assess how clouds at different altitudes contribute to the SW CRE feedback.

The goal of the present study is to understand and place an observational constraint on the inter-model spread of this feedback. To accomplish this, first we assume that SW CRE is a function of SST, EIS, SSTadv, RH_{700}, and ω_{700}. These variables are a reasonable approximation of the complete set of external parameters for a mixed-layer model of the cloudy MBL (*Lilly*, 1968). We can then write a first order Taylor series approximation of the change in SW CRE per unit change in global mean temperature T as

$$\frac{d\mathrm{SW}}{dT} = \sum_{i=1}^{5} \frac{\partial \mathrm{SW}}{\partial x_i} \frac{dx_i}{dT}, \tag{4.1}$$

where x_i is one of the five forcing variables. $\partial\mathrm{SW}/\partial x_i$ represents the direct response of SW CRE to a perturbation in x_i, and dx_i/dT represents the change in x_i mediated by a change in T. For each grid box we compute the latter derivative as the mean value of x_i in years 121–140 of the $4\mathrm{xCO}_2$ run minus that of years 1–20, divided the increase in T between the two time periods. To compute the partial derivatives of SW CRE with respect to each forcing parameter, we construct a multi-linear regression model from the time series of detrended, deasonalized monthly anomalies in each model's control climate. For each grid box SW CRE is then approximated as

$$\mathrm{SW} \approx \sum_{i=1}^{5} a_i x_i + b. \tag{4.2}$$

Each coefficient a_i is equal to $\partial\mathrm{SW}/\partial x_i$. Partial derivatives are also computed in this manner using anomalies of observations. Detrending ensures that potential unphysical trends in the reanalyzes do not contaminate the observational results. Each partial derivative represents the sensitivity of SW CRE to a change in some cloud-controlling factor when all other factors are held fixed. Covariability among the x_i does not alter this interpretation (see Appendix).

Decomposing each partial derivative and change in external parameter for the models into a domain average value plus a perturbation term, the spatially averaged predicted feedback described by Eq. 4.1 yields

$$\left\langle \frac{d\mathrm{SW}}{dT} \right\rangle = \sum_{i=1}^{5} \left\langle \frac{\partial \mathrm{SW}}{\partial x_i} \right\rangle \left\langle \frac{dx_i}{dT} \right\rangle + \left\langle \frac{\partial \mathrm{SW}'}{\partial x_i} \frac{dx_i{}'}{dT} \right\rangle. \tag{4.3}$$

The covariance term is found to be negligibly small, so that

$$\left\langle \frac{d\mathrm{SW}}{dT} \right\rangle \approx \sum_{i=1}^{5} \left\langle \frac{\partial \mathrm{SW}}{\partial x_i} \right\rangle \left\langle \frac{dx_i}{dT} \right\rangle. \tag{4.4}$$

By estimating the subtropical cloud feedback in this fashion, we are able to determine the role of changes in external forcing parameters in the perturbed climate in generating the cloud feedback in each model. While we do not expect this diagnostic technique to perform perfectly for each model, we expect that the results will elucidate reasons for the sign and magnitude of cloud feedbacks produced in the CMIP5 ensemble.

4.1.4 Determining observational uncertainty

Standard errors of the observed partial derivatives are computed as the square roots of the diagonal elements of the variance-covariance matrix $\mathbf{C}$ of regression coefficients (*Press et al.*, 1996). This matrix is formulated as $\mathbf{C} = \hat{\sigma}^2(\mathbf{X}^T\mathbf{X})^{-1}$, where $\mathbf{X}$ is the gram matrix with columns composed of the time series of each x_i and a column of ones, and $\hat{\sigma}^2$ is the mean of squared residuals of the regression model. Assuming the errors are normally distributed, we then calculate a 90% confidence interval for each grid box's partial derivative as

$$\frac{\partial \mathrm{SW}}{\partial x_i} \pm t\sqrt{\mathbf{C}_{ii}}\sqrt{N_{\mathrm{nom}}/N_{\mathrm{eff}}}, \tag{4.5}$$

or equivalently

$$\frac{\partial \mathrm{SW}}{\partial x_i} \pm \delta, \tag{4.6}$$

where N_{nom} (N_{eff}) is the nominal (effective) number of points in the time series, and t is the critical value of the student's t test at the 95% significance level with degrees of freedom equal to $N_{\mathrm{eff}} - 6$. The right most term in Eq. 4.5 takes into account that the time series of SW CRE may be auto-correlated. N_{eff} is formulated as

$$N_{\mathrm{eff}} = N_{\mathrm{nom}}\Big(\frac{1-r_T}{1+r_T}\Big), \tag{4.7}$$

where r_T is the lag one auto-correlation coefficient of the time series of SW CRE. Finally a 90% confidence interval for the domain average partial derivative is computed as

$$\Big\langle\frac{\partial \mathrm{SW}}{\partial x_i}\Big\rangle \pm \sqrt{\sum_{k=1}^{N'_{\mathrm{nom}}} \frac{\delta_k^2}{N'^2_{\mathrm{eff}}}}, \tag{4.8}$$

or equivalently

$$\Big\langle\frac{\partial \mathrm{SW}}{\partial x_i}\Big\rangle \pm \Delta, \tag{4.9}$$

where N'_{nom} (N'_{eff}) is the nominal (effective) number of points over the domain, and δ_k is the uncertainty for the kth grid box. N'_{eff} is formulated as

$$N'_{\mathrm{eff}} = N'_{\mathrm{nom}}\Big(\frac{1-r_Z}{1+r_Z}\Big)\Big(\frac{1-r_M}{1+r_M}\Big), \tag{4.10}$$

where r_Z and r_M are the zonal and meridional lag one auto-correlation coefficients computed using the zonal and meridional anomalies of $\partial\mathrm{SW}/\partial x_i$ of all latitude and longitude bands, respectively.

We desire a single value and confidence interval for each of the five partial derivatives in the regression model. However, since two cloud datasets and one merged reanalysis are used in this study, there are two observational estimates for each coefficient. To attain a single observational value for each $\big\langle\partial\mathrm{SW}/\partial x_i\big\rangle$, we take the mean of these two estimates. By propagating uncertainty between datasets, a 90% confidence interval bounding this value is computed as

$$\Big\langle\frac{\partial \mathrm{SW}}{\partial x_i}\Big\rangle \pm \sqrt{\frac{\Delta^2_{\mathrm{CERES}} + \Delta^2_{\mathrm{ISCCP}}}{2^2}}. \tag{4.11}$$

Here, Δ_{CERES} is the uncertainty of the observational estimate derived from CERES, and Δ_{ISCCP} is that derived from ISCCP. This method of computing the uncertainty assumes that the CERES and ISCCP estimates are independent. This assumption is justified because the cloud datasets provide SW CRE using different satellites with unique retrieval algorithms and have non-overlapping time periods of record.

4.2 Results

4.2.1 Contributions to SW CRE feedbacks

Figure 4.1 shows subtropical mean trends of the meteorological variables in the perturbed climate per unit increase in global mean temperature; observed and simulated partial derivatives of SW CRE with respect to SST, EIS, SSTadv, RH_{700}, and ω_{700}; and the actual and predicted SW CRE feedback for the CMIP5 ensemble. The predicted feedback is further broken into its components, each of which is defined as $\left\langle \partial \mathrm{SW}/\partial x_i \times dx_i/dT \right\rangle$. Partial derivatives and trends in external parameters are normalized by the respective standard deviations of the observed 1984–2012 domain mean time series of detrended interannual anomalies of each meteorological variable.

In the future climate, per unit increase in global mean temperature, the ensemble mean exhibits a strong increase in subtropical average SST, an increase in EIS and RH_{700}, and very small changes in SSTadv and ω_{700} (weakly enhanced cold SSTadv and slightly weaker subsidence). With the exception of the increase in RH_{700}, these changes over the subtropical ocean regions simulated by CMIP3 or CMIP5 models have been documented by previous studies (*Bretherton and Blossey*, 2013; *Caldwell et al.*, 2013; *Qu et al.*, 2013) and are considered to be realistic responses to greenhouse forcing. Relative humidity is often assumed to not change very much under anthropogenic warming, so the result that free-tropospheric relative humidity over the eastern subtropical oceans increases substantially when scaled by its observed interannual standard deviation is an interesting result in itself.

To elucidate the regression results, it is useful to consider how meteorological perturbations of the same sign as their climate change signal are related to interannual variations of SW CRE in the control/observed climate. These relationships are quantified as the partial derivatives shown in Fig. 4.1. For observations and the ensemble mean, more positive SW CRE (less solar reflection) is associated with anomalously warm SST. When multiplied by the increase in SST in the future climate, this relationship leads to a large positive feedback in most models. More negative SW CRE (more solar reflection) in the control and observed climates is associated with anomalously strong EIS, high RH_{700}, enhanced cold SSTadv, and weaker ω_{700}. When multiplied by the appropriate changes in meteorological variables, these relationships lead to small negative feedbacks (for the increase in EIS and RH_{700}) or near zero feedbacks (for the small changes in SSTadv and ω_{700}) in most models. Overall, for the ensemble mean, the positive feedback due to warmer SST dominates over the smaller negative feedbacks due to stronger EIS and higher RH_{700}. This yields a positive predicted SW CRE feedback.

The regression model therefore captures the correct sign of the actual ensemble mean SW CRE feedback (also shown in Fig. 4.1), though with a larger magnitude. Moreover, with the exception of one outlier, the inter-model spread of the predicted feedback is similar to that of the actual feedback and clearly dominated by the SST component $\left\langle \partial \mathrm{SW}/\partial \mathrm{SST} \times d\mathrm{SST}/dT \right\rangle$.

A more rigorous test of how the multi-linear regression model performs is presented in Fig. 4.2, showing a scatter plot of the predicted versus actual SW CRE feedback for all models. To highlight the most important components contributing to the feedback estimated via regression, scatter plots of the predicted SW CRE feedback for the SST component, SST+EIS components, and SST+EIS+RH_{700} components are also shown. Excluding the outlier model "P", the regression model explains 38% of the inter-model variability in the SW CRE feedback. As inferred from Fig. 4.1, most of the spread in the feedback is explained by the SST component, which alone explains 52% of inter-model variability. Hence, about half of the inter-model variability in SW CRE feedbacks in the CMIP5 ensemble is explained by differences in the strength of the positive SW CRE feedback induced by warming subtropical SST. This corroborates the findings of *Qu et al.* (2013), who found that a similar amount of inter-model variance in 21$^{\mathrm{st}}$ century changes in subtropical low-level CF is explained by the SST component of a similarly constructed statistical model. It is important to note, though, that changes in CF are not equivalent to cloud feedbacks.

Figure 4.2 also shows that the addition of the EIS and RH$_{700}$ components to the SST part of the regression model each reduces the root mean square of the residuals, suggesting that the increase in both EIS and RH$_{700}$ in the future climate collectively leads to a non-negligible negative SW CRE feedback in most models.

Still, the full regression model explains only a modest amount of the spread in the cloud feedback, and the magnitude of the residuals is substantial. This implies that some predictor variable(s) is (are) missing from the regression model and/or that interannual variability of SW CRE in the control climate cannot always be used to estimate any particular model's SW CRE feedback.

4.2.2 Performance of the regression model

We contend that for our regression method to perform well for a given model, the factors controlling the interannual variability of SW CRE in its control climate should be the same as or similar to those controlling SW CRE variability in observations. To explore this hypothesis, for each model we compute the root-mean-square error (RMSE$_{\partial\mathrm{SW}/\partial x}$) of all five partial derivatives relative to observations. This is expressed as

$$\mathrm{RMSE}_{\partial\mathrm{SW}/\partial x} = \sqrt{\frac{1}{5}\sum_{i=1}^{5}\Big(\frac{\partial\mathrm{SW}^{\mathrm{model}}}{\partial x_i} - \frac{\partial\mathrm{SW}^{\mathrm{obs}}}{\partial x_i}\Big)^2}, \qquad (4.12)$$

where $\partial\mathrm{SW}/\partial x_i^{\mathrm{model}}$ is one of the five spatially averaged relationships for a given model, and $\partial\mathrm{SW}/\partial x_i^{\mathrm{obs}}$ is the mean value of the observed relationships derived from CERES and ISCCP. Next we plot RMSE$_{\partial\mathrm{SW}/\partial x}$ versus the absolute value of the difference between the actual and predicted SW CRE feedback for all models (Fig. 4.3). A positive relationship between RMSE$_{\partial\mathrm{SW}/\partial x}$ and the residuals is evident, supporting our hypothesis that models must simulate the interannual variability of SW CRE in a manner consistent with observations in order for our regression method to accurately predict their SW CRE feedbacks. Similar results are attained when only the partial derivatives of SW CRE with respect to SST, EIS, and RH_{700} – the three relationships weighted most heavily in the regression model for future climate change – are used to compute $\mathrm{RMSE}_{\partial \mathrm{SW}/\partial x}$. Note also that models with small $\mathrm{RMSE}_{\partial \mathrm{SW}/\partial x}$ are generally inferior in their simulation of the sensitivity of SW CRE to interannual variations in both SST and EIS (Fig. A4.1) and in many cases simulate individual relationships outside the range of observational uncertainty.

In Fig. 4.4 we show the predicted versus actual SW CRE feedback with models color coded according to two categories distinguishing their $\mathrm{RMSE}_{\partial \mathrm{SW}/\partial x}$. Green points denote models with the nine smallest $\mathrm{RMSE}_{\partial \mathrm{SW}/\partial x}$ values, while red points denote models with the nine largest $\mathrm{RMSE}_{\partial \mathrm{SW}/\partial x}$ values (excluding the model "P" with the largest $\mathrm{RMSE}_{\partial \mathrm{SW}/\partial x}$). Models with small $\mathrm{RMSE}_{\partial \mathrm{SW}/\partial x}$ simulate actual SW CRE feedbacks closer to the regression-derived feedbacks than models with larger $\mathrm{RMSE}_{\partial \mathrm{SW}/\partial x}$. In fact, the root mean square of the residuals of the realistic subset of models is half of that of the poorer performing subset. Additionally, the regression model is able to explain 61% of inter-model variability among the realistic models compared to 38% of variability among all models.

Further classifying models according to the $\mathrm{RMSE}_{\partial \mathrm{SW}/\partial x}$ metric, in Fig. 4.5 we plot the predicted versus actual SW CRE feedback with models color coded according to four categories distinguishing their $\mathrm{RMSE}_{\partial \mathrm{SW}/\partial x}$ values. The models with the four smallest $\mathrm{RMSE}_{\partial \mathrm{SW}/\partial x}$ values simulate actual feedbacks much closer to the feedbacks predicted via regression relative to models with the five largest $\mathrm{RMSE}_{\partial \mathrm{SW}/\partial x}$.

To corroborate our claim that models can be considered realistic or unrealistic according to the $\mathrm{RMSE}_{\partial \mathrm{SW}/\partial x}$ metric, we next evaluate vertical profiles of the mean annual cloud water content (CWC) in the control climate of the models with the four smallest $\mathrm{RMSE}_{\partial \mathrm{SW}/\partial x}$ and compare these to the profiles of the models with the five largest $\mathrm{RMSE}_{\partial \mathrm{SW}/\partial x}$. This is motivated by the findings of the preceding chapter, published in *Myers and Norris* (2015), in which we showed that the inter-model spread of the mean CWC can have large impacts on variability of SW CRE, since CWC is proportional to cloud optical thickness. CWC at each model level is defined as $(\rho_a m_t)/\mathrm{CF}$, where ρ_a is the density of dry air, m_t is the total (liquid plus ice) water mixing ratio in a grid box, and CF is cloud fraction. Dividing by CF allows us to examine the total water content within a cloud. The mean CWC profiles are shown in Fig. 4.6. Realistic models, according to the $\mathrm{RMSE}_{\partial \mathrm{SW}/\partial x}$ metric, simulate lower-tropospheric CWC maxima of around 0.25 g m^{-2} or less, close to the value of the ensemble mean of all 19 CMIP5 models. With one exception, poorer performing models simulate lower-tropospheric CWC maxima between 0.6 and 0.9 g m^{-2}. The profiles of these two subsets of models are therefore fundamentally different, justifying our classification of models according to their $\mathrm{RMSE}_{\partial \mathrm{SW}/\partial x}$.

Another reason why our regression technique may not perform well for certain models could be that that there are SW CRE feedbacks in some models driven by changes in mid- or high-level clouds. The predictor variables in the regression model were chosen as the set of external parameters controlling subtropical MBL cloudiness, so we do not expect the model to capture changes in SW CRE associated with higher-level clouds.

To explore this hypothesis, we compute subtropical mean SW cloud feedbacks in models providing ISCCP simulator output and compare these to the SW feedbacks due only to changes in low-level clouds. SW cloud feedbacks are computed using the radiative kernel method of *Zelinka et al.* (2012) (see the previous chapter for a discussion of kernels and the ISCCP simulator). We define low clouds as those with tops below the 560 hPa level since the retrieval algorithm of ISCCP, and hence likely the simulator, often places true low-level clouds in the mid-level category in regions where strong inversions and overlying cirrus occur (*Mace et al.*, 2006; *Garay et al.*, 2008). The results are displayed in Fig. 4.7. While the spread of the SW cloud feedback shown in Fig. 4.7 is largely driven by changes in low clouds, two out of six models ("D" and "Q") simulate substantial negative feedbacks induced by trends in higher-level clouds, manifested as the residuals from the one-to-one line.

In Fig. 4.8 we illustrate that when the negative high cloud feedbacks in "D" and "Q" are subtracted from their simulated SW CRE feedbacks, the resulting low cloud feedbacks more closely align with the SW CRE changes estimated via regression. Note that models "D" and "Q" are within the subset of models with the nine smallest $\mathrm{RMSE}_{\partial \mathrm{SW}/\partial x}$ values. This suggests that for the models realistically producing interannual SW CRE variability, the SW CRE change predicted using our regression technique is truly capturing low cloud feedbacks.

4.2.3 Decomposition of feedbacks

Now that we are able to reasonably predict SW CRE feedbacks in nine models in the CMIP5 ensemble, we can ask, What drives the inter-model spread in this subset of models? To answer this question, we decompose each spatially averaged partial derivative $\left\langle \partial \mathrm{SW}/\partial x_i \right\rangle$ and meteorological trend $\left\langle dx_i/dT \right\rangle$ into a multi-model mean plus an anomaly from the multi-model mean. Then Eq. 4.4 can be written as

$$\frac{d\mathrm{SW}}{dT} = \sum_{i=1}^{5} \left[\frac{\partial \mathrm{SW}}{\partial x_i}\right]\left[\frac{dx_i}{dT}\right] + \frac{\partial \mathrm{SW}'}{\partial x_i}\left[\frac{dx_i}{dT}\right] + \left[\frac{\partial \mathrm{SW}}{\partial x_i}\right]\frac{{dx_i}'}{dT} + \left[\frac{\partial \mathrm{SW}'}{\partial x_i}\frac{{dx_i}'}{dT}\right]. \tag{4.13}$$

Bracketed quantities are multi-model means, primes denote anomalies of adjacent quantities, and the spatial average operator $\left\langle ... \right\rangle$ is omitted for conciseness. The first term on the right-hand side of Eq. 4.13 is the part of the SW CRE feedback common to all models. The second term is the part of the feedback due to interannual cloud/meteorology relationships different from those of the ensemble mean. The third term is the part of the feedback due to trends in meteorological variables different from those of the ensemble mean. The fourth term is a covariance factor, which is found to be small.

In Fig. 4.9 we plot the part of the SW CRE feedback common to all models plus $\partial \mathrm{SW}/\partial x_i'\left[dx_i/dT\right]$ (top left) and $\partial \mathrm{SW}/\partial x_i'\left[dx_i/dT\right] + \left[\partial \mathrm{SW}/\partial x_i\right] dx_i/dT'$ (top right) separately versus the actual SW CRE feedbacks in all CMIP5 models. We also plot the SST component of the predicted feedback decomposed in a similar manner versus the actual SW CRE feedback. Models are color coded into the two categories distinguishing their $\mathrm{RMSE}_{\partial \mathrm{SW}/\partial x}$ values, as done in Fig. 4.4. The top two subplots of Fig. 4.9 reveal that differences in partial derivatives among models contribute most to the spread of SW CRE feedbacks in both the realistic and poorer performing subset of models. Note, however, that the root mean square of the residuals is smaller among the former set of models.

The bottom two subplots of Fig. 4.9 show that differences in the sensitivity of SW CRE to interannual fluctuations in SST in the control climate are key to generating the spread of SW CRE feedbacks among models. As expected, not accounting for the EIS and RH_{700} components of the feedback increases the root mean square of the residuals compared to if they are included in the regression model. The interannual SW CRE/SST relationship on its own can explain nearly 50% of the inter-model spread in the SW CRE feedback in both the realistic and poorer performing subsets of models (bottom left of Fig. 4.9). Since observations can provide an estimate of this sensitivity as well as the sensitivity of SW CRE to interannual fluctuations in EIS and RH_{700} (Fig. 4.1), these results strongly indicate that realistic bounds of the true SW CRE feedback can be attained.

4.2.4 Observational constraint on the SW CRE feedback

Using multi-model mean values for each of the spatially averaged climate change perturbations in the meteorological variables $\left\langle dx_i/dT\right\rangle$ and observational estimates for each of the five interannual SW CRE sensitivity values $\left\langle \partial\mathrm{SW}/\partial x_i\right\rangle$, we approximate the true subtropical mean SW CRE feedback $\left\langle d\mathrm{SW}/dT\right\rangle$ using Eq. 4.4. By defining Δ_i as the observational uncertainty of $\left\langle \partial\mathrm{SW}/\partial x_i\right\rangle$ (Eq. 4.11) and propagating the error, we compute a 90% confidence interval for the true SW CRE feedback as

$$\left\langle \frac{d\mathrm{SW}}{dT}\right\rangle \pm \sqrt{\sum_{i=1}^{5} \Delta_i^2 \left\langle \frac{dx_i}{dT}\right\rangle^2}. \tag{4.14}$$

The observational estimate of the SW CRE feedback and its uncertainty and largest components are displayed in Fig. 4.10. Overall, the feedback is positive and nearly statistically significant at the 90% confidence level ($p = 0.13$). A positive feedback of 2 W m^{-2} K^{-1} arises as a result of the increase in SST projected by the ensemble

(Fig. 4.1), while a negative feedback of around -1 W m^{-2} K^{-1} arises as a result of the increase in EIS and RH$_{700}$. This yields a total feedback of 1 W m^{-2} K^{-1} with a 90% confidence interval extending from around 0 W m^{-2} K^{-1} to 2 W m^{-2} K^{-1}. This observationally constrained range of the subtropical SW CRE feedback is around half of the range of SW CRE feedbacks produced by the CMIP5 ensemble (Fig. 4.1).

Much of the spread of equilibrium climate sensitivity (ECS, the global mean equilibrium temperature response due to a doubling of CO$_2$) in the CMIP5 ensemble is explained by changes in SW CRE over the subtropical oceans (*Vial et al.*, 2013; *Myers and Norris*, 2015). We can therefore place an observational constraint on ECS using our observational estimate of the subtropical SW CRE feedback. To do this, in Fig. 4.11 we plot the actual SW CRE feedback against ECS for the nine models most realistically simulating the observed interannual variability of SW CRE (using our RMSE$_{\partial \mathrm{SW} \partial x}$ metric) and with reported ECS values taken from *Stocker et al.* (2014). Note that the SW CRE feedback and ECS in these models is highly correlated (r=0.8), pointing to the importance of the "slow" response of subtropical clouds to anthropogenic forcing. Also shown are standard error bounds and a 90% confidence interval for our observational estimate of the SW CRE feedback. The only two models, "H" and "Q", with feedbacks falling within the standard error bounds have ECS values of 3.6 K and 4 K, respectively. Models with feedbacks below (above) this range generally have lower (higher) ECS. In fact, three out of four models with SW CRE feedbacks of more than one standard error below the observational feedback estimate have ECS values between 2.1 K and 2.7 K. The 90% confidence range of the observationally constrained feedback, however, includes model "O" with an ECS of 2.7 K. Constraining the subtropical SW CRE feedback in a more statistically robust manner will require reducing the observational uncertainty of relationships between SW CRE and cloud controlling factors. But the fact that four out of the five models residing within the 90% confidence range of observations have ECS values between 3.6 K and 4.6 K is very suggestive evidence that the true climate sensitivity is on the high end of estimates currently produced by climate models.

Figure 4.11 additionally shows the SW CRE feedback versus ECS for all models with reported ECS values. Here, the two variables are also correlated (r=0.72), and the range of uncertainty of the observationally constrained feedback points to a high climate sensitivity but with a lesser degree of confidence than indicated by the left subplot of Fig. 4.11. This highlights the importance of the simulation of interannual variability in climate models. Models "P" and "R" reside within one standard error of our SW CRE feedback estimate but have ECS on the highest and low ends of estimates produced by the ensemble, respectively. These models, however, are among the five worst with respect to simulating interannual relationships between SW CRE and cloud-controlling factors (Fig. 4.3), and they both simulate $\langle \partial \mathrm{SW}/\partial \mathrm{SST} \rangle$ and $\langle \partial \mathrm{SW}/\partial \mathrm{EIS} \rangle$ outside the range observational uncertainty (Fig. A4.1). On this basis we argue that their SW CRE feedbacks, and by extension their climate sensitivities, are not to be trusted.

4.3 Summary and Discussion

In this study, we employ multi-linear regression analysis to explain the subtropical mean SW CRE feedbacks produced by 19 CMIP5 models in an idealized experiment in which CO_2 concentration is instantaneously quadrupled relative to preindustrial levels. Departing from previous studies examining changes in boundary layer clouds over the subtropical oceans, we restrict our analysis to a study of the "slow" cloud feedback, defined as the change in SW CRE mediated by the increase in global mean temperature over the first 140 years of the climate change run. The regression model, constructed from each CMIP5 model's control climate, produces the interannual sensitivity of SW CRE to independent variations in five external forcing parameters for each grid box over the tropical (30°N–30°S) oceans experiencing climatological subsidence. These parameters include SST, EIS, SSTadv, RH_{700}, and ω_{700}. Multiplying each of these partial derivatives by the grid-box trends in each parameter per unit of global warming, summing all components, and then spatially averaging results in an estimate of the subtropical SW CRE feedback for each model.

This diagnostic technique is able to explain the (positive) sign of the ensemble mean subtropical SW CRE feedback and a modest amount of its spread. The three most dominant variables in determining the SW CRE feedback are SST, EIS, and RH_{700}. This is mainly because in the $4\mathrm{xCO}_2$ experiments examined here, the CMIP5 ensemble predicts strong increases in these parameters relative to future changes in ω_{700} and SSTadv. For the ensemble mean and most models, a strong positive feedback due to warmer SST is larger in magnitude than the negative feedback resulting from stronger EIS and higher RH_{700}. The SST component of the regression model, $\left\langle \partial \mathrm{SW}/\partial \mathrm{SST} \times d\mathrm{SST}/dT \right\rangle$, explains 52% the inter-model variability of the SW CRE feedback in 18 models of the CMIP5 ensemble.

The ability of our regression technique to predict the SW CRE feedback in a given model depends on how well that model simulates the sensitivity of SW CRE to interannual variations in the five forcing parameters and whether or not the model simulates substantial high cloud feedbacks. Among the nine models most closely resembling observations, the root mean square of the difference between the actual and regression-predicted SW CRE feedbacks is half of that of the poorer-performing models. For this subset of models, 50% of inter-model variance of the feedback is explained by the interannual sensitivity of SW CRE to fluctuations in SST, $\left\langle \partial \mathrm{SW}/\partial \mathrm{SST} \right\rangle$. This strongly indicates that observational relationships between SW CRE and cloud-controlling factors can be used to constrain the cloud feedback.

Our observational estimate of the feedback is computed by multiplying the observed interannual sensitivity of SW CRE to independent variations in each of the five cloud-controlling factors by the appropriate multi-model mean climate change perturbations in these external factors and summing the resulting components. Using two independent cloud datasets (CERES and ISCCP) and four atmospheric reanalyses (CFSR, ERA-Interim, MERRA, and JRA-55) enables us to robustly capture the range of uncertainty of this estimate. This observationally constrained estimate suggests that a positive SW CRE feedback arising from the increase in SST will likely dominate over a negative feedback arising from the increase in both EIS and RH_{700}. Of the subset of models most realistically producing interannual variability of SW CRE, four out of the five models that simulate SW CRE feedbacks within the 90% confidence interval of our observational estimate produce ECS values between 3.6 K and 4.6 K. This corroborates several recent studies that have found that climate models most closely resembling some observational metric describing cloud processes have strong positive cloud feedbacks and high climate sensitivities (*Fasullo and Trenberth*, 2012; *Klein et al.*, 2013; *Sherwood et al.*, 2014; *Su et al.*, 2014; *Myers and Norris*, 2015).

While several studies have used observations to argue how subtropical MBL clouds will respond to and feed back on anthropogenic warming (*Miller*, 1997; *Clement et al.*, 2009; *Myers and Norris*, 2013; *Qu et al.*, 2013), ours is the first to do so in such a quantitative and systematic fashion. Why SW CRE over subtropical subsidence regions becomes more positive as SST warms is still an open question. A leading hypothesis proposed by recent modeling studies (*Brient and Bony*, 2013; *Bretherton et al.*, 2013) is based on the response of low clouds to the increase in the absolute moisture difference between the MBL and the drier free troposphere in the future climate that will occur for vertically uniform warming and unchanged relative humidity, based on Clausius-Clapeyron scaling. This enhanced moisture gradient increases entrainment drying of the MBL, reducing cloud cover. From an energetic standpoint, the enhanced moisture gradient results in an increase of the transport of air with low moist static energy by large-scale subsidence into the MBL. This is balanced in turn by a decrease in the radiative cooling by clouds within the MBL, reducing cloud cover. One issue with these arguments is that they assume that the relative humidity remains constant in a global warming scenario, whereas in the CMIP5 4xCO_2 simulations examined here free-tropospheric relative humidity increases non-negligibly. This increase in relative humidity implies less of an increase in the absolute moisture difference between the MBL and free troposphere than would occur if relative humidity were to remain fixed. In fact, we find that increasing relative humidity at 700 hPa will likely lead to a negative subtropical SW CRE feedback and partially act to oppose the positive feedback arising from an increase in SST.

Regardless of the physical mechanisms at play, the results of the present study reveal that an understanding of how and why subtropical MBL clouds vary on an interannual basis is likely sufficient to explain the cloud response to climate change. Our work may provide a framework with which to reduce uncertainty in MBL cloud feedbacks and climate sensitivity. Developers of cloud parameterizations can use the observational cloud/meteorology sensitivity estimates computed here as a benchmark for model performance. If the inter-model spread of interannual relationships between subtropical SW CRE and large-scale meteorological factors is reduced, it is likely that the spread of the subtropical cloud feedback and climate sensitivity will similarly be narrowed.

Tables and Figures

Table 4.1: CMIP5 models used in the investigation. The ID column lists letters used to identify models in the text and figures.

Modeling Group	**CMIP5 Models**	**ID**
Commonwealth Scientific and Industrial Research Organization (CSIRO) and Bureau of Meteorology (BOM), Australia	ACCESS1.0 ACCESS1.3	A B
Beijing Climate Center, China Meteorological Administration	BCC-CSM1.1	C
Canadian Centre for Climate Modelling and Analysis	CanESM2	D
National Center for Atmospheric Research	CCSM4	E
Commonwealth Scientific and Industrial Research Organization in collaboration with Queensland Climate Change Centre of Excellence	CSIRO-Mk3.6.0	F
LASG, Institute of Atmospheric Physics, Chinese Academy of Sciences and CESS, Tsinghua University	FGOALS-g2	G
NOAA Geophysical Fluid Dynamics Laboratory	GFDL-CM3 GFDL-ESM2G	H I
NASA Goddard Institute for Space Studies	GISS-E2-H	J
Met Office Hadley Centre	HadGEM2-ES	K
Institute for Numerical Mathematics	INM-CM4	L
Institut-Pierre Simon Laplace	ISPL-CM5A-LR IPSL-CM5B-LR	M N
Japan Agency for Marine-Earth Science and Technology, Atmosphere and Ocean Research Institute (The University of Tokyo), and National Institute for Environmental Studies	MIROC5 MIROC-ESM	O P
Max Plank Institute for Meteorology	MPI-ESM-LR	Q
Meteorological Research Institute	MRI-CGCM3	R
Norwegian Climate Centre	NorESM1-M	S

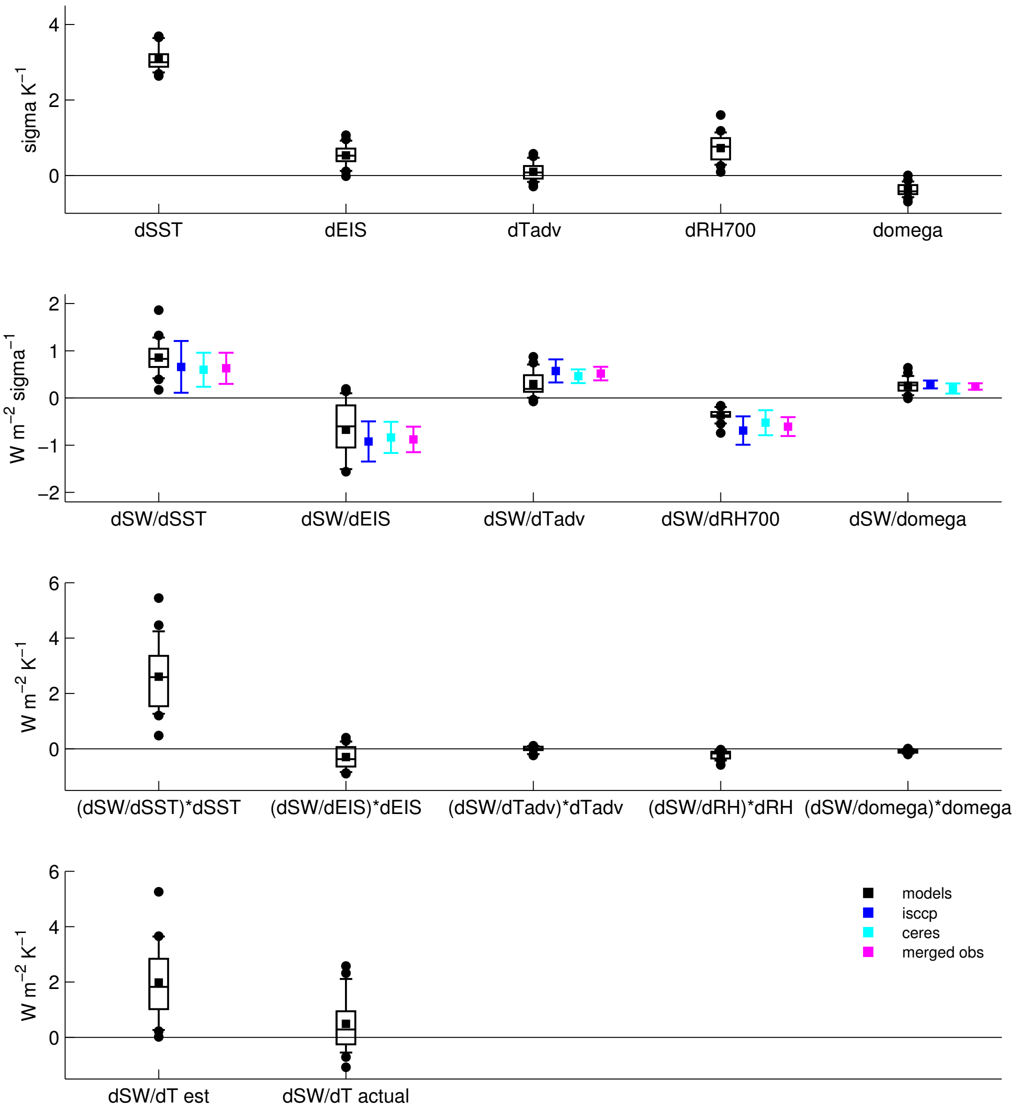

Figure 4.1: (top) Changes in subtropical mean meteorological variables in CMIP5 models per unit increase in global mean temperature, (second from top), subtropical mean sensitivity of SW CRE to interannual variations in meteorological parameters estimated using multi-linear regression in models and observations, (second from bottom) subtropical mean components of the estimated SW CRE feedback in the CMIP5 ensemble, and (bottom) estimated and actual subtropical mean SW CRE feedback in the CMIP5 ensemble. For CMIP5 quantities, the square denotes the multi-model mean, the horizontal line denotes the median of all modeled values, the box spans the interquartile range of all modeled values, the whiskers extend to the 10th and 90th percentiles of all modeled values, and the circles are the modeled values outside the 10th and 90th percentiles. For each observed relationship, the error bars span the 90% confidence range for ISCCP (blue), CERES (cyan), and merged observations (magenta) as described in the text.

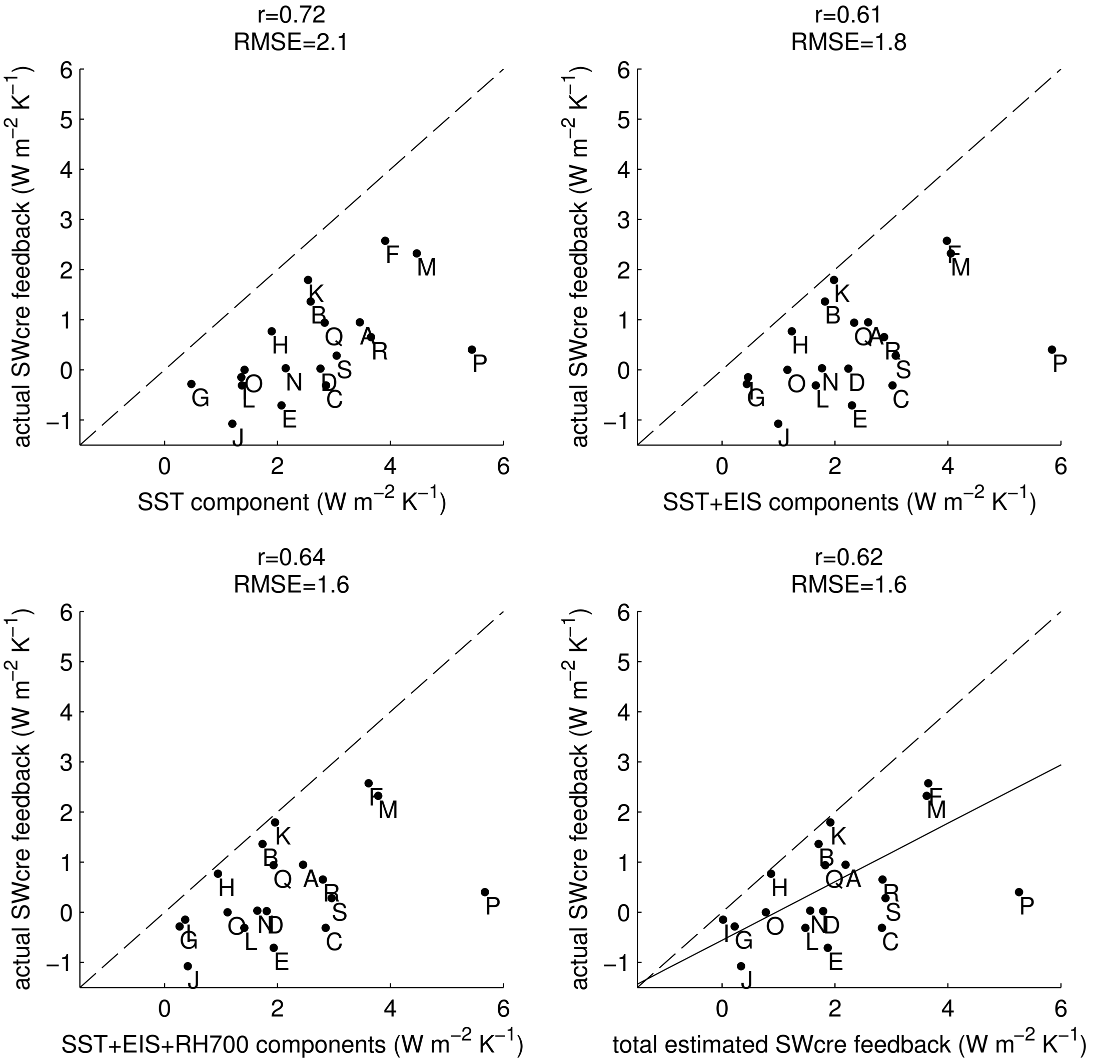

Figure 4.2: Components of the SW CRE feedback predicted using regression plotted against the actual SW CRE feedback in CMIP5 models. The SST component is defined as $\langle \partial \mathrm{SW}/\partial \mathrm{SST} \times d\mathrm{SST}/dT \rangle$. The EIS and RH700 components are defined similarly. Letters stand for individual models, defined in Table 4.1. Each dashed line is a theoretical perfect fit, and the solid line in the bottom right subplot shows a best fit using least squares linear regression excluding the outlier model "P". At the top of each subplot, a Pearson correlation coefficient (r) and the root mean square of the residuals (RMSE, in W m^{-2}K^{-1}) are listed.

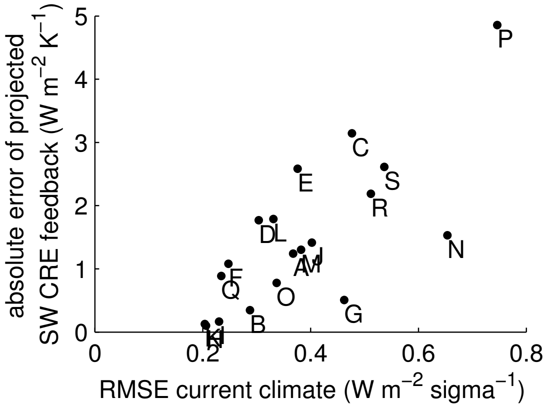

Figure 4.3: Root-mean-square error of the five subtropical mean SW CRE sensitivity estimates relative to observations plotted against the absolute value of the difference between actual SW CRE feedback and the feedback predicted via regression in CMIP5 models.

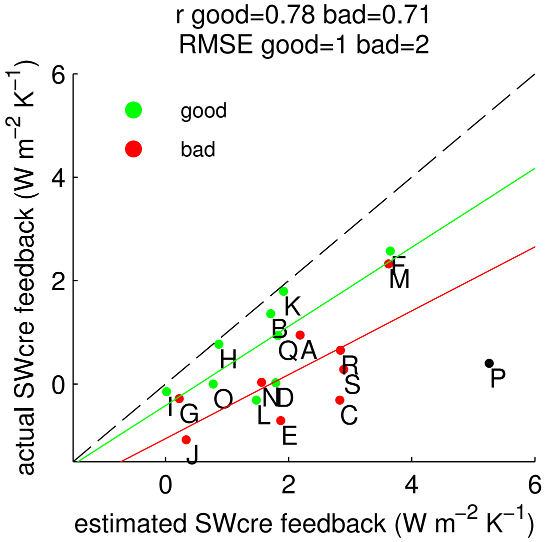

Figure 4.4: The SW CRE feedback predicted using regression plotted against the actual SW CRE feedback in CMIP5 models. Green points denote models with the nine smallest values of $\mathrm{RMSE}_{\partial \mathrm{SW}/\partial x}$ (good models). Red points denote models with the nine largest values of $\mathrm{RMSE}_{\partial \mathrm{SW}/\partial x}$ (bad models), excluding the outlier model "P". The dashed line is a theoretical perfect fit, while the green and red lines show best fits using least squares linear regression for good and bad models, respectively. At the top of the plot, correlation coefficients and the root mean square of the residuals (in W m^{-2}K^{-1}) are listed separately for good and bad models.

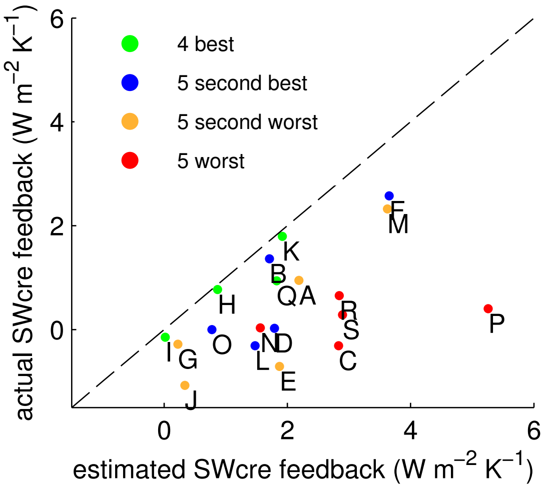

Figure 4.5: The SW CRE feedback predicted using regression plotted against the actual SW CRE feedback in CMIP5 models. Green points denote models with the four smallest values of RMSE$_{\partial \mathrm{SW}/\partial x}$ (four best models). Blue points denote models with the next five smallest values of RMSE$_{\partial \mathrm{SW}/\partial x}$ (five second best models). Red points denote models with the five largest values of RMSE$_{\partial \mathrm{SW}/\partial x}$ (five worst models). Orange points denote models with the next five largest values of RMSE$_{\partial \mathrm{SW}/\partial x}$ (five second worst models). The dashed line is a theoretical perfect fit.

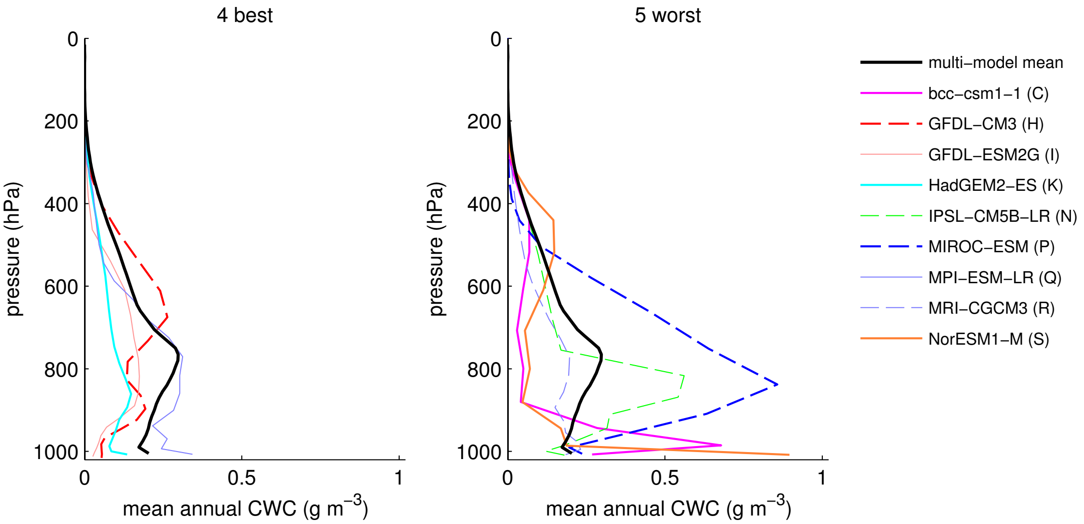

Figure 4.6: Mean annual cloud water content as a function of pressure in models with the (left) four smallest values of RMSE$_{\partial \mathrm{SW}/\partial x}$ and (right) five largest values of RMSE$_{\partial \mathrm{SW}/\partial x}$.

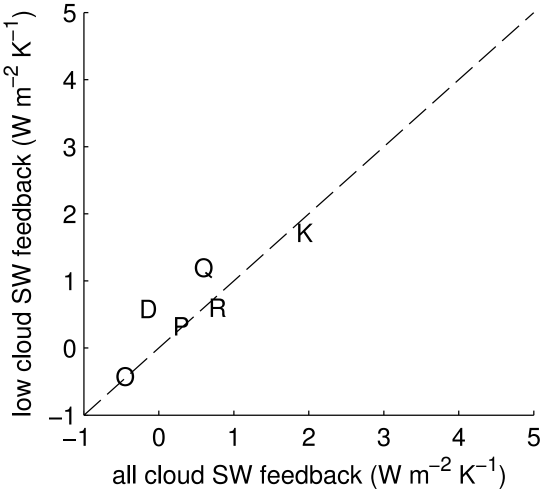

Figure 4.7: SW cloud feedback due to changes in all clouds plotted against the SW cloud feedback due to changes in low clouds, computed using the radiative kernel method of *Zelinka et al.* (2012). The dashed line is a theoretical perfect fit. Note that residuals from the dashed line indicate SW cloud feedbacks due to changes in high clouds.

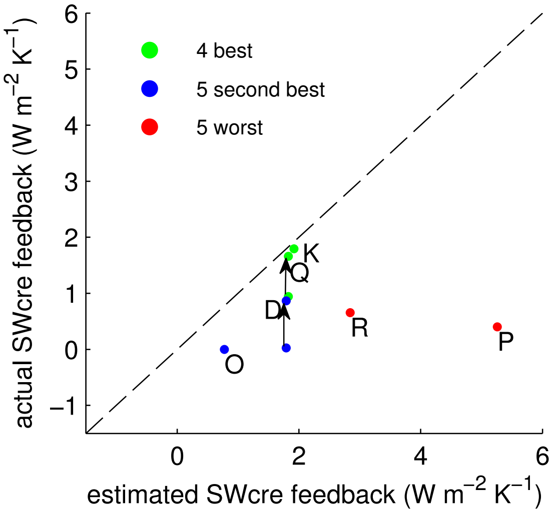

Figure 4.8: The SW CRE feedback predicted using regression plotted against the actual SW CRE feedback in CMIP5 models employing the ISCCP simulator. The arrows extend from models' "D" and "Q" actual SW CRE feedbacks to the part of their SW CRE feedbacks due only to changes in low clouds. The dashed line is a theoretical perfect fit.

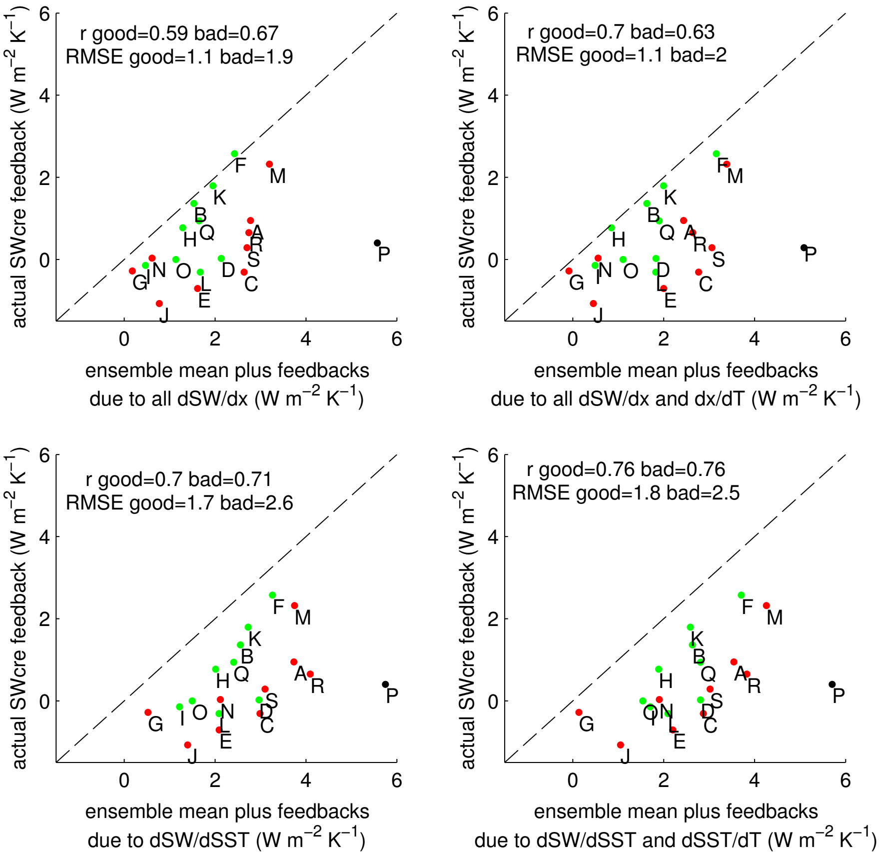

Figure 4.9: Decomposed SW CRE feedback predicted using regression plotted against the actual SW CRE feedback in CMIP5 models. The horizontal axis of the top left subplot represents the part of the predicted SW CRE feedback common to all models plus the part of the feedback due to interannual cloud/meteorology relationships different from those of the ensemble mean. The horizontal axis of the top right subplot represents the part of the predicted SW CRE feedback common to all models plus both the part of the feedback due to interannual cloud/meteorology relationships different from those of the ensemble mean and the part of the feedback due to trends in meteorological variables different from those of the ensemble mean. The horizontal axes of the bottom subplots are defined similarly but just for the SST component of the SW CRE feedback. See text for details. Points are color coded according to models' RMSE$_{\partial \mathrm{SW}/\partial x}$ values, as in Fig. 4.4. Each dashed line is a theoretical perfect fit. At the top of each subplot, a correlation coefficient and the root mean square of the residuals (in W m^{-2}K^{-1}) are listed separately for good and bad models.

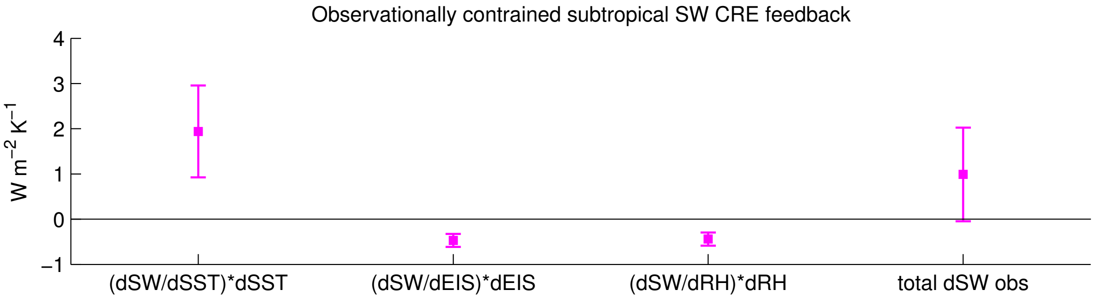

Figure 4.10: Components of the observational estimate of the subtropical SW CRE feedback, with error bars showing 90% confidence intervals. Estimates are formed by multiplying observed subtropical mean partial derivatives with multi-model mean meteorological trends, described in detail in the text.

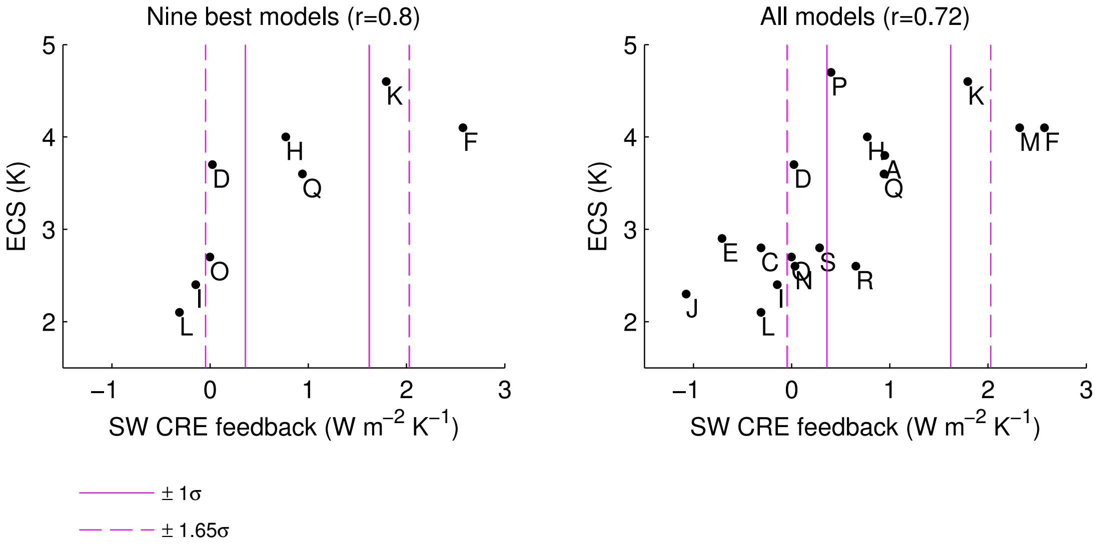

Figure 4.11: Subtropical mean SW CRE feedback plotted against ECS in (left) CMIP5 models with the nine smallest values of RMSE$_{\partial \mathrm{SW}/\partial x}$ and with reported ECS and (right) in all CMIP5 models with reported ECS. Solid (dashed) vertical lines horizontally span the standard error (90% confidence) bounds of the observational estimate of the SW CRE feedback.

Appendix

Meteorological covariability

The reader may question how covariability (or multi-collinearity) among the predictor variables (SST, EIS, SSTadv, RH_{700}, ω_{700}) in the present study affects the results. Multi-collinearity increases the uncertainty of the observed regression coefficients (Fig. 4.1, *O'brien*, 2007). Second, the model and observational estimates of the subtropical SW CRE feedback are not affected by multi-collinearity. Third, the variance inflation factor of the standard error for each observed coefficient is within the range considered by many statisticians not to indicate a multi-collinearity issue (*O'brien*, 2007). We conclude that multi-collinearity does affect any of our conclusions. For completeness, it is worth noting the degree of correlation among predictor variables. For each grid box we computed correlation coefficients among the time series of 1984-2012 interannual anomalies of the five cloud-controlling meteorological parameters examined in the study. The domain averages of these coefficients are shown in Table A4.1. The largest correlations are between SST and EIS ($r = 0.52$) and between RH_{700} and EIS ($r = 0.5$), both of which make physical sense given the definition of EIS.

Contributions to SW CRE feedbacks in individual models

To further support and elaborate on our methodology for grouping models into realistic and unrealistic subsets, in Fig. A4.1 we show subtropical mean partial derivatives of SW CRE with respect to each of the five external forcing parameters for observations and individual models color coded into four categories according to their values of $\mathrm{RMSE}_{\partial \mathrm{SW}/\partial x}$. Models with small $\mathrm{RMSE}_{\partial \mathrm{SW}/\partial x}$ generally are superior in their simulation of the interannual sensitivity of SW CRE to variations in both SST and EIS compared to models with relatively large $\mathrm{RMSE}_{\partial \mathrm{SW}/\partial x}$. The distinction is especially evident between the four best and five worst models according to this metric, with several models in the latter subset clearly outside the range of observational uncertainty of $\langle \partial \mathrm{SW}/\partial \mathrm{SST} \rangle$ or $\langle \partial \mathrm{SW}/\partial \mathrm{EIS} \rangle$.

Table A4.1: Spatially averaged correlation coefficients among the observed variables.

	SST	**EIS**	**SSTadv**	**RH$_{700}$**	**ω_{700}**
SST	1	-0.52	0.28	0.22	-0.19
EIS	-0.52	1	-0.14	-0.5	0.14
SSTadv	0.28	-0.14	1	0.2	-0.29
RH$_{700}$	0.22	-0.5	0.2	1	-0.43
ω_{700}	-0.19	0.14	-0.29	-0.43	1

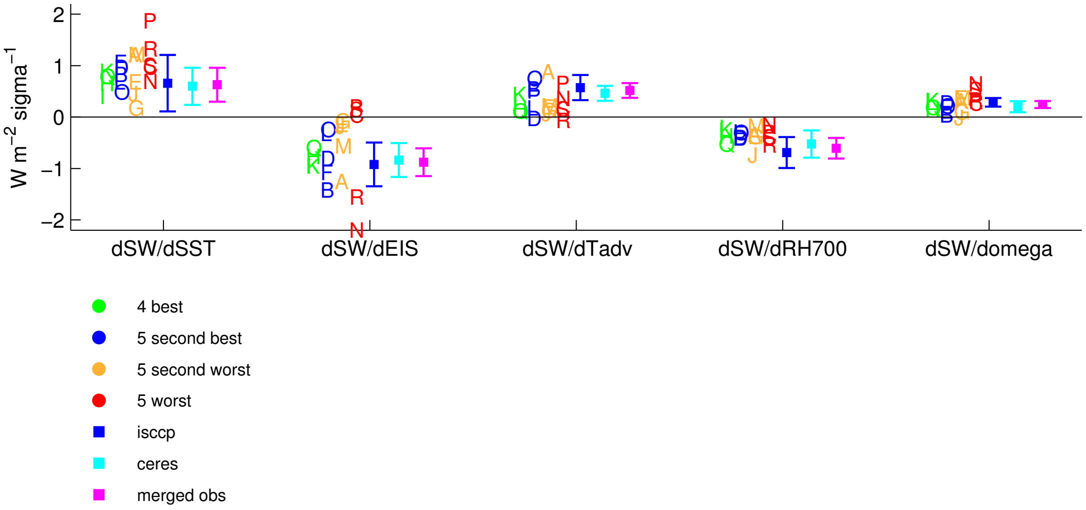

Figure A4.1: Subtropical mean sensitivity of SW CRE to interannual variations in meteorological parameters estimated using multi-linear regression in individual models and observations. Models are color coded according to their $\mathrm{RMSE}_{\partial \mathrm{SW}/\partial x}$ values as done in Fig. 4.5. For each observed relationship, the error bars span the 90% confidence range for ISCCP (blue), CERES (cyan), and merged observations (magenta) as described in the text.

Chapter 5

Conclusions

This thesis has aimed to increase the scientific understanding of subtropical marine boundary layer (MBL) clouds, which are poorly simulated by climate models and lead to large uncertainty of global warming projections. The main methodology employed throughout all chapters was the computation and interpretation of statistical relationships between boundary layer cloud properties and the variables describing their large-scale meteorological environment. These relationships serve as proxies for MBL cloud processes that occur on spatial scales too small to directly measure or to represent explicitly in climate models.

In Chapter 2, we showed, by dint of careful assessment of observations and theoretical reasoning, how large-scale subsidence affects MBL properties over the eastern subtropical oceans. In short, enhanced subsidence directly pushes down cloud top, reducing cloud thickness, whereas weaker subsidence allows cloud top to rise, increasing cloud thickness. Until now, this finding has proved elusive to observational studies because, climatologically, enhanced subsidence favors a stronger temperature inversion capping the MBL, which itself promotes MBL cloudiness. We sidestepped this confounding effect using a novel statistical technique to infer the relationship between subsidence MBL cloudiness for a fixed value of inversion strength. This approach is by no means exclusive to investigating MBL cloud processes or even just to climate science generally. Indeed, our methods can be used by other fields of research to disentangle the effects of different predictor variables on a dependent variable of interest, especially if the predictor variables covary.

In Chapter 3, we performed a thorough evaluation of model simulation of subtropical cloud processes on time scales of one month or greater. We found that both the latest generation of climate models (CMIP5) and the previous generation (CMIP3) are deficient in their simulation of the interannual relationship between shortwave cloud radiative effect and horizontal surface temperature advection. We discovered that CMIP5 is inferior to CMIP3 in producing the interannual relationship between shortwave cloud radiative effect and both sea surface temperature (SST) and the strength of the temperature inversion capping the MBL. While this may seem like a surprising result, it is important to recognize that CMIP5 models employ more physically realistic cloud parameterization schemes compared to CMIP3. It is likely that such schemes generate more degrees of freedom in their representation of MBL cloud processes than in CMIP3, allowing for a wider variety of cloud/meteorology relationships produced. Future studies can address this hypothesis.

But what makes a good model? One could argue that a model that realistically simulates the observed climate is a superior model to one that does a worse job at simulating observations but is more physically realistic. One could just as easily argue the opposite. Determining what makes a good model depends on how one wants to use the model in the first place (e.g numerical experimentation, decadal prediction, seasonal forecasting, etc.). Unfortunately, for global warming projections, only time will tell which models will have accurately predicted the climate response to anthropogenic forcing. Until then, we think it is crucial for models to simulate relationships between subtropical clouds and large-scale meteorological factors with some degree of fidelity if they are to be trusted in their global warming projections.

The large inter-model spread of the sensitivity of subtropical shortwave cloud radiative effect (SW CRE) to fluctuations in large-scale meteorological factors produced by climate models suggests why low-level cloud feedbacks to global warming are so uncertain. Chapter 4 is dedicated to more quantitatively and rigorously testing this hypothesis. In that chapter, we used a diagnostic technique to determine the mechanisms leading to the variety of subtropical SW CRE feedbacks projected by 19 CMIP5 models in an idealized instantaneous quadrupling of CO_2 experiment. After eliminating the models most poorly representing interannual relationships between SW CRE and cloud-controlling factors, the ensemble still produces a wide inter-model spread of the SW CRE feedback. Among these more realistic models, using multi-linear regression we find that the inter-annual sensitivity of SW CRE to variations in SST explains roughly 50% of the inter-model variance of the SW CRE feedback. All models simulate more positive SW CRE (i.e. less solar radiation reflected to space) when SST is anomalously warm on an inter-annual timescale. SST warms a lot relative to changes in other cloud controlling factors in the future climate, so models that produce a large magnitude of this sensitivity project more positive SW CRE feedbacks than models that produce a weaker sensitivity. An observational estimate of this sensitivity implies a positive SW CRE feedback to global warming, partially offset by a negative feedback due to an increase of both inversion strength and free-tropospheric relative humidity in the future climate. Our observational estimate also suggests that a high climate sensitivity is more probable than a low one, in line with results of several recent model evaluation studies (*Fasullo and Trenberth*, 2012; *Klein et al.*, 2013; *Sherwood et al.*, 2014; *Su et al.*, 2014; *Myers and Norris*, 2015).

The results of Chapter 4 show that an understanding of the mechanisms governing interannual variability of subtropical MBL clouds may be sufficient to understand the cloud response to climate change. Though we did not address why warmer SST on an interannual basis leads to less solar reflection by MBL clouds, recent modeling studies propose that vertically uniform warming leads to more entrainment drying and an increase in the import of air with low moist static energy into the MBL, thereby reducing cloudiness (*Bretherton et al.*, 2013; *Brient and Bony*, 2013). Future observational studies can apply the compositing techniques of Chapter 2 to explore whether these mechanisms operate in the real atmosphere.

Chapter 6

Bibliography

Albrecht, B. A., Jensen, M. P., and Syrett, W. J. (1995). Marine boundary layer structure and fractional cloudiness. *Journal of Geophysical Research: Atmospheres (1984–2012)*, 100(D7):14209–14222.

Andrews, T., Gregory, J., Forster, P., and Webb, M. (2012a). Cloud adjustment and its role in CO2 radiative forcing and climate sensitivity: A review. *Surveys in geophysics*, 33(3-4):619–635.

Andrews, T., Gregory, J. M., Webb, M. J., and Taylor, K. E. (2012b). Forcing, feedbacks and climate sensitivity in CMIP5 coupled atmosphere-ocean climate models. *Geophysical Research Letters*, 39(9):n/a–n/a.

Betts, A. K. and Ridgway, W. (1989). Climatic equilibrium of the atmospheric convective boundary layer over a tropical ocean. *Journal of the Atmospheric Sciences*, 46(17):2621–2641.

Blossey, P. N., Bretherton, C. S., Zhang, M., Cheng, A., Endo, S., Heus, T., Liu, Y., Lock, A. P., Roode, S. R., and Xu, K.-M. (2013). Marine low cloud sensitivity to an idealized climate change: The cgils les intercomparison. *Journal of Advances in Modeling Earth Systems*, 5(2):234–258.

Bodas-Salcedo, A., Webb, M., Bony, S., Chepfer, H., Dufresne, J.-L., Klein, S., Zhang, Y., Marchand, R., Haynes, J., Pincus, R., et al. (2011). Cosp: Satellite simulation software for model assessment. *Bulletin of the American Meteorological Society*, 92(8):1023–1043.

Bony, S. and Dufresne, J. (2005). Marine boundary layer clouds at the heart of tropical cloud feedback uncertainties in climate models. *Geophysical Research Letters*, 32(20):L20806.

Bony, S., Dufresne, J.-L., Le Treut, H., Morcrette, J.-J., and Senior, C. (2004). On dynamic and thermodynamic components of cloud changes. *Climate Dynamics*, 22(2-3):71–86.

Bretherton, C. S. and Blossey, P. N. (2013). Low cloud reduction in a greenhouse-warmed climate : Results from Lagrangian LES of a subtropical marine cloudiness transition . (July):1–61.

Bretherton, C. S., Blossey, P. N., and Jones, C. R. (2013). Mechanisms of marine low cloud sensitivity to idealized climate perturbations: A single-les exploration extending the cgils cases. *Journal of Advances in Modeling Earth Systems*, 5(2):316–337.

Bretherton, C. S. and Wyant, M. C. (1997). Moisture transport, lower-tropospheric stability, and decoupling of cloud-topped boundary layers. *Journal of the atmospheric sciences*, 54(1):148–167.

Brient, F. and Bony, S. (2013). Interpretation of the positive low-cloud feedback predicted by a climate model under global warming. *Climate Dynamics*, 40(9-10):2415–2431.

Broccoli, A. J. and Klein, S. a. (2010). Comment on "Observational and model evidence for positive low-level cloud feedback". *Science (New York, N.Y.)*, 329(5989):277; author reply 277.

Caldwell, P. M., Zhang, Y., and Klein, S. a. (2013). CMIP3 Subtropical Stratocumulus Cloud Feedback Interpreted through a Mixed-Layer Model. *Journal of Climate*, 26(5):1607–1625.

Charney, J. G., Arakawa, A., Baker, D. J., Bolin, B., Dickinson, R. E., Goody, R. M., Leith, C. E., Stommel, H. M., and Wunsch, C. I. (1979). Carbon dioxide and climate: a scientific assessment.

Chepfer, H., Bony, S., Winker, D., Cesana, G., Dufresne, J., Minnis, P., Stubenrauch, C., and Zeng, S. (2010). The gcm-oriented calipso cloud product (calipso-goccp). *Journal of Geophysical Research: Atmospheres (1984–2012)*, 115(D4).

Christensen, M. W., Carrió, G. G., Stephens, G. L., and Cotton, W. R. (2013). Radiative Impacts of Free-Tropospheric Clouds on the Properties of Marine Stratocumulus. *Journal of the Atmospheric Sciences*, 70(10):3102–3118.

Clement, A. C., Burgman, R., and Norris, J. R. (2009). Observational and model evidence for positive low-level cloud feedback. *Science*, 325(5939):460–4.

Deardorff, J. (1976). On the entrainment rate of a stratocumulus-topped mixed layer. *Quarterly Journal of the Royal Meteorological Society*, 102(433):563–582.

Dee, D., Uppala, S., Simmons, A., Berrisford, P., Poli, P., Kobayashi, S., Andrae, U., Balmaseda, M., Balsamo, G., Bauer, P., et al. (2011). The era-interim reanalysis: Configuration and performance of the data assimilation system. *Quarterly Journal of the Royal Meteorological Society*, 137(656):553–597.

Dolinar, E. K., Dong, X., Xi, B., Jiang, J. H., and Su, H. (2014). Evaluation of CMIP5 simulated clouds and TOA radiation budgets using NASA satellite observations. *Climate Dynamics*, 44(7-8):2229–2247.

Ebita, A., Kobayashi, S., Ota, Y., Moriya, M., Kumabe, R., Onogi, K., Harada, Y., Yasui, S., Miyaoka, K., Takahashi, K., et al. (2011). The japanese 55-year reanalysis" jra-55": an interim report. *Sola*, 7:149–152.

Fasullo, J. and Trenberth, K. (2012). A less cloudy future: The role of subtropical subsidence in climate sensitivity. *science*, 338(6108):792–4.

Garay, M. J., de Szoeke, S. P., and Moroney, C. M. (2008). Comparison of marine stratocumulus cloud top heights in the southeastern pacific retrieved from satellites with coincident ship-based observations. *Journal of Geophysical Research: Atmospheres (1984–2012)*, 113(D18).

Georgakakos, K. P. and Bras, R. L. (1984). A hydrologically useful station precipitation model: 1. formulation. *Water Resources Research*, 20(11):1585–1596.

Gregory, J. and Webb, M. (2008). Tropospheric adjustment induces a cloud component in co2 forcing. *Journal of Climate*, 21(1):58–71.

Hahn, C. and Warren, S. (1999). Extended edited synoptic cloud reports from ships and land stations over the globe, 1952-2006 (ndp-026c).

Hanson, H. P. (1991). Marine stratocumulus climatologies. *International journal of climatology*, 11(2):147–164.

Hartmann, D. L. (1994). *Global physical climatology*, volume 56. Academic press.

Hartmann, D. L., Ockert-Bell, M. E., and Michelsen, M. L. (1992). The effect of cloud type on earth's energy balance: Global analysis. *Journal of Climate*, 5(11):1281–1304.

Heidinger, A. K., Evan, A. T., Foster, M. J., and Walther, A. (2012). A Naive Bayesian Cloud-Detection Scheme Derived from CALIPSO and Applied within PATMOS-x. *Journal of Applied Meteorology and Climatology*, 51(6):1129–1144.

Held, I. M. and Soden, B. J. (2006). Robust responses of the hydrological cycle to global warming. *Journal of Climate*, 19(21):5686–5699.

Klein, S. A. and Hartmann, D. L. (1993). The seasonal cycle of low stratiform clouds. *Journal of Climate*, 6(8):1587–1606.

Klein, S. A., Hartmann, D. L., and Norris, J. R. (1995). On the relationships among low-cloud structure, sea surface temperature, and atmospheric circulation in the summertime northeast pacific. *Journal of climate*, 8(5):1140–1155.

Klein, S. a., Zhang, Y., Zelinka, M. D., Pincus, R., Boyle, J., and Gleckler, P. J. (2013). Are climate model simulations of clouds improving? An evaluation using the ISCCP simulator. *Journal of Geophysical Research: Atmospheres*, 118(3):1329–1342.

Kubar, T. L., Waliser, D. E., Li, J.-L., and Jiang, X. (2012). On the Annual Cycle, Variability, and Correlations of Oceanic Low-Topped Clouds with Large-Scale Circulation Using Aqua MODIS and ERA-Interim. *Journal of Climate*, 25(18):6152–6174.

Lacagnina, C. and Selten, F. (2013). A novel diagnostic technique to investigate cloud-controlling factors. *Journal of Geophysical Research: Atmospheres*, 118(12):5979–5991.

Lilly, D. K. (1968). Models of cloud-topped mixed layers under a strong inversion. *Quarterly Journal of the Royal Meteorological Society*, 94(401):292–309.

Loeb, N. G., Wielicki, B. A., Doelling, D. R., Smith, G. L., Keyes, D. F., Kato, S., Manalo-Smith, N., and Wong, T. (2009). Toward optimal closure of the earth's top-of-atmosphere radiation budget. *Journal of Climate*, 22(3):748–766.

Mace, G. G., Benson, S., Sonntag, K. L., Kato, S., Min, Q., Minnis, P., Twohy, C. H., Poellot, M., Dong, X., Long, C., Zhang, Q., and Doelling, D. R. (2006). Cloud radiative forcing at the Atmospheric Radiation Measurement Program Climate Research Facility: 1. Technique, validation, and comparison to satellite-derived diagnostic quantities. *Journal of Geophysical Research*, 111(D11):D11S90.

Mauger, G. S. and Norris, J. R. (2010). Assessing the Impact of Meteorological History on Subtropical Cloud Fraction. *Journal of Climate*, 23(11):2926–2940.

Meehl, G. a., Covey, C., Taylor, K. E., Delworth, T., Stouffer, R. J., Latif, M., McAvaney, B., and Mitchell, J. F. B. (2007). THE WCRP CMIP3 Multimodel Dataset: A New Era in Climate Change Research. *Bulletin of the American Meteorological Society*, 88(9):1383–1394.

Miller, R. (1997). Tropical thermostats and low cloud cover. *Journal of climate*, 10(3):409–440.

Minnis, P., Heck, P. W., Young, D. F., Fairall, C., and Snider, J. (1992). Stratocumulus cloud properties derived from simultaneous satellite and island-based instrumentation during fire. *Journal of Applied Meteorology*, 31(4):317–339.

Minnis, P., Sun-Mack, S., Chen, Y., Khaiyer, M. M., Yi, Y., Ayers, J. K., Brown, R. R., Dong, X., Gibson, S. C., Heck, P. W., et al. (2011a). Ceres edition-2 cloud property retrievals using trmm virs and terra and aqua modis data—part ii: Examples of average results and comparisons with other data. *Geoscience and Remote Sensing, IEEE Transactions on*, 49(11):4401–4430.

Minnis, P., Sun-Mack, S., Young, D. F., Heck, P. W., Garber, D. P., Chen, Y., Spangenberg, D. A., Arduini, R. F., Trepte, Q. Z., Smith, W. L., et al. (2011b). Ceres edition-2 cloud property retrievals using trmm virs and terra and aqua modis data—part i: Algorithms. *Geoscience and Remote Sensing, IEEE Transactions on*, 49(11):4374–4400.

Muñoz, R. C., Zamora, R. a., and Rutllant, J. a. (2011). The Coastal Boundary Layer at the Eastern Margin of the Southeast Pacific (23.4 °S, 70.4 °W): Cloudiness-Conditioned Climatology. *Journal of Climate*, 24(4):1013–1033.

Myers, T. A. and Norris, J. R. (2013). Observational Evidence That Enhanced Subsidence Reduces Subtropical Marine Boundary Layer Cloudiness. *Journal of Climate*, 26(19):7507–7524.

Myers, T. A. and Norris, J. R. (2015). On the Relationships between Subtropical Clouds and Meteorology in Observations and CMIP3 and CMIP5 Models*. *Journal of Climate*, 28(8):2945–2967.

Nakicenovic, N. and Swart, R. (2000). Special report on emissions scenarios. *Special Report on Emissions Scenarios, Edited by Nebojsa Nakicenovic and Robert Swart, pp. 612. ISBN 0521804930. Cambridge, UK: Cambridge University Press, July 2000.*, 1.

Norris, J. R. (1998a). Low cloud type over the ocean from surface observations. part i: Relationship to surface meteorology and the vertical distribution of temperature and moisture. *Journal of climate*, 11(3):369–382.

Norris, J. R. (1998b). Low cloud type over the ocean from surface observations. part ii: Geographical and seasonal variations. *Journal of climate*, 11(3):383–403.

Norris, J. R. and Evan, A. T. (2015). Empirical removal of artifacts from the isccp and patmos-x satellite cloud records. *Journal of Atmospheric and Oceanic Technology*, 32(4):691–702.

Norris, J. R. and Iacobellis, S. F. (2005). North pacific cloud feedbacks inferred from synoptic-scale dynamic and thermodynamic relationships. *Journal of Climate*, 18(22):4862–4878.

Norris, J. R. and Leovy, C. B. (1994). Interannual variability in stratiform cloudiness and sea surface temperature. *Journal of climate*, 7(12):1915–1925.

O'brien, R. M. (2007). A caution regarding rules of thumb for variance inflation factors. *Quality & Quantity*, 41(5):673–690.

O'Dell, C. W., Wentz, F. J., and Bennartz, R. (2008). Cloud liquid water path from satellite-based passive microwave observations: A new climatology over the global oceans. *Journal of Climate*, 21(8):1721–1739.

Onogi, K., Tsutsui, J., Koide, H., Sakamoto, M., Kobayashi, S., Hatsushika, H., Matsumoto, T., Yamazaki, N., Kamahori, H., Takahashi, K., Kadokura, S., Wada, K., Kato, K., Oyama, R., Ose, T., Mannoji, N., and Taira, R. (2007). The JRA-25 Reanalysis. *Journal of the Meteorological Society of Japan*, 85(3):369–432.

Park, S. and Leovy, C. B. (2004). Marine low-cloud anomalies associated with enso. *Journal of climate*, 17(17):3448–3469.

Pincus, R., Platnick, S., Ackerman, S. a., Hemler, R. S., and Patrick Hofmann, R. J. (2012). Reconciling Simulated and Observed Views of Clouds: MODIS, ISCCP, and the Limits of Instrument Simulators. *Journal of Climate*, 25(13):4699–4720.

Press, W. H., Teukolsky, S. A., Vetterling, W. T., and Flannery, B. P. (1996). *Numerical Recipes in Fortran 77: The Art of Scientific Computing.* Cambridge University Press.

Qu, X., Hall, A., Klein, S. a., and Caldwell, P. M. (2013). On the spread of changes in marine low cloud cover in climate model simulations of the 21st century. *Climate Dynamics*, 42(9-10):2603–2626.

Randall, D. A., Wood, R. A., Bony, S., Colman, R., Fichefet, T., Fyfe, J., Kattsov, V., Pitman, A., Shukla, J., Srinivasan, J., et al. (2007). Climate models and their evaluation. In *Climate Change 2007: The physical science basis. Contribution of Working Group I to the Fourth Assessment Report of the IPCC (FAR)*, pages 589–662. Cambridge University Press.

Rienecker, M. M., Suarez, M. J., Gelaro, R., Todling, R., Bacmeister, J., Liu, E., Bosilovich, M. G., Schubert, S. D., Takacs, L., Kim, G.-K., et al. (2011). Merra: Nasa's modern-era retrospective analysis for research and applications. *Journal of Climate*, 24(14):3624–3648.

Rossow, W. B. and Schiffer, R. A. (1999). Advances in understanding clouds from isccp. *Bulletin of the American Meteorological Society*, 80(11):2261–2287.

Rozendaal, M. A., Leovy, C. B., and Klein, S. A. (1995). An observational study of diurnal variations of marine stratiform cloud. *Journal of climate*, 8(7):1795–1809.

Saha, S., Moorthi, S., Pan, H.-L., Wu, X., Wang, J., Nadiga, S., Tripp, P., Kistler, R., Woollen, J., Behringer, D., Liu, H., Stokes, D., Grumbine, R., Gayno, G., Wang, J., Hou, Y.-T., Chuang, H.-Y., Juang, H.-M. H., Sela, J., Iredell, M., Treadon, R., Kleist, D., Van Delst, P., Keyser, D., Derber, J., Ek, M., Meng, J., Wei, H., Yang, R., Lord, S., Van Den Dool, H., Kumar, A., Wang, W., Long, C., Chelliah, M., Xue, Y., Huang, B., Schemm, J.-K., Ebisuzaki, W., Lin, R., Xie, P., Chen, M., Zhou, S., Higgins, W., Zou, C.-Z., Liu, Q., Chen, Y., Han, Y., Cucurull, L., Reynolds, R. W., Rutledge, G., and Goldberg, M. (2010). The NCEP Climate Forecast System Reanalysis. *Bulletin of the American Meteorological Society*, 91(8):1015–1057.

Sandu, I. and Stevens, B. (2011). On the factors modulating the stratocumulus to cumulus transitions. *Journal of the Atmospheric Sciences*, 68(9):1865–1881.

Sandu, I., Stevens, B., and Pincus, R. (2010). On the transitions in marine boundary layer cloudiness. pages 2377–2391.

Schubert, W. H., Wakefield, J. S., Steiner, E. J., and Cox, S. K. (1979). Marine stratocumulus convection. part i: Governing equations and horizontally homogeneous solutions. *Journal of the Atmospheric Sciences*, 36(7):1286–1307.

Sherwood, S. C., Bony, S., and Dufresne, J.-L. (2014). Spread in model climate sensitivity traced to atmospheric convective mixing. *Nature*, 505(7481):37–42.

Simon, R. L. (1977). The summertime stratus over the offshore waters of california. *Monthly Weather Review*, 105(10):1310–1314.

Soden, B. J. and Vecchi, G. a. (2011). The vertical distribution of cloud feedback in coupled ocean-atmosphere models. *Geophysical Research Letters*, 38(12):n/a–n/a.

Stevens, B. (2006). Bulk boundary-layer concepts for simplified models of tropical dynamics. *Theoretical and Computational Fluid Dynamics*, 20(5-6):279–304.

Stocker, T., Qin, D., Plattner, G.-K., Tignor, M., Allen, S. K., Boschung, J., Nauels, A., Xia, Y., Bex, V., and Midgley, P. M. (2014). *Climate change 2013: The physical science basis*. Cambridge University Press Cambridge, UK, and New York.

Su, H., Jiang, J. H., Zhai, C., Shen, T. J., Neelin, J. D., Stephens, G. L., and Yung, Y. L. (2014). Weakening and strengthening structures in the Hadley Circulation change under global warming and implications for cloud response and climate sensitivity. *Journal of Geophysical Research: Atmospheres*, 119(10):5787–5805.

Sun, F., Hall, a., and Qu, X. (2011). On the relationship between low cloud variability and lower tropospheric stability in the Southeast Pacific. *Atmospheric Chemistry and Physics Discussions*, 11(2):3777–3811.

Taylor, K. E., Stouffer, R. J., and Meehl, G. A. (2007). A Summary of the CMIP5 Experiment Design. 2009(January 2011):1–33.

Taylor, K. E., Stouffer, R. J., and Meehl, G. A. (2012). An overview of cmip5 and the experiment design. *Bulletin of the American Meteorological Society*, 93(4):485–498.

Vecchi, G. a. and Soden, B. J. (2007). Global Warming and the Weakening of the Tropical Circulation. *Journal of Climate*, 20(17):4316–4340.

Vial, J., Dufresne, J.-L., and Bony, S. (2013). On the interpretation of inter-model spread in CMIP5 climate sensitivity estimates. *Climate Dynamics*, 41(11-12):3339–3362.

Wang, L., Wang, Y., Lauer, A., and Xie, S.-P. (2011). Simulation of Seasonal Variation of Marine Boundary Layer Clouds over the Eastern Pacific with a Regional Climate Model *. *Journal of Climate*, 24(13):3190–3210.

Webb, M., Senior, C., and Sexton, D. (2006). On the contribution of local feedback mechanisms to the range of climate sensitivity in two GCM ensembles. *Climate Dynamics*, 27(1):17–38.

Webb, M. J., Lambert, F. H., and Gregory, J. M. (2012). Origins of differences in climate sensitivity, forcing and feedback in climate models. *Climate Dynamics*, 40(3-4):677–707.

Wood, R. (2012). Stratocumulus Clouds. *Monthly Weather Review*, 140(8):2373–2423.

Wood, R. and Bretherton, C. (2006). On the relationship between stratiform low cloud cover and lower-tropospheric stability. *Journal of climate*, 19(24):6425–6432.

Wood, R. and Bretherton, C. S. (2004). Boundary Layer Depth, Entrainment, and Decoupling in the Cloud-Capped Subtropical and Tropical Marine Boundary Layer. *Journal of Climate*, 17(18):3576–3588.

Wood, R. and Hartmann, D. (2006). Spatial variability of liquid water path in marine low cloud: The importance of mesoscale cellular convection. *Journal of Climate*, 17(9):1748–1764.

Wyant, M. C., Bretherton, C. S., Rand, H. A., and Stevens, D. E. (1997). Numerical simulations and a conceptual model of the stratocumulus to trade cumulus transition. *Journal of the atmospheric sciences*, 54(1):168–192.

Zelinka, M. D., Klein, S. a., and Hartmann, D. L. (2012). Computing and Partitioning Cloud Feedbacks Using Cloud Property Histograms. Part I: Cloud Radiative Kernels. *Journal of Climate*, 25(11):3715–3735.

Zhang, Y., Stevens, B., Medeiros, B., and Ghil, M. (2009). Low-Cloud Fraction, Lower-Tropospheric Stability, and Large-Scale Divergence. *Journal of Climate*, 22(18):4827–4844.

Zhang, Y., Xie, S., Covey, C., Lucas, D. D., Gleckler, P., Klein, S. a., Tannahill, J., Doutriaux, C., and Klein, R. (2012). Regional assessment of the parameter-dependent performance of CAM4 in simulating tropical clouds. *Geophysical Research Letters*, 39(14):n/a–n/a.

Zhou, C., Zelinka, M. D., Dessler, A. E., and Yang, P. (2013). An analysis of the short-term cloud feedback using modis data. *Journal of Climate*, 26(13):4803–4815.